



Center for the Commercial Deployment
of Transportation Technologies

CFD Design Tool Development and Validation

Submitted by:

Hamid Hefazi, Task Manager
hefazi@csulb.edu
Program Element 2.8, Fiscal Year 2000

Submitted to:

Center for the Commercial Deployment of Transportation Technologies
California State University, Long Beach Foundation
6300 State University Drive, Suite 332 • Long Beach, CA 90815 • 562.985.7394

February 4, 2002

TABLE OF CONTENTS

	<u>Page Number</u>
Executive Summary	1
Introduction.....	3
Chapter 1. Design Method Development and Application to Underwater Hull Configuration Optimization	5-39
Purpose.....	5
Design/optimization method.....	6
1.1. Computational Fluid Dynamics Tool.....	8
1.1.1. Panel method with free surface modeling with negative image	8
1.1.2. Interactive Boundary Layer Approach.....	9
1.1.3. Comparison with experimental data: Midfoil Bay Test	11
1.1.4. Application to Baseline Twin-H Configuration.....	14
1.2. Hull shape representation.....	17
1.2.1. Parametric representation.....	17
1.2.2. Meshing, including extra-strips.....	19
1.2.3. Parameterization of foil cross-sections for optimization	20
1.3. Optimization method	21
1.3.1. Latin Hypercubes	21
1.3.2. Genetic Algorithms	22
1.4. Integration into design/optimization tool.....	23
1.5. Tests and application: Twin-H body optimization.....	28
1.5.1. Problem set up.....	28
1.5.2. DOE	28
1.5.3. Design variables.....	28
1.5.4. Parametric study.....	29
1.5.5. Genetic algorithm optimization	31
1.5.6. Validation of optimum	35
Chapter 2. Development of accurate free surface calculation methods.....	40-66
2.1. Two-Dimensional Free Surface Method for Hydrofoils.....	40
2.1.1. Mathematical formulation.....	41
2.1.2. Numerical Validation	45
2.1.3. Submerged circular cylinder	46
2.1.4. Submerged hydrofoils	48

Center for the Commercial Deployment of Transportation Technologies

2.2.	Three-Dimensional Free surface code development and improvement for high-speed ships.....	54
2.2.1.	Use of extra strips.....	55
2.2.2.	Symmetry option.....	57
2.2.3.	Free Surface mesh sensitivity study.....	58
2.2.4.	Modeling of Strut/Free surface Intersection	62
2.2.5.	Fully submerged configuration	63
2.2.6.	Twin-H configuration	64
2.2.7.	Remaining Work	65
2.3	Interactive Boundary Layer with Free Surface.....	66
	Summary/Conclusion.....	67
	Bibliography	69
	List of Tables	71
	List of Figures.....	72
	Glossary	74
	Acknowledgment	75
	Appendix A.....	76-108

EXECUTIVE SUMMARY

CCDoTT task 2.8 “Computational Fluid Dynamics (CFD) Design Tool Development and Validation” was a fast paced, intensive research program to develop state-of-the-art *Computational Fluid Dynamics (CFD) and optimization tools* for applications in the design and optimization of ship hull forms. This first phase of the project started in October 2000 and was concluded in July 2001. To achieve the ambitious goals of the project, a team consisting of six CSULB Faculty, two research associates, three independent contractors, and three graduate students, along with a team from our partner Pacific Marine, participated in the project. A subtask of the project was also contracted to the Boeing Company.

The CFD methods developed in this phase of the project consist of a method for the accurate prediction of two-dimensional (2D) free surface effects as well as initiation of the three-dimensional (3D) free surface method to be completed in phase two of the project, and an Interactive Boundary Layer (IBL) method for computation of viscous effects. These CFD methods differ from existing methods by implementing the non-linear free surface boundary condition in a more accurate and direct form, thus leading to a more accurate prediction of the sea surface shape and the resulting wave drag. The optimization tools developed include a novel automatic numerical optimization process using these and other CFD methods in conjunction with Computer Aided Design (CAD), surface meshing, and optimization programs.

The CFD programs developed here are first used to analyze Pacific Marine’s innovative LSCX hull form. This patent-pending underwater body is currently being evaluated for incorporation into a number of high-priority military programs including the U.S. Navy’s proposed new Littoral Support Craft (LSC) and the U.S. Army’s proposed new Theater Support Vessel (TSV) (also referred to as the Logistics Support Vessel LSV). At the same time, this hull form also offers the commercial fast ferry market the possibility of delivering significantly higher speeds and greater sea kindliness than current fast ferry designs.

The optimization method developed in this project was then applied to this hull form to optimize and improve its Lift to Drag ratio (L/D) and performance by 17%. In this first phase of the project, the optimization process mostly relies on the first generation CFD codes already developed by the Aerospace Engineering (AE) faculty of CSULB and others. In the second part (FY01), the more advanced CFD methods developed and validated here will be utilized for optimization. Therefore, while Part 1 will provide a useful design/optimization tool, Part 2 will greatly enhance this tool by integrating higher fidelity CFD models and more advanced optimization methods, and by enhancing its robustness and efficiency. While we use the Pacific Marine’s LSCX as our test case, the fast ship technologies developed and demonstrated under this task are dual-use, with both commercial and military applications. The technologies will help meet CCDOTTs goal of improving America's high-speed Marine sealift capabilities and the technology breakthroughs needed to achieve this objective.

Center for the Commercial Deployment of Transportation Technologies

This report documents the details of our accomplishments on the various tasks outlined in our proposal and Statement of Work.

Center for the Commercial Deployment of Transportation Technologies

INTRODUCTION

The goal of this project is to develop state of the art Computational Fluid Dynamic (CFD) software, designs and optimization software, and apply them to fast ship designs. Using these tools, an underwater “lifting body” designed by Pacific Marine for application to a Littoral Support Craft (LSC) will be analyzed and optimized. The technologies to be developed and demonstrated under this proposal, however, are dual-use, with both commercial and military applications. The technologies will help meet CCDoTT’s goal of improving America’s high-speed marine sealift capabilities, and provide the technology breakthroughs needed to achieve this objective.

Military planners envision the need for the fleet to stand offshore 100 nautical miles or more when a port of opportunity is denied, or destroyed, or cruise missiles pose a threat to large ships operating too close to shore. The LSC(X) is needed to transit and support the movement of men and materiel through the littoral zone, serving as the final link in the Navy’s logistical chain. The three principal missions of the LSC(X) have been identified: as vertical replenishment (VERTREP) by helicopter or V-22 tilt-rotor aircraft; communications support; and service as the Forward Area Arming Replenishment Platform (FARP). The design and construction of the LSC(X) has been funded by the Navy and work has already begun on this high priority program.

The LSC(X) is being designed to achieve a minimum top speed of 40 knots, with an ultimate goal of 50 knots. A successful LSC(X) would thus be a high-speed sealift craft as envisioned by CCDoTT and the technologies demonstrated by the successful deployment of the LSC(X) will be equally applicable to commercial craft.

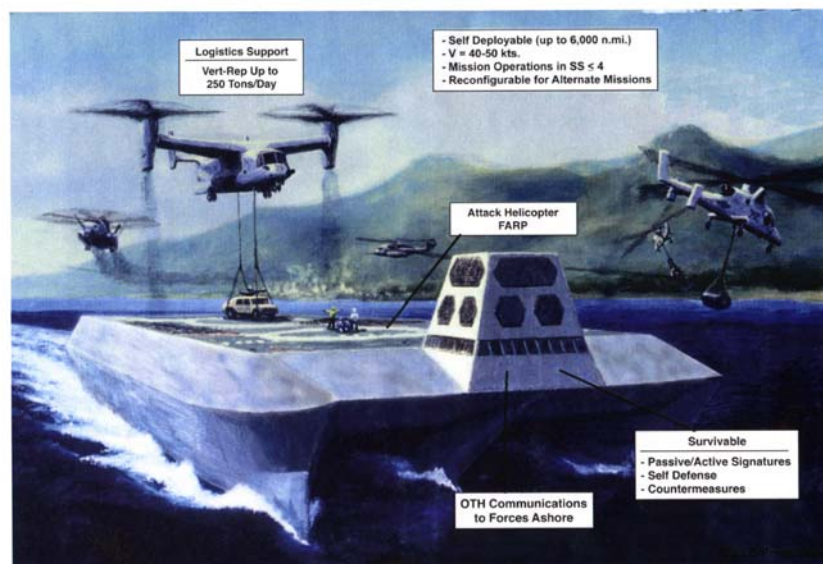


Figure 1. Artist's Concept of LSC(X)

Center for the Commercial Deployment of Transportation Technologies

This report consists of two major chapters. Chapter 1 describes design and optimization development and application to the LSC(x) lift body. Chapter 2 discusses the development of new CFD methods focusing on the accurate prediction of free surface and wave drag.

The advanced ship hull design/optimization software developed, despite limited applications to the LSC(x) configuration in this project, which address hydrodynamic aspects required in the design phase of fast ships will be a valuable resource equally applicable to the design of future commercial and military (and dual-use) high speed vessels. The advanced hull forms designed therewith offer the added advantage of reduced drag at a given speed, and thus increased fuel efficiency and range.

Chapter 1. Design Method Development and Application to Underwater Hull Configuration Optimization

This chapter describes the activities and accomplishments associated with Task 1 of our Statement of Work.

Purpose

This chapter presents an optimization method developed for the Computational Fluid Dynamics (CFD) design of lifting bodies also referred to as underwater hull configurations. The method is applied to the shape optimization of a lifting submerged configuration consisting of two displacement bodies, called *H-bodies*, linked with a thin foil, referred to as *cross-foil*, and attached to the ship by two struts (Fig. 1). The entire arrangement is referred to as the twin H-body configuration and is designed to be fitted to a catamaran or pentamaran ship. The displacement hulls are designed to provide good sea-keeping properties at lower speeds when the hulls of the catamaran or pentamaran are partially submerged, while the cross-foil is designed to provide additional lift at higher speed when the multiple hulls are lifted out of the water in order to reduce drag.

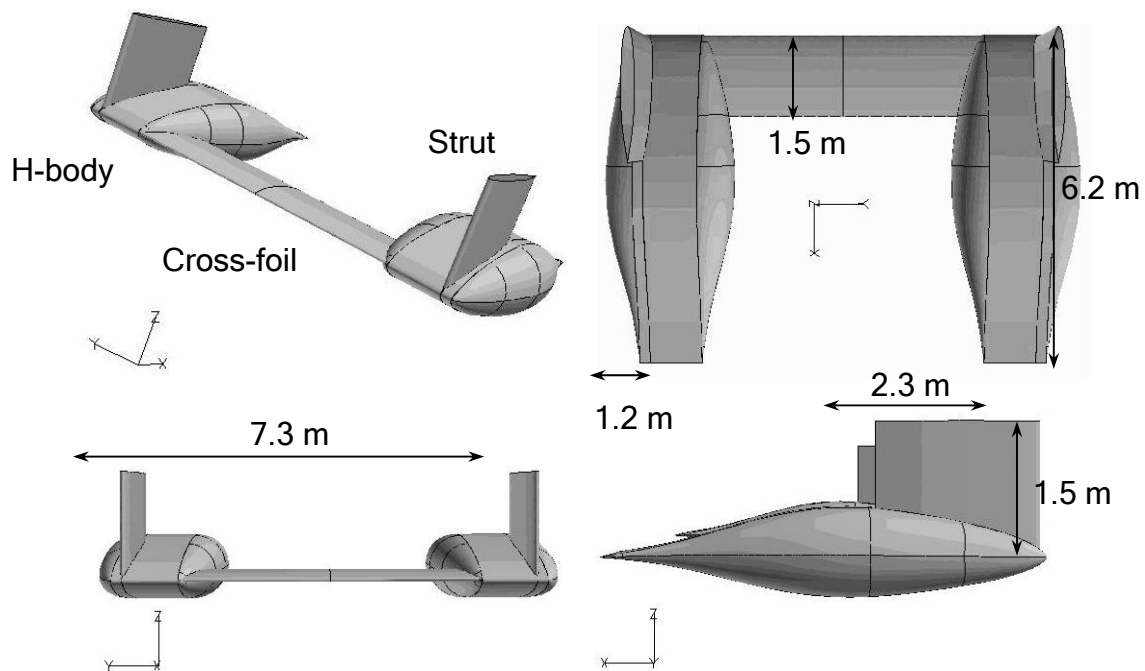


Figure 2. Twin H-body configuration, Baseline

The optimization is performed for a boat speed of 40 knots. At this velocity, the boat is designed so that all hulls, other than the twin H-body, are out of the water. The configuration must be able to generate a total lift of 60 LT, including a minimum of 20 LT of displacement. The objective is to optimize for range, i.e. lift-to-drag ratio, which corresponds to minimizing drag at constant lift. In addition, the configuration is to be designed such that it can operate cavitation free at 45 knots.

Center for the Commercial Deployment of Transportation Technologies

From an optimization problem viewpoint, the objective function and design constraints can be summarized as:

- Objective: Maximize L/D
- Constraints:
 - Cavitation free at 45 knots, i.e. $C_p > -0.357$ (Hawaii water at 75 F)
 - Total lift equal to 30 LT
 - Displacement greater than 20 LT
 - The span (location where strut and H-body intersect) is fixed at 7.315 m and the strut and cross-foil must be aligned for structural reasons.

At 40 knots in 75 F HI waters, the Reynolds number per meter is 20.7×10^6 .

Design/optimization method

A general optimization process is illustrated in Fig. 2. An initial set of s design variables, $\mathbf{x} = (x_i)_{1 \leq i \leq s}$, which might represent the configuration designed by experienced engineers, is supplied to the optimizer. Then, for this design, the objective function, f , is evaluated and the constraints, g_i , are analyzed to check whether they are violated or not. If the optimum is not reached, these values are fed back to the optimizer that modifies the design vector \mathbf{x} . The process is repeated until convergence.

For the application to aerodynamic or hydrodynamic optimization, the three main components of the numerical method are, (1) the representation of a configuration by a set of design variables (D.V.), \mathbf{x} , (2) the optimization method, and (3) the evaluation of the aerodynamic performance, i.e. f , for a given configuration. The constraints, g_i , are analyzed at the stage appropriate for the problem considered.

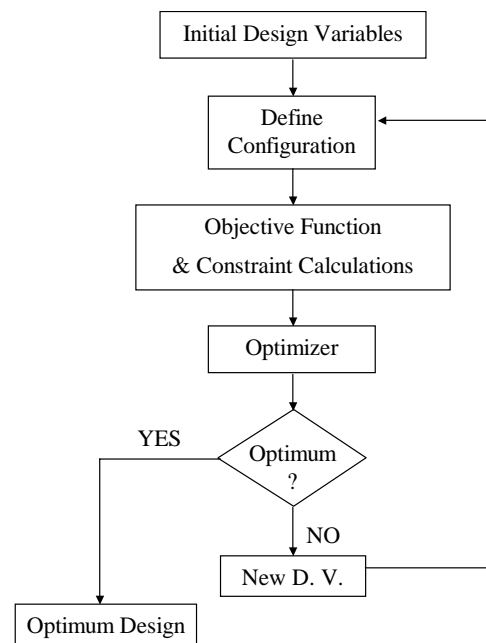


Figure 3. Flowchart of the numerical optimization.

Center for the Commercial Deployment of Transportation Technologies

Nowadays, all design engineers are accustomed to designing their vehicles using some Computer Aided Design (CAD) or solid modeling package, such as Pro-Engineer, CATIA, UniGraphics, Ideas, etc. In addition, the designer usually represents the configuration by a set of parameters, or design variables, which can be varied to improve the design by linking the CAD software with an appropriate analysis module. This approach is routinely used for structural design, for example, by linking the CAD software with a Finite Element (FE) method. Such approach is not yet routinely used, however, in the case of hydrodynamic shape optimization, because additional challenges face the designer. Among these issues are

- The cost and accuracies associated with flow analysis using CFD
- The grid requirements for CFD methods

In order to address the issue of CFD shape optimization, one must be able to *automatically* vary the shape of various elements of the configuration in the CAD method, generate a mesh of sufficient quality for the CFD method, and use an efficient and accurate CFD method to obtain the hydrodynamic performance of the configuration being analyzed. The driver in the selection of the components of the CFD optimization method is the ability to link these tools together in an automated fashion, without user intervention, while ensuring that the flow analysis is both efficient and accurate for the problem at hand. For this reason, several options for each tool were considered and the following set of tools was selected:

- CAD software: *Pro-Engineer* [1]
- Grid generation software: *ICEM-CFD* [2]
- CFD software: CSULB-developed Interactive Boundary Layer (IBL) approach with free surface modeled by negative images [3]
- Optimization software: *iSIGHT* [4]

Pro-Engineer and *ICEM-CFD* were selected because of the existence of a module which does allow for automatic data transfer between the CAD and grid generation package. The IBL approach was chosen, because at high Reynolds numbers and low angles of attack, it is a very accurate and efficient approach. In addition, because of the large Froude number for the case at hand, the free surface can be modeled with negative images. Finally, the numerical optimizer *iSIGHT* offers an easy to use platform for the optimization and/or design of experiments. The CFD tool is presented and discussed in Sect. 1.1. The twin H-body hull representation is addressed in Sect. 1.2, and the numerical optimization method is briefly described in Sect. 1.3. These components are integrated into the design/optimization tools, as shown in Sect. 1.4, and the resulting method is applied to the optimization of the twin H-body configuration in Sect. 1.5.

It is important to note, however, that the present design/optimization method does not restrict the CFD code to be the CSULB IBL method. Other methods, such as potential flow based or those solving the Navier-Stokes equations, could be used as well. Some modifications may be needed in the Pro-Engineer component (such definition of an outer control volume) and would definitely be required in the meshing procedure.

Center for the Commercial Deployment of Transportation Technologies

1.1 Computational Fluid Dynamics Tool

1.1.1. Panel method with free surface modeling with negative image

The inviscid flow is computed by the higher-order Hess panel method [5], which is applicable to a complete airplane configuration. In this method, a general body is represented by means of a set of curved quadrilateral panels. The complete solution for a prescribed flow condition is obtained by simultaneously satisfying a condition of zero or prescribed normal velocity at a control point on each panel of the body together with a Kutta condition at each trailing edge panel.

If a free surface is present as depicted in Fig. 3, in addition to the free-air conditions, the flow must satisfy a condition of zero (atmospheric) pressure along the free surface. The location is initially unknown. However, if disturbances are assumed small, i.e. velocity is not very different from its free stream value V and free surface height and slopes are small, the free surface condition may be linearized to

$$V^2\phi_{xx} + g\phi_z = 0 \quad \text{on} \quad z = 0 \quad (1)$$

This condition may be applied to either the total potential or the perturbation potential, since the free stream potential $\Phi_\infty = Vx$ gives zero when put in the left side of the above equation.

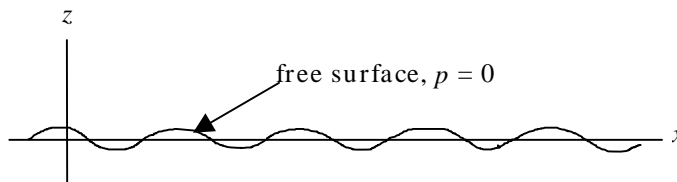


Figure 4. Free surface flow

The incorporation of the free surface condition into the problem is very difficult in general, but is easy in two limiting cases.

Case 1: Small V , low Froude Number

The first term in (1) may be neglected giving

$$\phi_z = 0 \quad \text{on} \quad z = 0 \quad (2)$$

i.e. $z = 0$ may be replaced by a solid wall.

Case 2: Large V , high Froude Number

The term ϕ_{xx} must be small or approximately

$$\phi_{xx} = 0, \quad u = V \quad \text{on} \quad z = 0 \quad (3)$$

where u is the velocity component in the free stream direction.

As is well known, Case 1 may be simulated by calculating the flow about the body and its mirror image in the $z = 0$ plane (positive image). In terms of sources and vortices, this means that any

Center for the Commercial Deployment of Transportation Technologies

source or source distribution on the actual body gives rise to an equal source at the image point. A vortex, however, gives rise to a negative vortex at the image point. It is readily verified, that these combinations, shown in Fig. 4, give zero vertical velocity on $z = 0$.

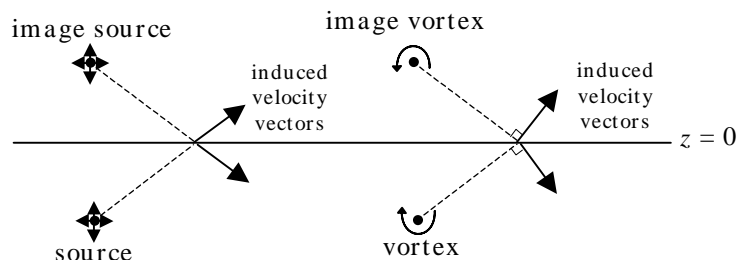


Figure 5. Induced velocities with positive image.

Case 2 is less familiar. However, it turns out that, as shown in Fig. 5, the signs of the image singularities are reversed (negative image). It can be seen that these combinations give zero horizontal velocity on $z=0$, leaving the velocity there equal to free stream.

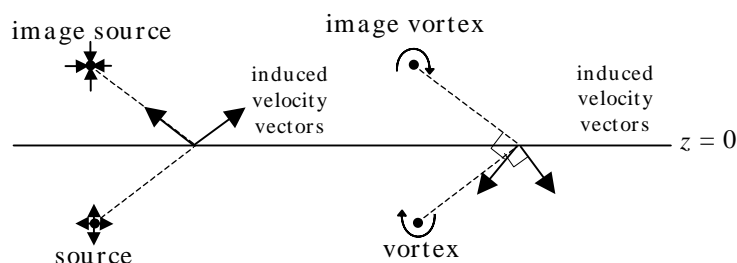


Figure 6. Induced velocities with negative image.

The panel method includes options for either positive symmetry (solid boundary) or negative symmetry (free surface) on either the $y=0$ or the $z=0$ planes. In addition, combinations of two symmetry boundary conditions can be specified. For most of the cases included in this report, a positive symmetry condition on $y=0$ is combined with a negative symmetry condition at $z=0$ to represent the water surface. This method was used successfully for calculating lift and induced drag distributions on hydrofoils with struts. [3]

1.1.2 Interactive Boundary Layer Approach

For a given configuration, the flowfield can be calculated by either solving the Navier-Stokes (NS) equations or employing an Interactive Boundary Layer (IBL) approach. The latter is based on the interactive solution of the inviscid and boundary layer equations. Again, it is not as general as the former but offers a good compromise between the efficiency and the accuracy needed in a design environment and is therefore selected here. Also, for the purpose of hydrofoil design subject to low cavitation numbers, Reynolds numbers are large, viscous effects are small,

Center for the Commercial Deployment of Transportation Technologies

and therefore the boundary layer approximation is appropriate. Thus for the present application, results with IBL are as accurate as with NS methods.

The IBL method has been used extensively for single and multi-element airfoil flowfield predictions and is described in greater detail in the literature [6]. Its ingredients are shown in Fig. 6. The inviscid flow field is computed by the panel method described above. In summary, once the external velocity distribution is known, the boundary layer equations are solved in an inverse mode using the Hilbert integral formulation to allow for the computation of possibly separated flows. Transition is determined as part of the solution procedure, employing either the e^n -method or correlation formulas. Since for the present application all calculations are performed at very high Reynolds numbers, transition was set near the stagnation point. The turbulent flow calculations employ a modified Cebeci-Smith eddy viscosity formulation, validated for both accelerating and adverse pressure gradient flows. In addition, surface roughness is modeled into the method using the Cebeci-Chang roughness model. See for example [7] for more details.

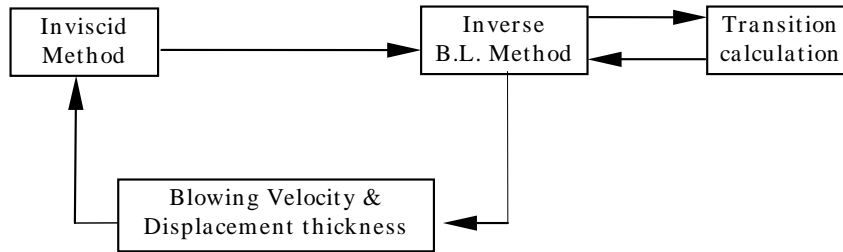


Figure 7. Interactive Boundary Layer approach.

The displacement thickness and blowing velocity distributions are used to simulate the viscous effects in the inviscid method. The procedure is repeated until convergence.

The profile drag (friction and pressure) is calculated with the Squire-Young formula [8] applied several chords downstream of the trailing edge

$$c_d = 2\overline{\theta} \overline{u_e}^{\left(\frac{H+5}{2}\right)} \quad (4)$$

where $\overline{u_e} \equiv u_e/V$ is the velocity at the edge of the boundary layer normalized by the freestream velocity, $H \equiv \delta^*/\theta$ is the shape factor, δ^* is the displacement thickness, θ is the momentum thickness and $\overline{\theta} \equiv \theta/c$.

The viscous effects are currently included in the method for lifting sections only, i.e. for sections with a distinct leading edge, a stagnation point, trailing edge and wake. The viscous drag associated with the caps is computed from [9]:

$$(D)_{caps} = \left(1.0 + 1.5 \left(\frac{d}{l} \right)^{1.5} + 7.0 \left(\frac{d}{l} \right)^3 \right) c_f q_\infty (S_{wet})_{caps} \quad (5)$$

Center for the Commercial Deployment of Transportation Technologies

where d is the cap diameter, l its length, and $(S_{wet})_{caps}$ is the caps wetted area. Here, c_f is the average skin friction and is given by [9]:

$$c_f = \frac{0.455}{(\log(R_l))^{2.58}} \quad (6)$$

where R_l is the Reynolds number based on l . This formula assumes fully turbulent flow, which is a very good approximation for high Reynolds number flows.

1.1.3. Comparison with experimental data: Midfoil Bay Test

In this section, the calculation method is applied to the Midfoil configuration, which was tested in a bay in Hawaii at 20.2 knots [10]. The configuration is shown in Fig. 7. The red part denotes the submerged configuration addressed here. The Midfoil hull is positioned at a 2 degree angle of attack, and the forward T-foil is at an angle of 2.5 deg. For this test case, one might expect to have a rather significant effect of the free surface shape on the pressure distribution above the main lifting hull since the velocity is “only” 20 knots and, more importantly, the top of the foil operates less than 2 ft from sea level at rest. Fig. 8 shows the pressure distribution computed by the CFD method on the Midfoil configuration. Fig. 9 shows a comparison between measured and computed pressure distribution at a span-wise distance of 5 ft from the centerline. Although the free surface is extremely close to the body (a couple feet on top of the main displacement body), results show that the pressure distribution obtained by the negative image approach does not drastically differ from measurements. At higher speeds (i.e. higher Froude numbers) and higher depth-to-chord ratios, this comparison would even improve significantly.

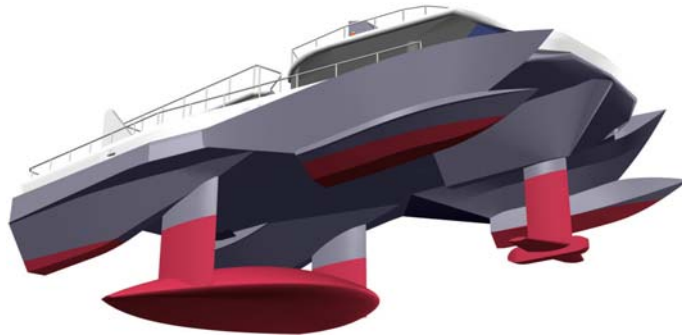


Figure 8. Midfoil configuration (submerged parts in red)

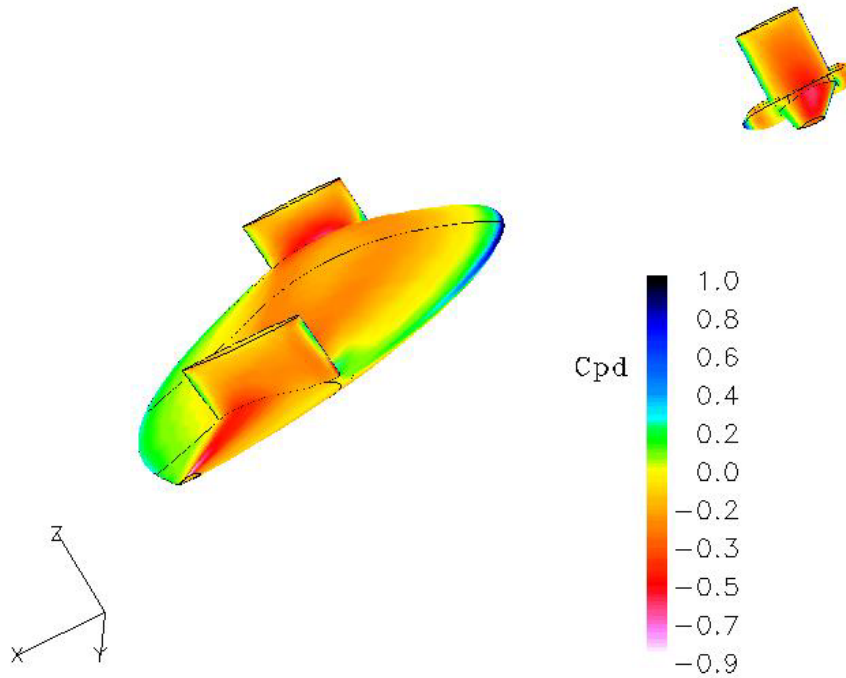


Figure 9. Pressure distribution on the Midfoil

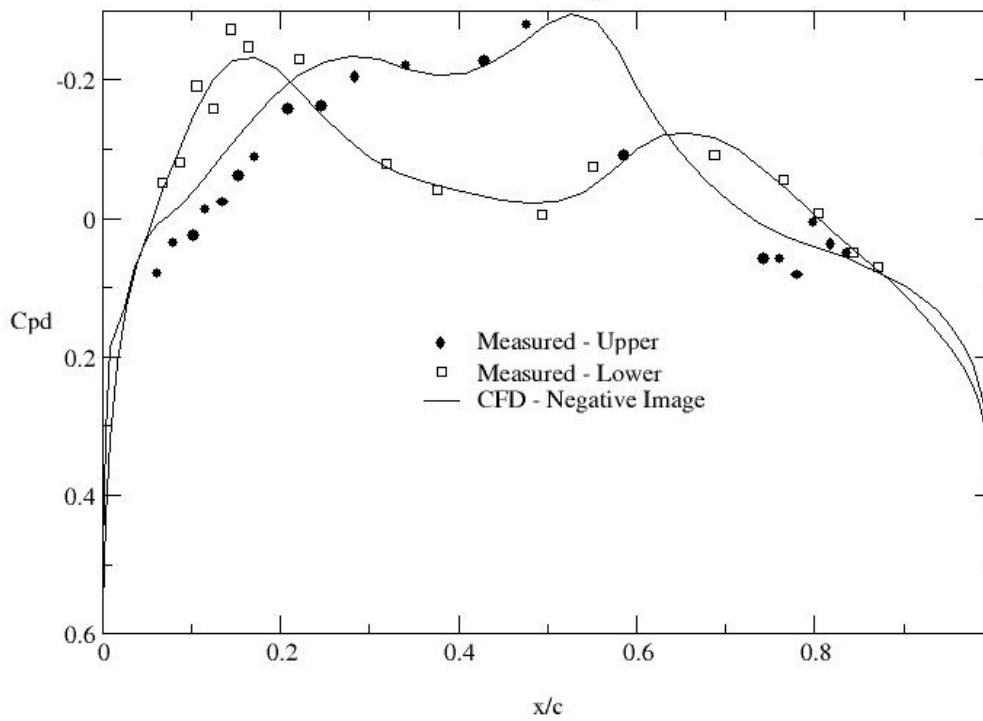


Figure 10. Comparison between measured and calculated pressure distribution at $y = 5$ ft

Center for the Commercial Deployment of Transportation Technologies

In addition to the pressure measurements, boundary layer profiles were also measured at four locations on the $y = 5$ ft line:

- At 9.8 ft and 17.1 ft from the leading edge on the lower surface
- At 17.6 ft and 20.1 ft from the leading edge on the upper surface

The surface roughness was measured to be 0.001253 in. For some of these points, the outer boundary layer was not properly measured and the velocity recorded at the farthest point away from the wall did not match that of the pressure data. Therefore, the data comparison is shown only for the non-dimensional velocity profiles, u^+ vs. y^+ , where u^+ vs. y^+ are the usual boundary layer log law profiles [7]:

$$y^+ = \frac{u_\tau y}{\nu}, \quad u^+ = \frac{u}{u_\tau} \quad (7)$$

Fig. 11 shows the results for the lower surface and Fig. 12 for the upper surface for the most downstream points. Calculations are shown for three cases: when transition is free to take place wherever the model calculates it (i.e. “free transition” flow over smooth surface), with “fully turbulent” flow (over smooth surface), and with surface roughness considered in the turbulence model. Results clearly show that roughness is present and that the Cebeci-Chang roughness model does successfully predict the effect of roughness on the inner layer. The discrepancies discussed earlier when reaching the outer part of the boundary layer are visible.

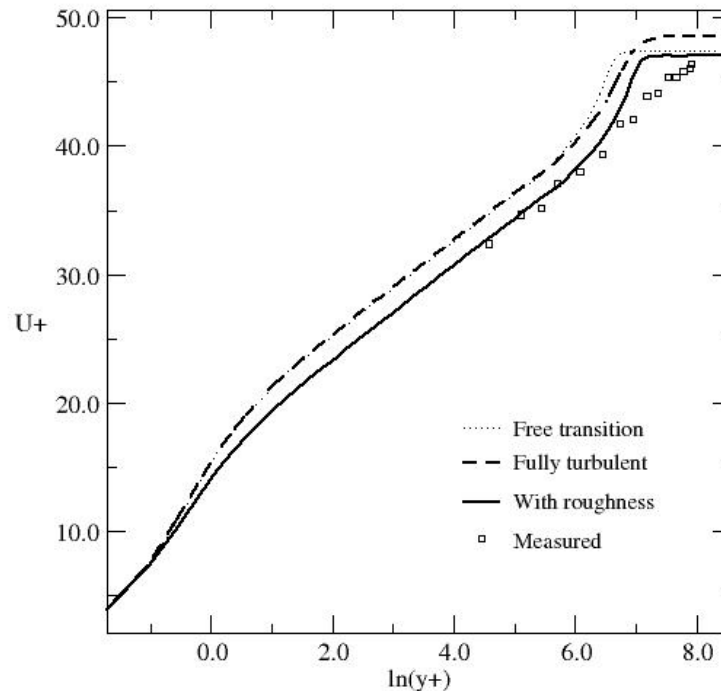


Figure 11. Log law profiles at $y = 5$ ft on the Midfoil lower surface at 17.1 ft from the leading edge

Center for the Commercial Deployment of Transportation Technologies

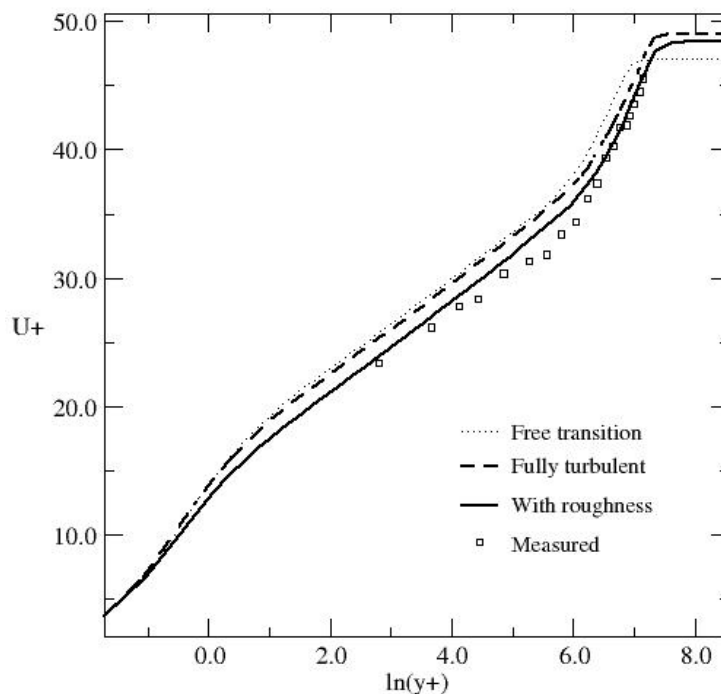


Figure 12. Log law profiles at $y = 5$ ft on the Midfoil upper surface at 20.1 ft from the leading edge

1.1.4 Application to Baseline Twin-H Configuration

The method is applied here to the baseline twin H-body configuration at 0 deg. angle of attack. Fig. 13 shows the pressure distribution over the configuration. Fig. 14 shows a comparison between the IBL method with negative image (“IBL-Neg”) and the full free surface method being developed at CSULB (wave code). It should be noted that, currently, experimental data for this configuration is not available for comparison with our CFD results. Such “at-sea trials” are planned for the next phase of the program. The data collected will be used to further validate our CFD results. More details are presented in Chapter 2, where we discuss the development of the three-dimensional free surface method. In summary, the results show excellent agreement between the two methods, confirming the appropriateness of the negative image approximation (large Froude number).

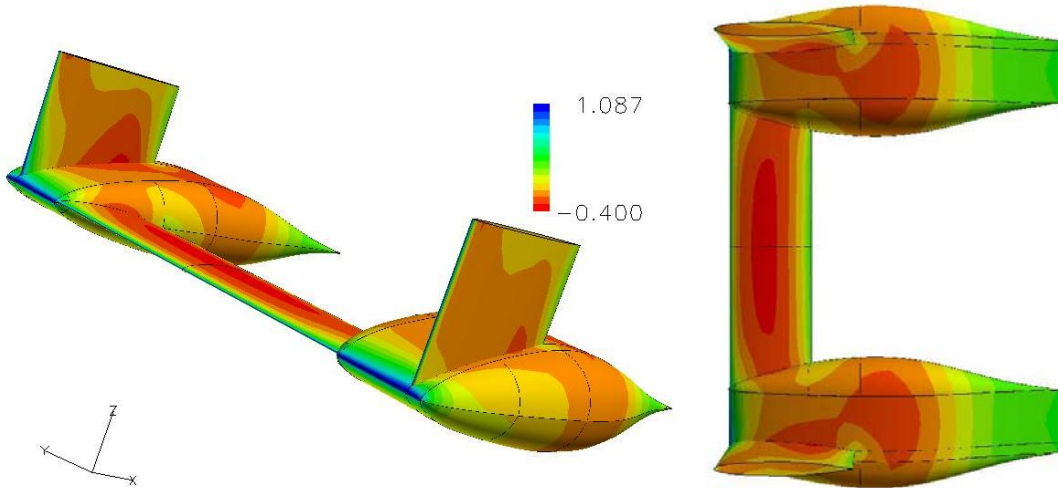
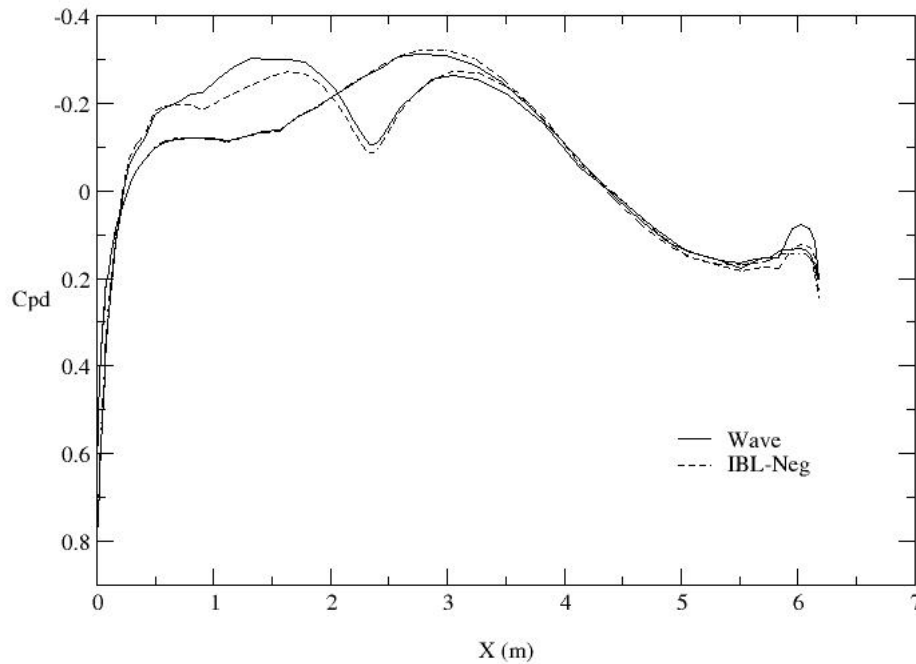
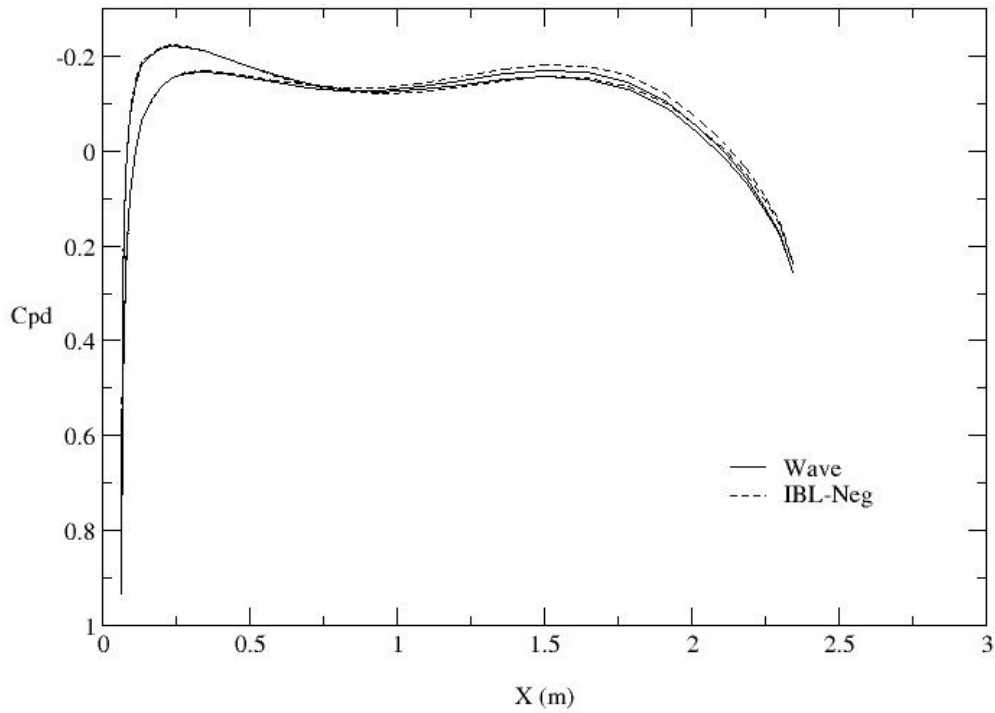


Figure 13. Dynamic pressure coefficient distribution over the baseline twin-H configuration

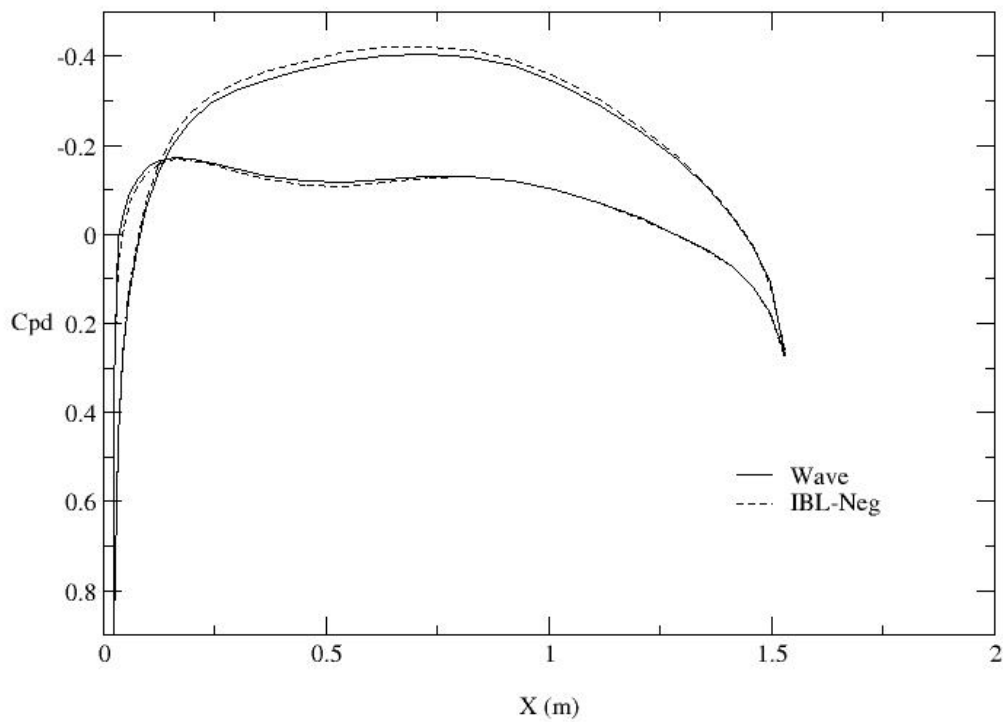


(a)

Figure 14. Pressure distribution computed by the CSULB IBL method with negative images (IBL-Neg.) and free surface code (wave) on (a) the H-body (at $y = 3.8$ m), (b) on the strut (at $z = -0.12$), and (c) on the cross-foil (at $y = 0.4$ m – centerline is at $y=0$)



(b)



(c)

Figure 14. Pressure distribution computed by the CSULB IBL method with negative images (IBL-Neg.) and free surface code (wave) on (a) the H-body (at $y = 3.8$ m), (b) on the strut (at $z = -0.12$), and (c) on the cross-foil (at $y = 0.4$ m – centerline is at $y=0$), concluded

Center for the Commercial Deployment of Transportation Technologies

Table 1 presents the computed lift for the baseline at 0 deg. using three different CFD methods available, the IBL method with negative image (“IBL-Neg.”), the free surface code under development at CSULB (“wave code”, see Sect. 2.), as well as USAERO, a commercially available three-dimensional panel method developed by Analytical Methods, Inc. Pacific Marine (Navatek, Ltd., of Hawaii) generated the results quoted here. As it can be seen, the IBL-Neg and the wave code show very consistent results. The USAERO value, however, is somewhat different. A discussion of the differences between these methods is presented later in Section 1.5, under the "validation of optimum" section.

Table 1. Lift for the baseline configuration at 0 deg. angle of attack

<i>Lift in LT</i>	<i>IBL-Neg.</i>	<i>Wave</i>	<i>USAERO¹</i>
Displacement	20.4	20.4	20.4
Dynamic	28.9	26.4	19.3
<i>Total Lift</i>	<i>49.3</i>	<i>46.8</i>	<i>39.7</i>
<i>Drag in LT</i>	<i>4.75</i>	<i>N/A</i>	<i>5.65</i>
<i>L/D</i>	<i>10.38</i>	<i>N/A</i>	<i>7.92</i>

Table 2 presents the detailed results for the baseline configuration in terms of objective function and constraints used in optimization. The Table shows that the displacement requirement is met, but at $\alpha = 0^\circ$, the dynamic lift requirement is not.

Table 2. Baseline performance, $\alpha = 0^\circ$

	IBL-Neg.	Objective
Displacement	20.4 LT	> 20 LT
Total lift	49.3 LT	= 60 LT
$C_{p,min}$	-0.337	> - 0.354
L/D	10.38	Maximum

1.2. Hull shape representation

1.2.1 Parametric representation

Each individual component of the configuration (H-body, strut, and cross-foil) is represented by a set of parameters, and once assembled, these components describe the entire twin-H configuration. Simple geometrical parameters, such as width, length, chord, etc., are used to characterize the elements. Foil cross-sections are defined by their mean camber line and thickness distributions. Camber is parameterized by classical NACA 2-parameter camber [11]. The thickness distribution, y_{th} , is represented by a 6-deg. polynomial, with an additional term for controlling the leading edge radius:

$$y_{th}(x) = a_0 \sqrt{x} + \sum_{i=1}^6 a_i x^i, \quad 0 \leq x \leq 1 \quad (8)$$

¹ From Navatek, Ltd., HI

Center for the Commercial Deployment of Transportation Technologies

Table 3 presents the parameters, which are used to define each component and their relative placement. These parameters are defined in three Pro-Engineer files, corresponding to each individual component. The values for the baseline configuration are shown. The polynomial coefficients were determined to best match the profiles of the baseline twin H-body configuration supplied by Navatek, Ltd. Fig. 14 shows the individual components before assembly.



Figure 15. Components of the twin H-body configuration, (a) cross-foil, (b) H-body, and (c) strut.

Table 3. Parameters defining each component and their relative placement

<i>PARAMETER NAME</i>	<i>DESCRIPTION</i>	<i>BASELINE</i>
Hbody.ptr		
Hchord	Chord length of H-body (in meters)	6.19591
Hwidth	Width of H-body (in meters)	1.17590
Hthick	Thickness ratio (thickness/chord)	0.10000
T0	A0 for H-body (Eq. (8))	0.83540
T1	A1 for H-body (Eq. (8))	4.04445
T2	A2 for H-body (Eq. (8))	-22.16024
T3	A3 for H-body (Eq. (8))	80.98612
T4	A4 for H-body (Eq. (8))	-156.34020
T5	A5 for H-body (Eq. (8))	134.85237
T6	A6 for H-body (Eq. (8))	-42.21789
Camber_m	Maximum camber ratio (max_camber/chord)	0.01100
Camber_p	Relative location of maximum camber (max_camber_loc/chord)	0.46712
Hstrutpcspan	Relative spanwise location of strut on H-body (spanwise_strut_loc/chord)	0.11645
Hstrutpcchord	Relative chordwise location of strut ¼ chord (chordwise_strut_loc/chord)	0.01000
Hbodyspan	H-body spanwise location measured from strut centerline at ¼ chord from mid plane of model (in meters)	3.65760
Hbodyangle	Angle of H-body. Angle can be positive or negative. A positive angle gives a nose down attitude to the H-body (in degrees)	0.00000
Hbodydepth	Clearance of the H-body relative to the undisturbed sea surface (in meters)	1.90660
Hcrosspcchord	Chord location of the ¼ chord of the cross-foil relative to the H-body chord	0.06500
Hextra	Internal parameter related to the wakes (not changed)	0.00100
Hbi	Ratio of inner ellipse side width relative to height	1.00000
Hbo	Ratio of outboard ellipse side width relative to height	1.00000

Center for the Commercial Deployment of Transportation Technologies

Crosswing.ptr		
Crossthick	Thickness-to-chord ratio of the foil	0.05441
Crosschordi	Chord of inner (center line) foil (in meters)	1.52400
Crosschordo	Chord of outboard foil (in meters)	1.52400
Crosstwisti	Twist of foil at inboard position (in degrees). Angle can be positive or negative. Positive angle causes a nose down rotation of the airfoil.	0.00000
Crosstwisto	Twist of foil at outboard position (in degrees). Angle can be positive or negative. Positive angle causes a nose down rotation of the foil.	0.00000
U0	A0 for cross-foil (Eq. (8))	1.25985
U1	A1 for cross-foil (Eq. (8))	3.41325
U2	A2 for cross-foil (Eq. (8))	-17.29867
U3	A3 for cross-foil (Eq. (8))	46.08449
U4	A4 for cross-foil (Eq. (8))	-71.88818
U5	A5 for cross-foil (Eq. (8))	54.29078
U6	A6 for cross-foil (Eq. (8))	-15.86151
Camber_m	Maximum camber ratio (max_camber/chord)	0.02000
Camber_p	Relative location of maximum camber (max_camber_loc/chord)	0.43058
Strut.ptr		
Strutchord	Chord length of strut (in meters)	2.30100
s0	A0 for strut (Eq. (8))	2.25913
s1	A1 for strut (Eq. (8))	0.18280
s2	A2 for strut (Eq. (8))	-6.38813
s3	A3 for strut (Eq. (8))	10.28311
s4	A4 for strut (Eq. (8))	-1.59661
s5	A5 for strut (Eq. (8))	-12.70745
s6	A6 for strut (Eq. (8))	7.96715
Camber_m0	Maximum camber ratio near H-body (max_camber/chord)	0.00000
Camber_m1	Maximum camber ratio near sea surface(max_camber/chord)	0.00000
Camber_p	Relative location of maximum camber (max_camber_loc/chord)	0.30000
Strutthick	Thickness-to-chord ratio of the foil	0.05000

1.2.2. Meshing, including extra-strips

Once the configuration is defined in the CAD model, using the “Promif” module between *Pro-Engineer* and *ICEM-CFD*, the geometry, and additional points and curves needed for the mesh generation, are transferred to the grid generation software, or mesher, *ICEM-CFD*. In the present case, since the negative image option is used, the free surface does not need to be represented. However, since the IBL method employs a boundary layer calculation extending to the far field, wakes must be attached to the lifting surfaces and extend several chords downstream of the lifting surfaces. Fig. 15 shows the resulting paneling distribution on the twin H-body configuration. The resulting configuration is comprised of:

Center for the Commercial Deployment of Transportation Technologies

- Four (4) lifting sections:
 - Cross-foil
 - Strut
 - Inner H-body
 - Outer H-body
- Several non-lifting sections describing the caps, both inner and outer

In order to ensure continuity of the vortex sheet at the junction between two or more lifting sections, “extra-strips” are used to link the sections. The additional panels carry vorticity, but do not carry sources. This approach has been used extensively and successfully in the Hess panel method (which is the base of the inviscid flow calculation) for modeling the intersection of lifting components, e.g. wing pylon. It is used here for the cross-foil/H-body and the outer-H-body/strut/inner-H-body intersections.

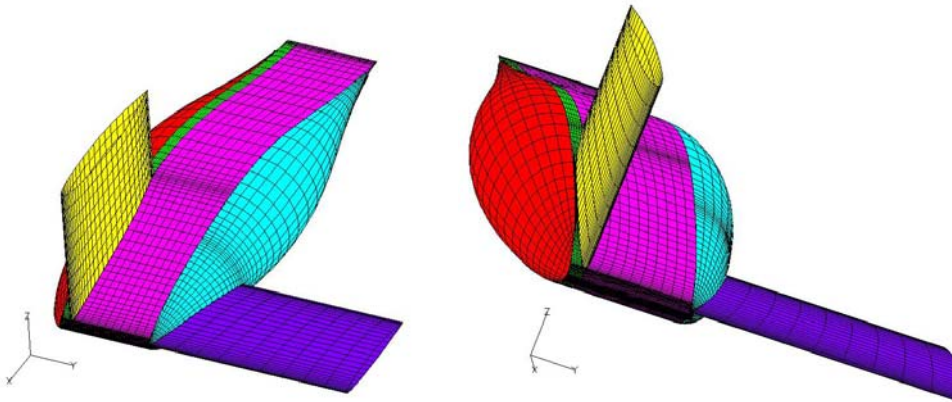


Figure 16. Paneling distribution on twin H-body configuration

1.2.3. Parameterization of foil cross-sections for optimization

One of the issues associated with the use of polynomials for thickness representation is the fact that a rather small disturbance in one or more of the coefficients may result in an unsuitable wavy profile. To avoid this problem during optimization, the foil cross-section is represented by “geometrical” parameters, which define, a priori, a suitable foil, and “compatibility relations” between these parameters and the polynomial coefficients is derived. The following four parameters are the resulting design variables:

- $a_0 = \sqrt{2r_0}$, where r_0 is the leading edge radius
- a_1 , which is a parameter related to the airfoil shape near the nose since $a_1 = \left. \frac{d(y/\sqrt{x})}{d(\sqrt{x})} \right|_{x \rightarrow 0}$
- γ : slope at trailing edge with respect to horizontal
- x_m : location of maximum thickness, $0 < x_m < 1$

Center for the Commercial Deployment of Transportation Technologies

Two additional relations close the problem:

- $y_{th} = 0$ in $x = 1$
- The term in $(1 - x)^2$ is 0 at the trailing edge ($x = 1$) so that the foil is linear at the trailing edge
- $y_{th} = th/2$ at x_m . Here, the thickness ratio is controlled in the Pro-Engineer parameter file (see Table 3) so that $th/2$ is set to 1.

Table 4 presents the parameter definition corresponding to the foil cross-sections of the strut, H-body and cross-foil.

Table 4. Foil cross-section parametric definition

Parameter	Description	Hbody	Crosswing	Strut
Gamma	γ	52.56463	74.34601	69.91842
R0	r_0	0.34894	0.79361	2.55183
Xm	x_m	0.44276	0.44249	0.46392
Alpha	α	-2.09216	-5.54668	7.03191

The entire process, from definition of independent parameters to the generation of a mesh suitable for the CFD method, is implemented in batch and does not require the intervention of the user. This automatic implementation is described in Sect. 1.4.

1.3. Optimization method

In the development of the method, three distinct features of *iSIGHT* can be used:

- Design of Experiments (DOE): Latin hypercubes
- Parametric studies
- Optimization: Genetic Algorithm

DOE was used to verify that the model could be varied and that the solution process would work. In addition, it allowed determining the limits of the model before setting up the optimization process. These limits are reached when, for example, geometrical parameters lead to an unfeasible geometry. A trivial example would be if the cross-foil angle of attack ends up so high that the grid at the cross-foil/H-body intersection gets skewed or twisted. The choice of Latin Hypercubes is discussed below.

Parametric studies were also conducted, for the primary purpose of obtaining preliminary information regarding the relative role played by the various design variables.

Finally, Genetic Algorithm was selected for conducting the optimization because of its robustness and generality. In addition, the use of the negative image approach in the CFD allows for reduced computer time for each function evaluation (approximately 6 minutes per cycle on a single SGI Origin 3000 processor) and makes the use of GA practical. Genetic Algorithms are described below.

1.3.1. Latin Hypercubes

Latin hypercubes offer an efficient way of sampling large design spaces. In this technique, the design space is uniformly divided in n divisions along each direction. These levels are then randomly combined to specify n point defining the design matrix.

In this approach, each level of a given direction is explored only once. Fig. 17 shows the case for two directions, X1 and X2 in which 5 points are studied. An advantage of this sampling method is that the designer has the freedom in selecting the number of designs to run (as long as it is greater than the number of factors). On the other hand, they have the disadvantages of not being reproducible (based on random factors) and, as the number of points increases, the chances of missing regions of the design space increase.

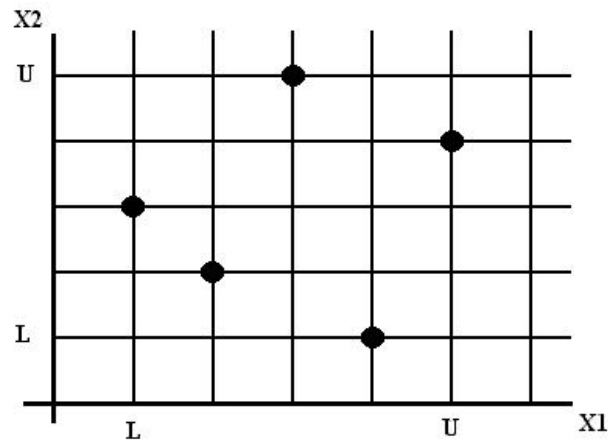


Figure 17. Latin hypercube sampling

1.3.2. Genetic Algorithms

Genetic Algorithms (GA) were introduced by J. Holland [13], who expressed the two main principles of GA, (1) the string representation of complex structures, and (2) the power of simple transformations acting on the strings to improve these structures. Further developments have been made by Goldberg [14], who introduced *fitness functions*. The main advantages of GA are their robustness and simplicity. They cope easily with discontinuous, rough, or multi-modal functions, and make an interesting tradeoff between diversification (exploration of the search space) and intensification (exploitation of the results).

The first step in SA is to encode a point x of the search space as a fixed- and finite-length string. This can be a binary or real string, but this choice has some consequences on the implementation of the algorithm, as will be explained later. An initial population made out of n of these strings is then created.

Then, a set of operators acting on these strings (selection, reproduction, mutation, crossover) is created. Selection is a stochastic process that consists of choosing the elements of the current population that will have an offspring. This process is based on the fitness function (the objective

Center for the Commercial Deployment of Transportation Technologies

function). Reproduction is a process by which a string is copied with no modification in the next population, and mutation randomly modifies parts of the string. Finally, crossover acts on two strings and exchanges parts of them with the objective of gathering interesting parts of different strings in the same one. When the string is binary, crossover can create new values of the coordinates of elements of the search space, since it can cut “within” numbers, whereas cuts can only occur between parameters if the string is real. In this case, mutations are necessary because they are the only operator allowing the exploration of the search space.

Iterations are performed until convergence is reached.

1.4. Integration into design/optimization tool

As previously outlined, the optimizer, *iSIGHT* controls the process and calls the scripts, which, ***from the design variables***,

1. Defines the geometry (Pro-Engineer),
2. Generates a suitable mesh (ICEM-CFD),
3. Executes the CFD method (IBL-Neg.), and
4. Extracts the data needed by *iSIGHT* (***objective function and constraint values***) for the next iteration.

Once *iSIGHT* is setup, the *iSIGHT* process can be chosen among design of experiments, parametric studies, or optimization, with the click of a button. The key, therefore, resides in linking the components of the method in an automatic and robust fashion. Fig. 17 shows the overall process as controlled by *iSIGHT* and shows the sequence of events.

Center for the Commercial Deployment of Transportation Technologies

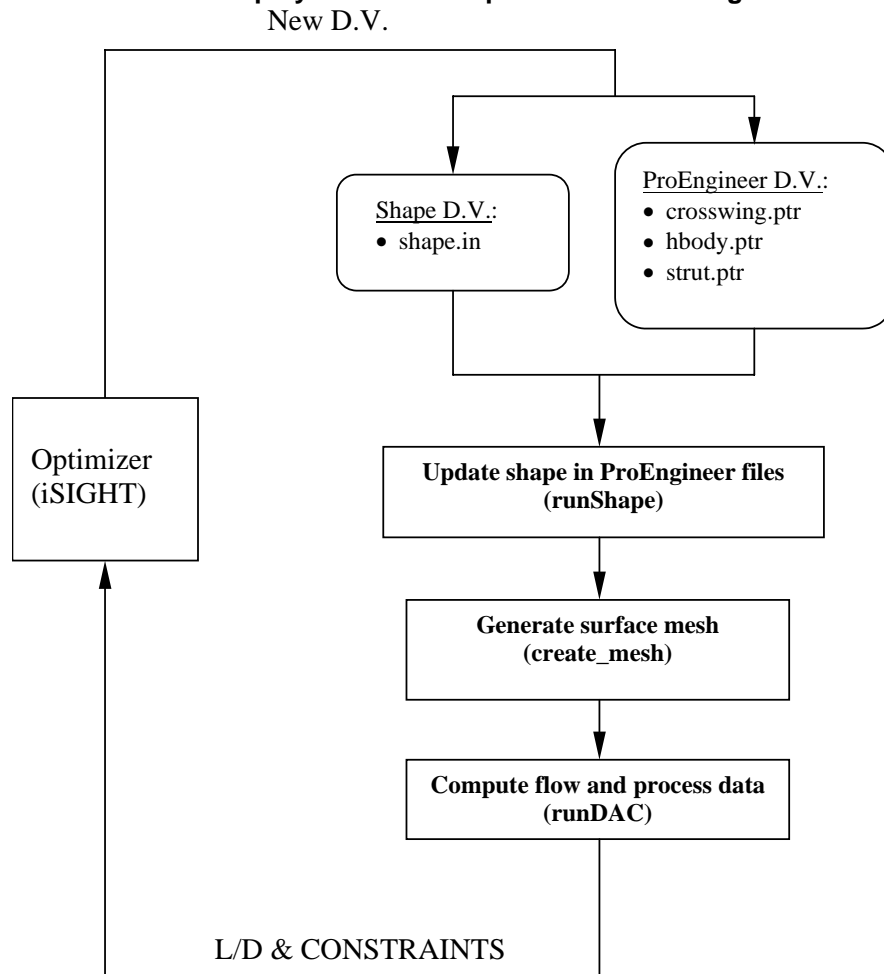


Figure 18. Optimization process

The values for the design variables are decided by *iSIGHT*, which then updates the files used for generating the configuration. These include the *Pro-Engineer* files (*.ptr) and the file which controls the shape of the component cross-sections (*shape.in*; see Table 4). These are fed into *runShape* which updates the part of the *Pro-Engineer* files corresponding to the cross-section definition (mainly T0, etc.; see Table 3). Then, from the *Pro-Engineer* files, *create_mesh* generates the CAD model into *Pro-Engineer* (in batch) as well as other information needed for generating the mesh, volume information, etc. *create_mesh*, continues by calling *ICEM-CFD* to generate a grid. This grid is then formatted by *runDAC* to fit CSULB's IBL method with negative images. *runDAC* continues with the flow calculation with the CFD method and concludes with the post-processing of the data to extract displacement (buoyant lift), total lift, drag, minimum pressure (for cavitation constraint), etc. This data is then fed back to *iSIGHT* for the next iteration.

Figures. 19 through 21 give one additional level of detail by providing the flow of data and processes occurring within each of the three scripts, *runShape*, *create_mesh*, and *runDAC*. Figure. 19 shows that the *Pro-Engineer* files (*.ptr) are updated to reflect the information in *shape.in*. Figure. 20 shows the process used to go from these *Pro-Engineer* files to a surface mesh in a format suitable for the wave code of Sect. 2. This format is then modified to be

Center for the Commercial Deployment of Transportation Technologies

suitable for the IBL code (see Fig. 21). The code is run part of *runDAC* and the data is extracted from the various output files by *drag_v3.x* (Fig. 21).

It is important to note that the files listed in these figures are only a small portion of the files required for setting up and running the process. Additional files, such as input data for grid distribution, for CFD code, etc. are also needed.

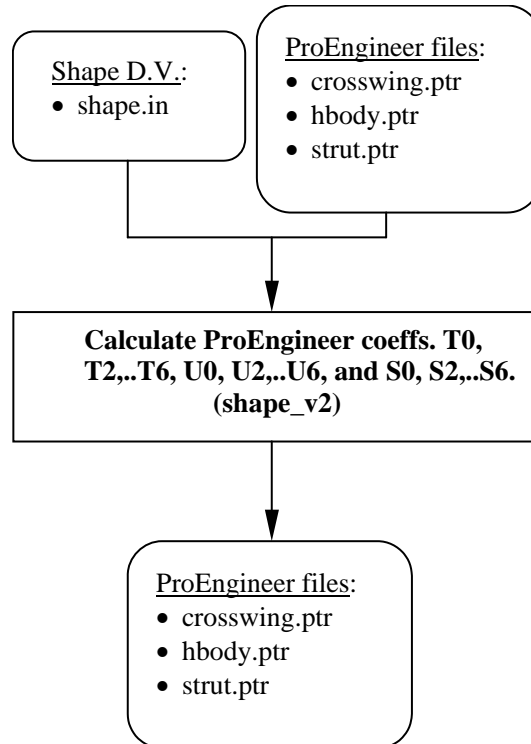


Figure 19. From design variables to Pro-Engineer files – *runShape*

Center for the Commercial Deployment of Transportation Technologies

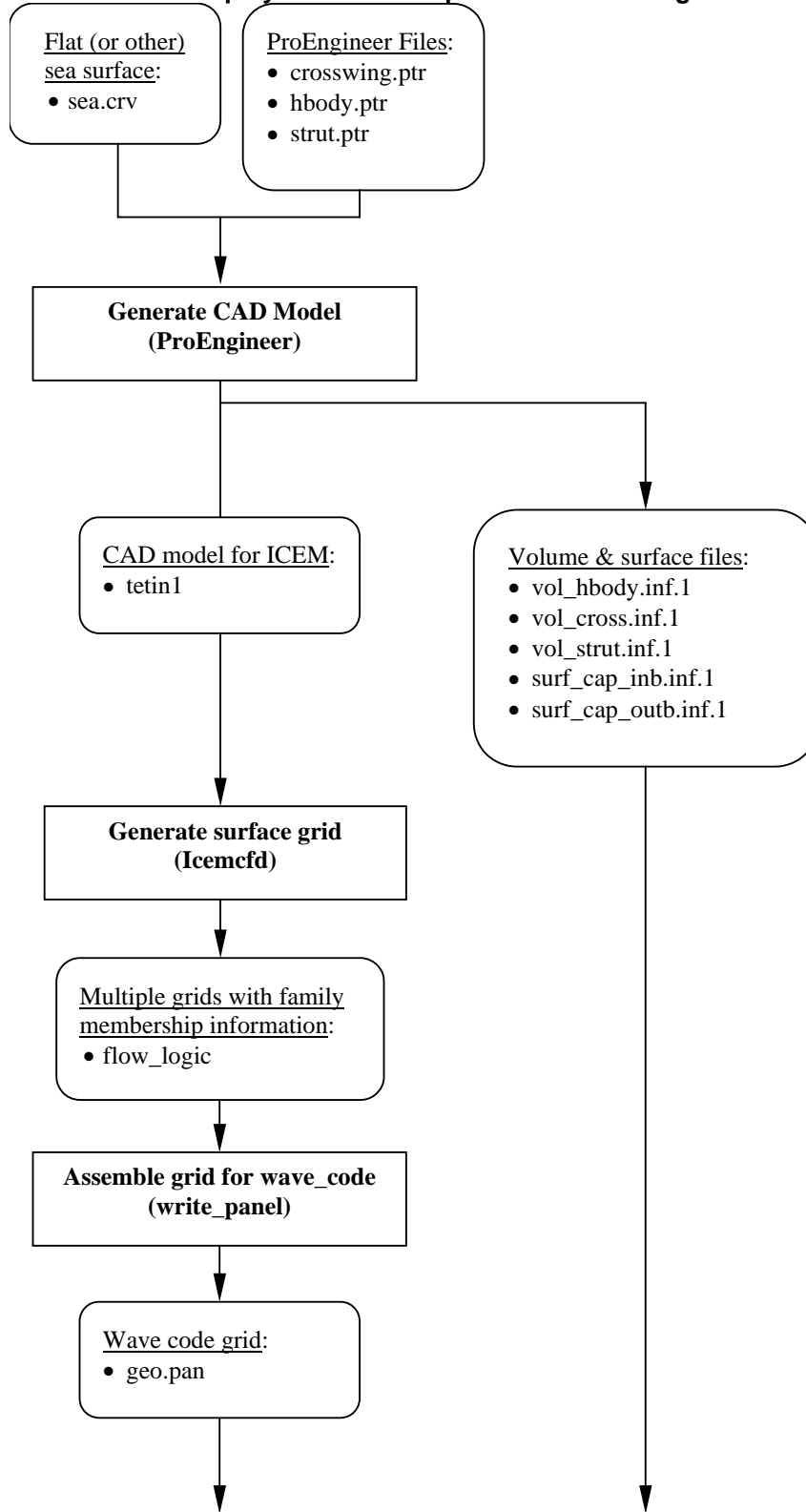


Figure 20. From Pro-Engineer files to surface mesh – *create_mesh*

Center for the Commercial Deployment of Transportation Technologies

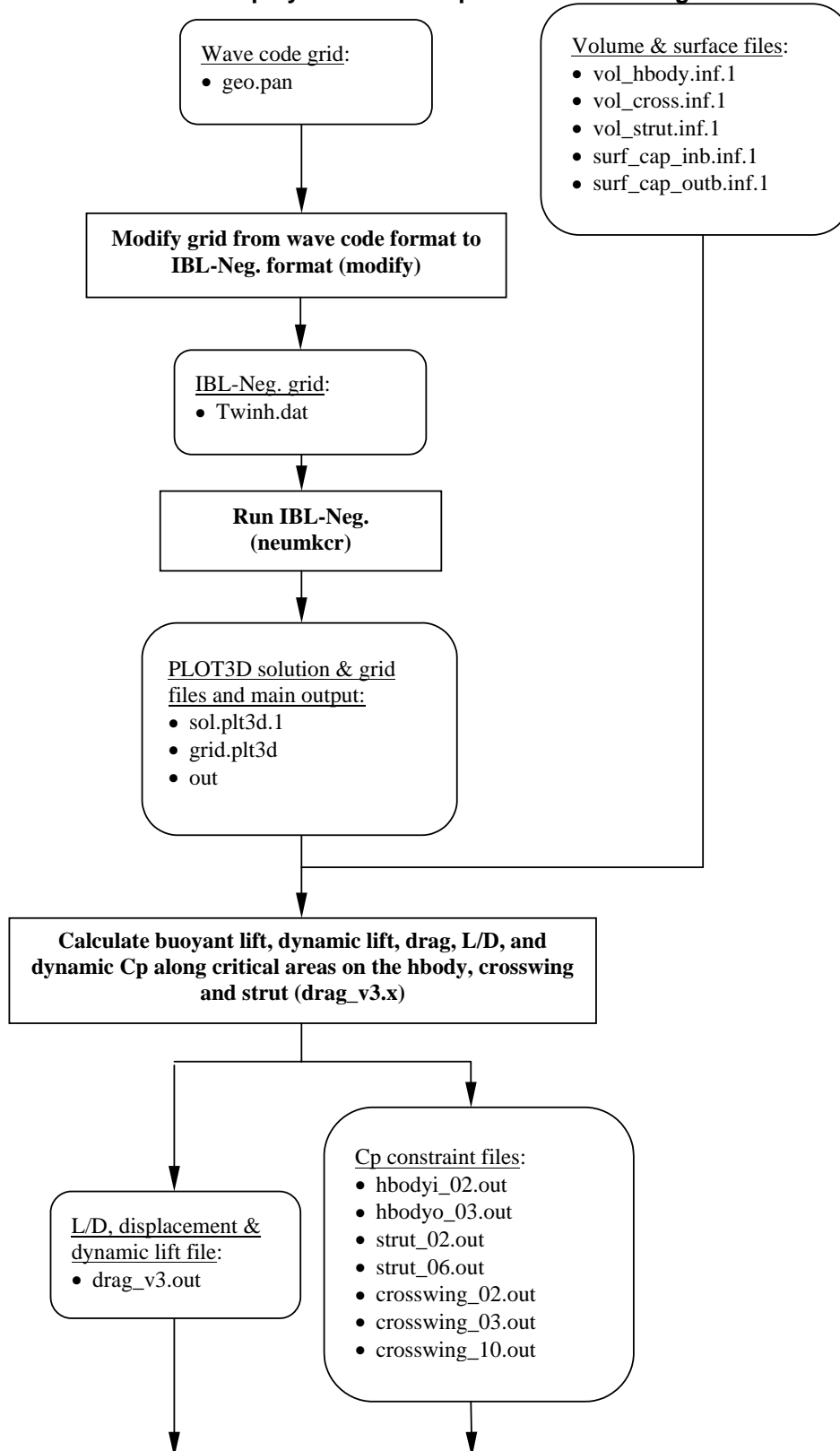


Figure 21. From surface mesh to flow solution, objective function and constraint determination – *runDAC*

Center for the Commercial Deployment of Transportation Technologies

1.5 Tests and application: twin H-body optimization

The method of Sect. 1.4 is applied here to the design/optimization of the twin H-body configuration shown in introduction to this section.

1.5.1. *Problem setup*

As stated in introduction to Sect. 1, the objective of the optimization is to maximize L/D of the twin H-body configuration subject to the following constraints:

- Cavitation free at 45 knots, i.e. $C_p > -0.357$ (Hawaii water at 75 F)
- Total lift equal to 30 LT
- Displacement greater than 20 LT
- The span (location where strut and H-body intersect) is fixed at 7.315 m and the strut and cross-foil must be aligned for structural reasons.

The performance of the baseline configuration is given in Table 2.

1.5.2. *Design of Experiment (DOE)*

In order to validate the method, and in particular in order to verify its implementation, two design of experiments (DOE) were conducted, at first with 3 and then with 16 parameters among the *Pro-Engineer* parameters. In some cases, DOE can provide a simple way to explore the search space and determine improved designs. In this case, however, increases in lift often lead to improved L/D , but most often, the cavitation limit is surpassed so that the design with improved L/D is not feasible. For this reason, the use of DOE was not pursued further.

1.5.3. *Design variables*

The next step is to actually identify design variables among all parameters. For the parametric representation of Sect. 1.2, a set of 34 design variables can be identified. The 34 design variables are shown in Table 5 along with the interval over which they were allowed to vary. This interval was determined by a compromise between size (large but not necessarily too large to avoid a prohibitively large design space), and model capability (i.e. leading to designs for which the grid can be generated by the model). The variables are defined in Tables 3 and 4.

Table 5. Design space

<i>PARAMETER NAME</i>	<i>MIN</i>		<i>BASELINE</i>	<i>MAX</i>
Hbody.ptr				
Hchord	4.00000	<	6.19591	< 9.00000
Hwidth	0.50000	<	1.17590	< 2.00000
Hthick	0.06000	<	0.10000	< 0.15000
T1	0.00000	<	4.04445	< 10.00000
Camber_m	0.00000	<	0.01100	< 0.03000
Camber_p	0.10000	<	0.46712	< 0.70000
Hstrutpcspan	0.10000	<	0.11645	< 0.90000
Hstrutpcchord	0.01000	<	0.01000	< 0.70000
Hbodyangle	-3.00000	<	0.00000	< 3.00000

Center for the Commercial Deployment of Transportation Technologies

Hbodydepth	1.80000	<	1.90660	<	2.00000
Hcrosspcchord	0.04000	<	0.06500	<	0.40000
Hbi	0.50000	<	1.00000	<	1.50000
Hbo	0.50000	<	1.00000	<	1.50000
Shape.in for Hbody					
Gamma	10.00000	<	52.56463	<	85.00000
R0	0.10000	<	0.34894	<	3.00000
Xm	0.10000	<	0.44276	<	0.70000
Alpha	-20.00000	<	-2.09216	<	20.00000
Crosswing.ptr					
Crossthick	0.03000	<	0.05441	<	0.07000
Crosschordi	1.00000	<	1.52400	<	3.00000
Crosschordo	1.00000	<	1.52400	<	3.00000
Crosstwisti	-3.00000	<	0.00000	<	3.00000
Crosstwisto	-3.00000	<	0.00000	<	3.00000
U1	0.00000	<	3.41325	<	10.00000
Camber_m	0.00000	<	0.02000	<	0.05000
Camber_p	0.10000	<	0.43058	<	0.60000
Shape.in for Crosswing					
Gamma	10.00000	<	74.34601	<	85.00000
R0	0.10000	<	0.79361	<	3.00000
Xm	0.10000	<	0.44249	<	0.70000
Alpha	-20.00000	<	-5.54668	<	20.00000
Strut.ptr					
S1	0.00000	<	0.18280	<	10.00000
Shape.in for Strut					
Gamma	10.00000	<	69.91842	<	85.00000
R0	0.10000	<	2.55183	<	3.00000
Xm	0.10000	<	0.46392	<	0.70000
Alpha	-20.00000	<	7.03191	<	20.00000

1.5.4. Parametric study

The next step was to perform a trade study around the baseline design. The design variables were varied one by one of 1% from the baseline and the percentage change, in absolute value, in L/D was determined. If the variables were initially zero (case of most angles), they were varied of a small quantity (1 deg. for the angles). This approach enables to determine which variables play a key role in changes in L/D around the baseline design. Figs. 22 and 23 show the bar chart for the variables modified by 1% and 1 deg., respectively.

The cross-foil camber is the parameter, which has the largest influence on L/D . This remark is consistent with the fact that increasing the lift without increasing wetted area leads to larger L/D . The role played by other parameters is subtler. For the angles (Figure. 23), a similar observation can be made. Twisting the cross-foil increases the local angle of attack, and therefore increases

Center for the Commercial Deployment of Transportation Technologies

lift, with greater effect near the middle of the foil than near the H-body. Again, since for lifting configurations L/D is approximately a linear function of L , increasing L should increase L/D if the wetted area remains unchanged. A similar remark holds for the H-body angle.

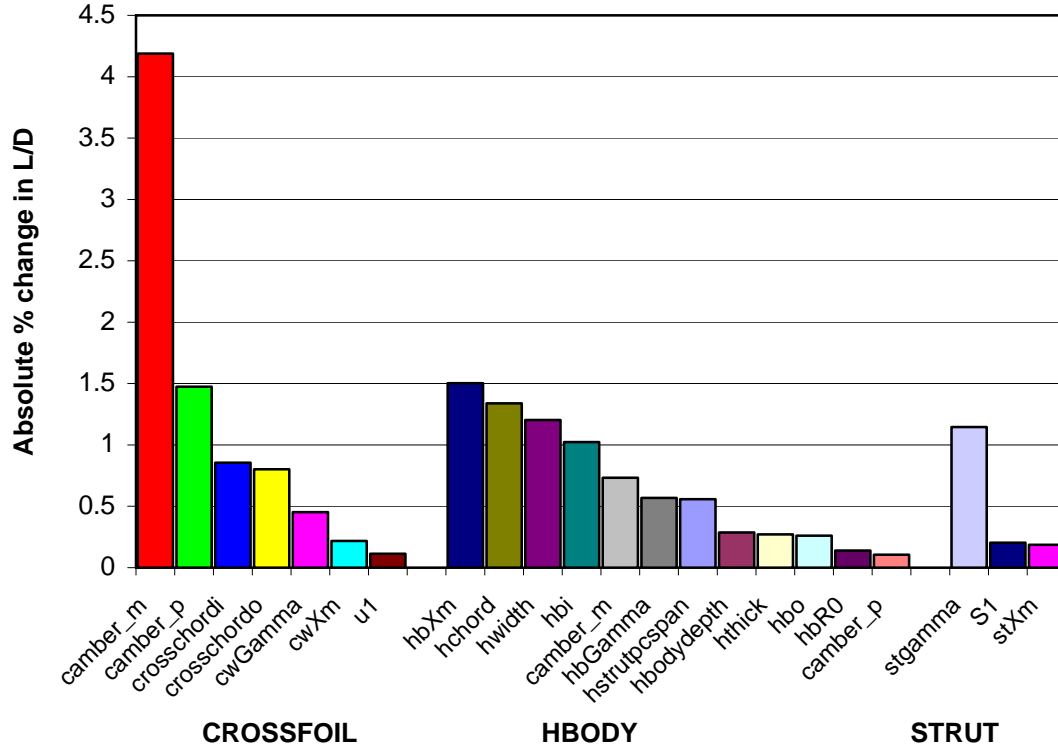


Figure 22. Absolute percentage variation in L/D for 1% change in design variable

Center for the Commercial Deployment of Transportation Technologies

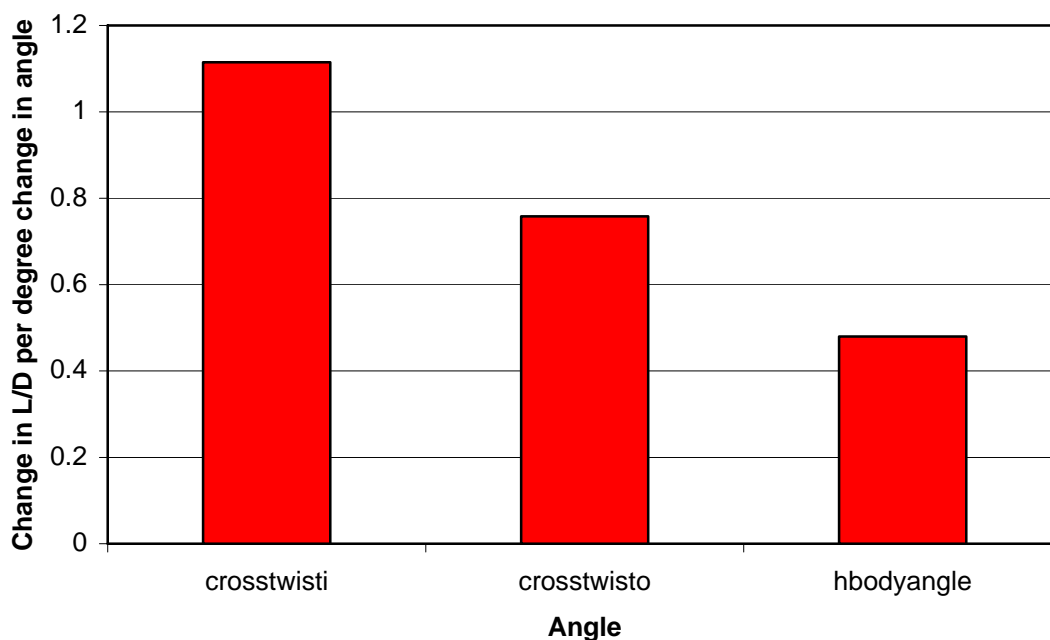


Figure 23. Absolute percentage variation in L/D for a 1 deg. change in angle

1.5.5. Genetic algorithm optimization

In order to obtain an improved configuration, which would satisfy the constraints, a Genetic Algorithm optimization was applied to the twin H-body configuration by varying all 34 design variables. This method was chosen over local optimization methods because for such large dimensional design spaces, functions typically exhibit many local minima in which the local method gets trapped. The optimization was run over a period of 10 days on a single Origin 3000 processor. During this 10-day period, a total of 2000 iterations were run, for a single run average of approximately 7 minutes. These 7 min. include approximately 1 to 1.5 min. needed for generating the grid, and most of the rest is used by the CFD method. The analysis of the results showed that running the GA longer would not improve drastically the objective function because the amount of buoyant lift needed does not allow for L/D ratio much larger than 12.

A large amount of computer time is spent in data input/output (I/O) to a hard disk, which is typical of panel methods where the *full* matrices needed in the calculation are too large to be held in core memory (although 4 GB was available) and must be dumped to files. This is particularly true for the present IBL method. In order to satisfy the so-called off-body Kutta-condition (due to viscous effects the Kutta-condition is satisfied at the displacement thickness), several thousand off-body points are added and appear in the matrices. Therefore, although the resulting memory requirements are then relatively low, the I/O requirements are significant and prevent from being able to run several simultaneous flow computations on the same server. For the present application, workstation clusters would have to be used in order to parallelize the calculation process and lead to overall significant computer time savings required to get an improved design.

Center for the Commercial Deployment of Transportation Technologies

With the GA optimization, the **lift-to-drag ratio was improved by about 17%** from the baseline value. Table 6 shows the parameters defining the optimized configuration and compares them with those of the baseline design. The performance values obtained for the objective function and the constraints are shown in Table 7. Recall that the baseline configuration did not meet the requirement of generating a total lift of 60 LT. The optimization handled the violated constraint and brought the total lift to a value within the specified constraint margin. At the same time, the minimum pressure coefficient on the body stayed within the desired limit to prevent cavitation (at 45 knots).

Figures. 24 and 25 show the dynamic pressure coefficient (C_{pd}) on both the baseline and the optimized model. The baseline is at the top half of each figure. Fig. 24 is a top view and Fig. 25 a bottom view. The result of the optimization is that the H-body is longer and narrower, which increases the cross-foil span and thus the dynamic lift as needed to get from 50 to 60 LT. Also, by improving the cross-foil profile and adding a little twist, the C_{pd} is lower on its upper surface and higher on its lower surface for the optimized configuration. This further increases the dynamic lift. On the H-body, the optimizer lowered the acceleration of the flow on both the upper and lower surfaces by thinning and improving its profile. This reduces the drag from the H-body. Note that the H-body carries most of the buoyant lift, and the cross-foil mainly carries the dynamic lift.

Also, as mentioned above, the strut thickness and chord were kept constant for structural reasons.

Table 6. Optimized vs. Baseline Configuration Definition

<i>PARAMETER NAME</i>	<i>BASELINE</i>	<i>OPTIMIZED</i>
Hbody.ptr		
Hchord	6.19591	6.5137339
Hwidth	1.17590	1.1081280
Hthick	0.10000	0.0918970
T1	4.04445	4.6098819
Camber_m	0.01100	0.0065891
Camber_p	0.46712	0.4988000
Hstrutpcspan	0.11645	0.2757037
Hstrutpcchord	0.01000	0.0099998
Hbodyangle	0.00000	-0.0542934
Hbodydepth	1.90660	1.8936862
Hcrosspcchord	0.06500	0.0734024
Hbi	1.00000	1.000000
Hbo	1.00000	0.8509133
Shape.in for Hbody		
Gamma	52.56463	57.554775
R0	0.34894	0.3766045
Xm	0.44276	0.4427588
Alpha	-2.09216	-1.143852

Center for the Commercial Deployment of Transportation Technologies

Crosswing.ptr		
Crossthick	0.05441	0.0505900
Crosschordi	1.52400	1.5240117
Crosschordo	1.52400	1.5002218
Crosstwisti	0.00000	-0.0017898
Crosstwisto	0.00000	-1.3160000
U1	3.41325	2.2839397
Camber_m	0.02000	0.0200000
Camber_p	0.43058	0.4470897
Shape.in for Crosswing		
Gamma	74.34601	73.49530
R0	0.79361	0.794089
Xm	0.44249	0.421278
Alpha	-5.54668	-4.69262
Strut.ptr		
S1	0.18280	0.18633090
Shape.in for Strut		
Gamma	69.91842	64.690822
R0	2.55183	2.5519771
Xm	0.46392	0.4650965
Alpha	7.03191	7.1868400

Table 7. Performance of optimized vs. baseline configuration – IBL-Neg. method

	Baseline	Optimum	Objective
Displacement	20.4 LT	19.9 LT	> 20 LT
Total lift	49.3 LT	61.8 LT	= 60 LT
$C_{p,min}$	-0.337	-0.350	> - 0.354
L/D	10.38	12.11	Maximum

Center for the Commercial Deployment of Transportation Technologies

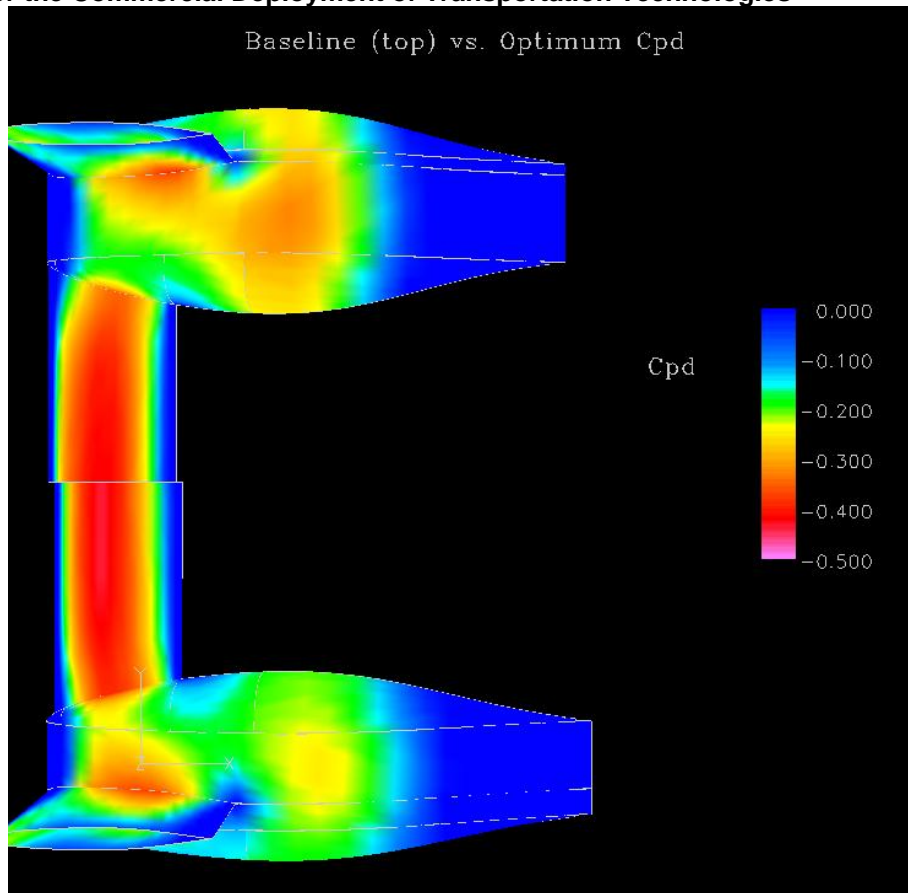


Figure 24. Dynamic pressure comparison between the baseline (top half of the picture) and optimized configuration (bottom half). *Top View*

Center for the Commercial Deployment of Transportation Technologies

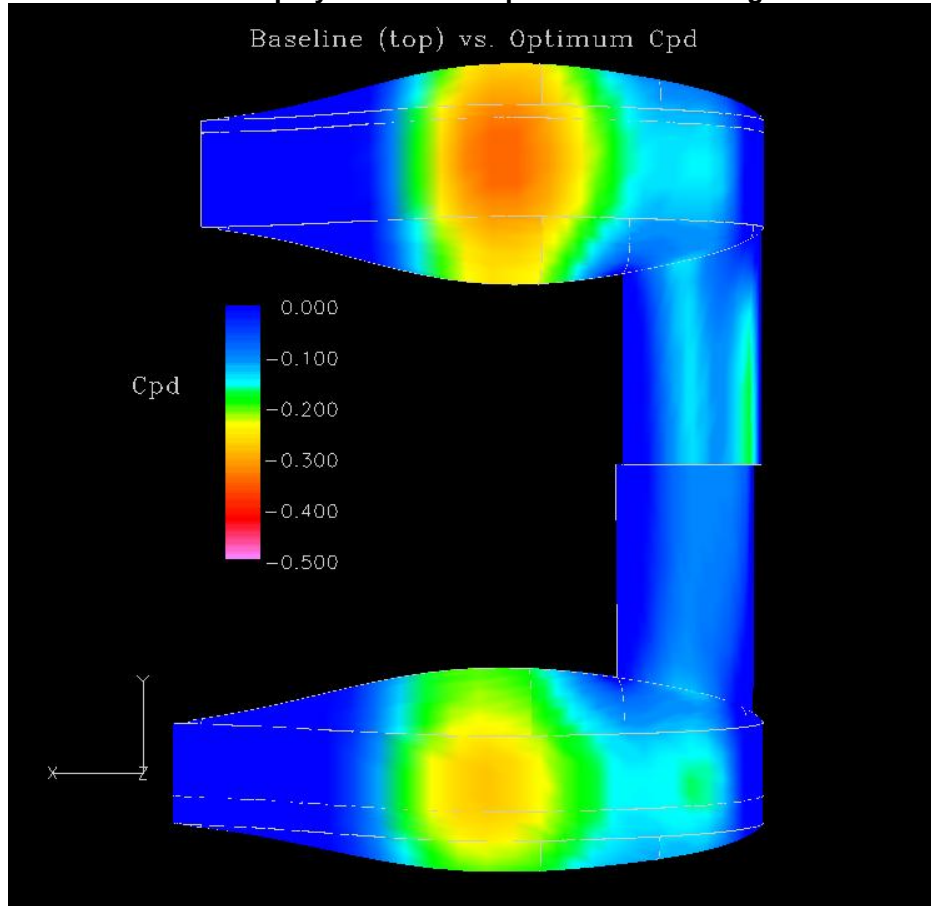


Figure 25. Dynamic pressure comparison between the baseline (top half of the picture) and optimized configuration (bottom half). *Bottom View*

1.5.6. Validation of optimum

The results reported above stem from the optimization performed with the IBL-Neg method, which employs the negative image approach to model the free surface effects. In order to ensure that the negative image method models the flow appropriately, the flow over the optimized configuration was also calculated using the free surface method being developed at CSULB (“Wave”, see Chapter 2). Figs. 26 and 27 show the dynamic pressure distribution at two cross-sections of the cross-foil (near the plane of symmetry and near the foil/H-body junction) and at two H-body cross-sections, inboard and outboard of the strut, respectively. Results are shown for the IBL method with negative image (“IBL-Neg.”), for the free surface method (inviscid: “Wave code”) and for USAERO². As mentioned before in the discussion of results of Table 1, while the IBL-Neg and our Wave Code show very consistent results, there are some differences between our results and those results obtained by Pacific Marine (Navetek Ltd) for the same geometry using USAERO.

USAERO uses an unsteady formulation to solve the free surface problem as does the Wave Code that is being developed and applied at CSULB under this contract, although the details of this iteration, and the way the free surface boundary condition is imposed by USAERO, substantially

² Results provided by Navatek, Ltd., HI

Center for the Commercial Deployment of Transportation Technologies

differ from our Wave Code. Also, USAERO uses a surface doublet singularity distribution on the body surface to solve the potential flow problem, rather than the surface source singularities used in the Wave Code. A Green's identity formulation is used to compute the required doublet strengths for each panel. Unlike our method, this formulation does not automatically require the use of extra strips to handle the carry over of lift from one section to another. However, a Kutta condition is still required for such lift carry over strips. The correct treatment is particularly important for the shapes such as the "body caps" in the TwinH geometry which don't have a well-defined Kutta point, but which are required to carry the lift over from the struts.

While the results obtained for the Twin H body, using these two codes, are similar, there are some differences. These differences are most pronounced in the intersection regions between the lifting sections, as well as the body caps region, where the handling of such lift carry over is different between the two codes. The reasons for these differences are currently under further investigation. They could be related to the above discussion, or surface grid densities used to represent the bodies that may not be optimum for one or both of the codes. More details are discussed in Chapter 2, under three-dimensional free surface method development.

Such differences in predicted results amongst different computational methods are not unusual, particularly for free surface problems such as this where the results are particularly sensitive to the computed wave shape. The best way to evaluate these results is with comparison with experimental (at sea-trials) data, which will be obtained, in the next phase of the program. At the present stage, the key to the successful implementation of computational methods to our optimization problems lies in the ability of the methods to correctly predict the effects of incremental design changes on the overall performance of the vehicle, which both the Wave Code and USAERO have indicated in these applications. When these incremental design changes are accurately captured, we can use the method with confidence in the design optimization process.

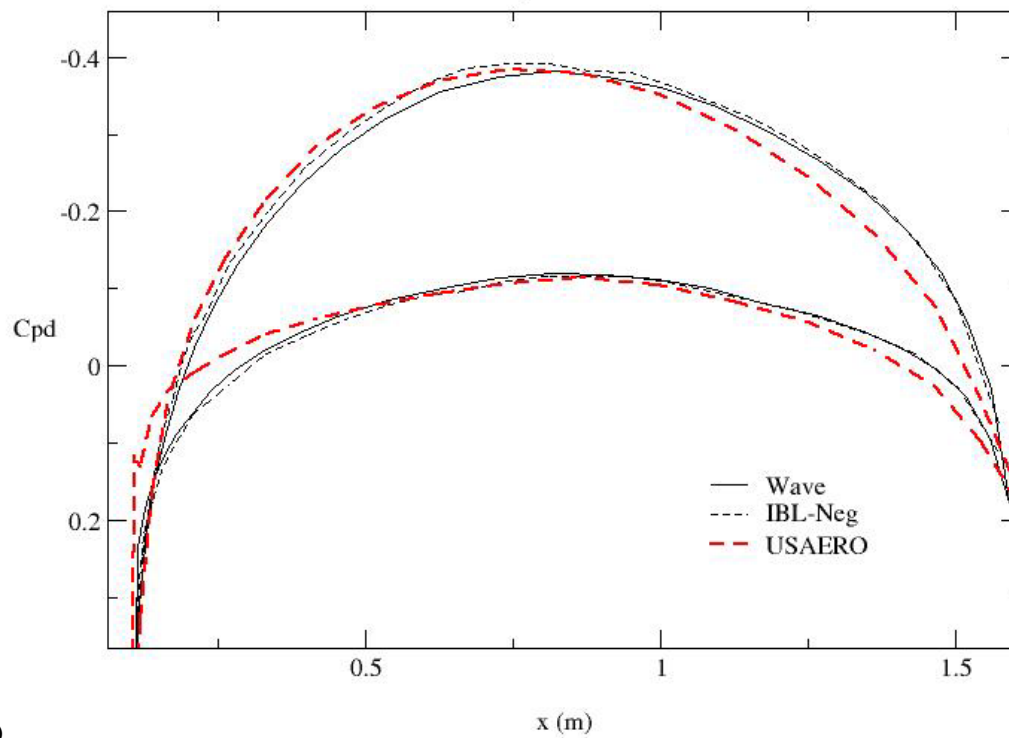
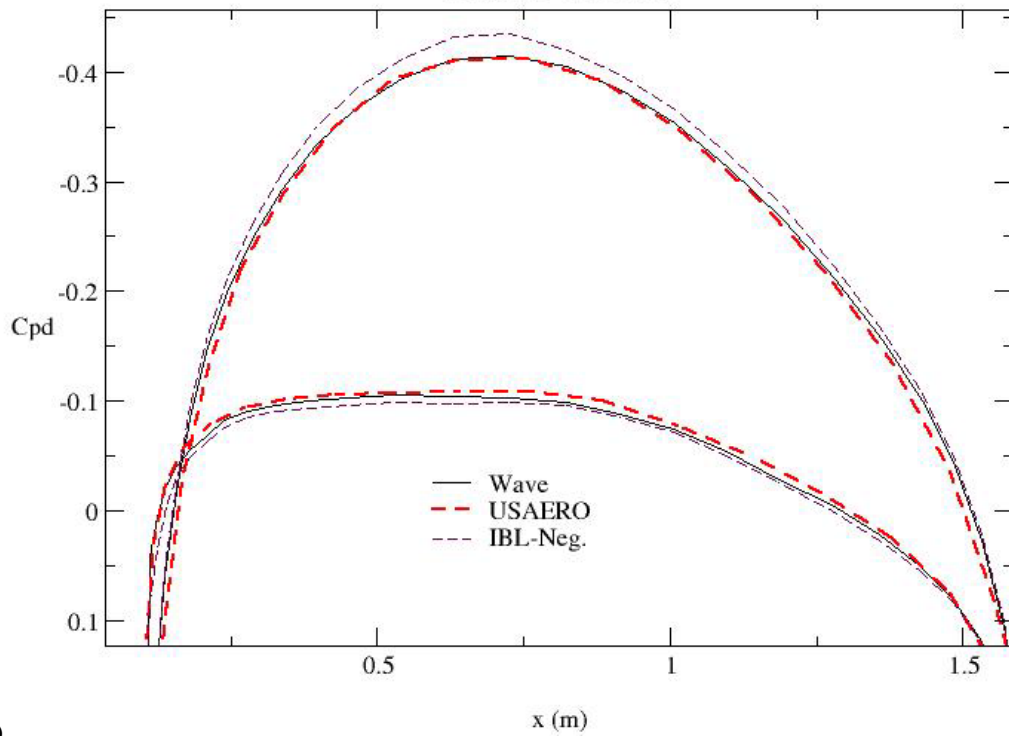
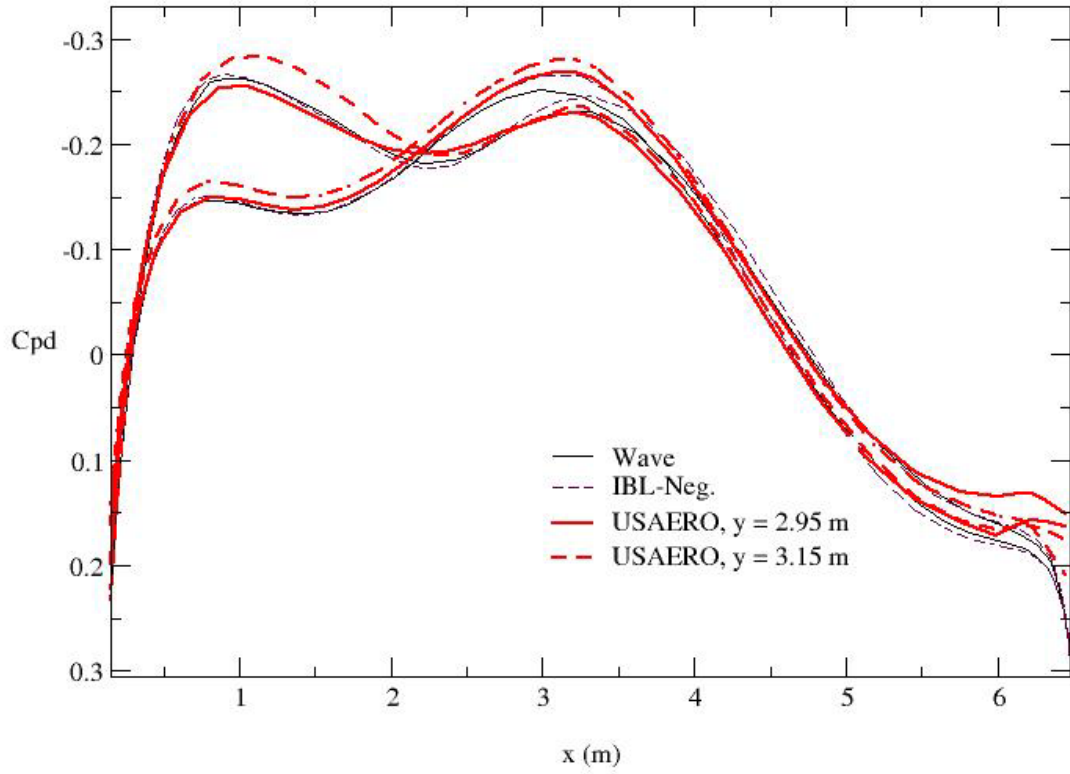
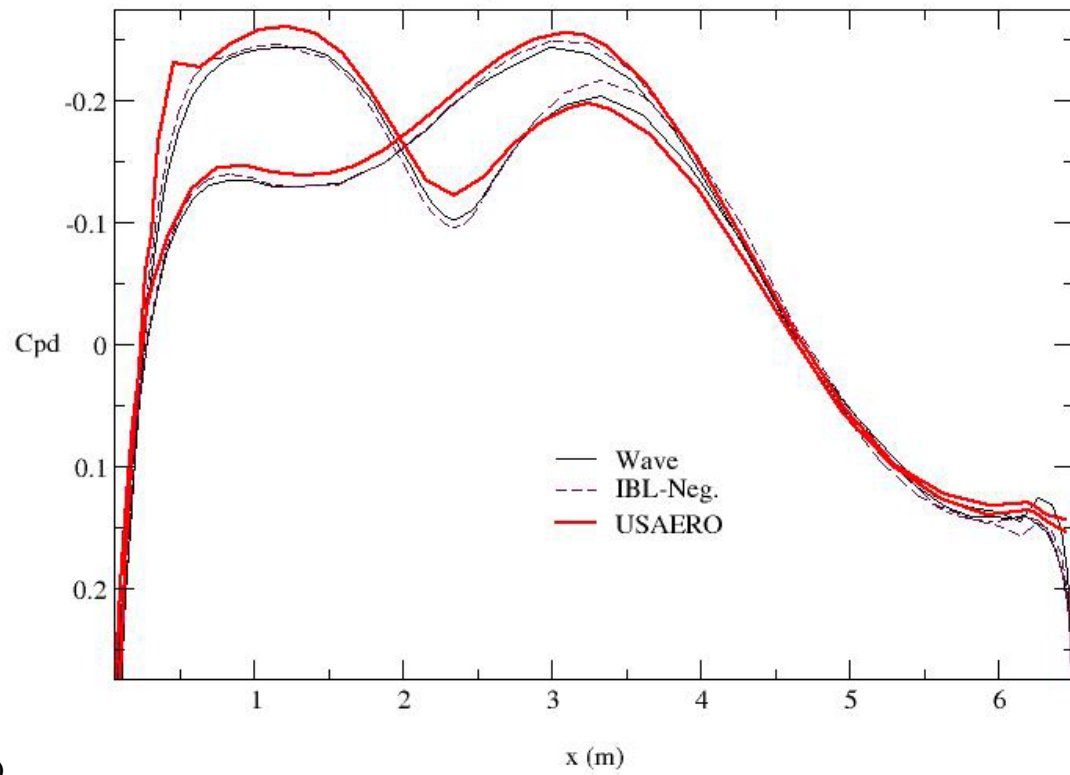


Figure 26. Pressure distribution on cross-foil at (a) $y = 0.4$ m (near center) and (b) $y = 2.22$ m (near junction with H-body)

Center for the Commercial Deployment of Transportation Technologies



(a)



(b)

Figure 27. Dynamic pressure distribution on H-body, (a) inner section ($y = 3.1$ m) and (b) outer section ($y = 3.9$ m)

Center for the Commercial Deployment of Transportation Technologies

Table 8 summarizes the improvements in L/D for both IBL and USAERO when compared with their respective baseline L/D values, shown in Table 1. It also shows how close the integrated pressure forces are for both the IBL and wave method. Obviously, since the initial lift was much lower with USAERO, the percentage increase in L/D is much larger (47%) than for the IBL method (17%). Nevertheless, the method is shown to yield significant improvements in both cases.

Table 8. Performance of optimized configuration with various CFD methods

	IBL-Neg.	Wave	USAERO
Total lift	61.84	59.46	49.19
L/D	12.11	N/A	10.36
Improvement over baseline	17%	N/A	47%

Chapter 2. Development of accurate free surface calculation methods

Chapter 2 describes the activities and accomplishments associated with Task 2 of our Statement of Work. The development of free surface methods is divided into three sections. Section 2.1 describes the development of the two-dimensional method (Hydrofoils). Section 2.2 covers the development of the three-dimensional free surface method to date. Finally, Section 2.3 describes the Interactive Boundary Layer Method developed under a subcontract to the Boeing Company.

2.1 Two-Dimensional Free Surface Method for Hydrofoils

In this section, the development and testing of the two-dimensional free surface method for hydrofoils are discussed. This section of our work has been submitted as a paper and has been accepted for presentation in the Advances in Fluid Mechanics 2002 Conference, to be held 15-17 May 2002, in Ghent, Belgium.

Hydrofoils or ships moving at constant speed in a calm sea will generate a wave pattern. The waves created will dissipate energy and cause resistance to the moving body, which is referred to as “wave drag”. To move near a free surface in a fluid, hydrofoils or ships must overcome the wave drag. While the wave drag is small at relatively low speeds, it increases very quickly with speed and becomes the dominant part of the total resistance. In order to accurately predict the wave resistance and minimize it by modifying the body shape in the design stage of hydrofoils and ships, it is necessary to predict the wave pattern generated by the body.

Theoretical studies on the prediction of wave pattern generated by hydrofoils or ships have been carried out for a long time. However, until recently most studies were based on linearized solutions of the free surface problem. In these linearized solutions, it is assumed that the disturbance to the incoming uniform flow due to the body and the free surface is small in magnitude compared with the uniform flow, and the free surface boundary conditions are imposed on the undisturbed water surface. As a pioneering work, Dawson [15] proposed an efficient linearized method, which gives realistic results, in general, in 1977. However, as the Froude number increases, the nonlinear effects of the free surface become more and more pronounced and the wave resistance predicted by the linearized solutions are not very reliable. These limitations of the linearized methods can be removed and accuracies of the solutions can be improved if the nonlinear effects are taken into account. Therefore, it is desirable to develop a numerical method to solve the fully nonlinear free surface problem.

The solution of the nonlinear free surface problem is much more difficult than the linearized solution. The nonlinear boundary conditions and the presence of the moving boundary, i.e. the free surface, make the numerical problems very complicated and not easily solved. However, with the advances of computational fluid dynamics (CFD), studies have been made recently to solve this nonlinear problem using various numerical schemes [16, 17, 18, 19].

To solve the nonlinear free surface problem, an iterative procedure must be used. It has been found that the iterative procedure tends to be unstable, and severe convergence problems have been experienced by many researchers in their studies. Therefore, techniques such as artificial

Center for the Commercial Deployment of Transportation Technologies

damping and the use of an under-relaxation factor are incorporated into numerical schemes for the suppression of instability.

In the present study, our attention will be confined to the development of a general, robust method to compute free surface flows over submerged two-dimensional bodies using a panel method. However, the solution techniques discussed in this report are not restricted to two-dimensional flow and can be extended to three-dimensional flows in the future.

2.1.1. Mathematical Formulation

Consider a two-dimensional body moving with constant speed in a calm sea. By assuming incompressible, irrotational flow, the mathematical problem reduces to that of solving Laplace's equation for the velocity potential in the fluid domain, subject to a Neumann boundary condition on the body. Besides, both kinematic and dynamic boundary conditions must be imposed on the free surface. The kinematic boundary condition states that fluid cannot penetrate the free surface and the dynamic boundary condition requires the pressure to be constant and equal to atmospheric pressure everywhere on the free surface. The flow is undisturbed far upstream, while a trailing wave pattern is propagated downstream. This means that the waves do not propagate upstream and are referred as the "radiation condition" of the free surface problem.

A coordinate system moving with the body is adopted. The x-axis is horizontal and the y-axis is positive upward with the undisturbed water surface given by $y = 0$ (see Figure 1). The free surface shape is described as a single-valued function of the x-coordinate, i.e., $y = \eta(x)$. The governing equation and boundary conditions can be written as

$$\nabla^2 \phi = 0 \quad (1)$$

$$\nabla \phi \cdot \vec{n} = 0 \quad \text{on the body and free surface} \quad (2)$$

$$p = \text{const} \quad \text{on the free surface} \quad (3)$$

$$\nabla \phi \rightarrow V_\infty \quad \text{as } x \rightarrow -\infty \quad (4)$$

where ϕ is the velocity potential, \vec{n} is the outward unit normal, p is the static pressure and V_∞ is the incoming uniform velocity. Using the Bernoulli equation, equation (3) can be written as

$$g\eta + \frac{V^2}{2} = \frac{V_\infty^2}{2} \quad (5)$$

where g is the gravitational acceleration, and the velocity \vec{V} is given by $\vec{V} = \nabla \phi$. Equation (5) can be reduced to

$$\frac{\eta}{L} = \frac{1}{2} F_r^2 \left(1 - \frac{V^2}{V_\infty^2}\right) \quad (6)$$

Center for the Commercial Deployment of Transportation Technologies

where L is the reference length, usually the chord of the hydrofoil, and the Froude number is defined as $F_r \equiv \frac{V_\infty}{\sqrt{gL}}$. Equation (6) is nonlinear and must be applied to the free surface that is not known *a priori*.

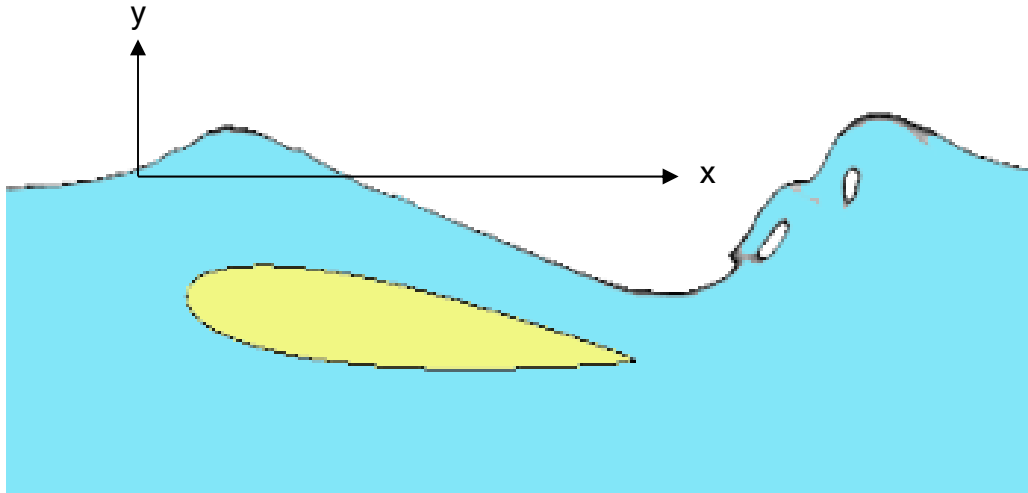


Figure 28. Coordinate system for free surface flow over submerged bodies

Panel methods have been widely used during the past years in aerodynamic and hydrodynamic design and analysis [20]. They can be used to solve potential flows about complicated configurations and give reliable results. Therefore, a panel method was chosen in the present study to solve the two-dimensional free surface flow over a submerged body of arbitrary shape. The body surface and the free surface are divided into panels. Source singularities are distributed along the body surface and the free surface. For lifting bodies, vortex singularities will be used and distributed on the body surface to account for the lift. Boundary conditions are imposed at control points on the body surface and the free surface. Strengths of source and vortex singularities are determined in order to satisfy all the boundary conditions. For lifting bodies, the Kutta condition at the trailing edge of a hydrofoil must also be satisfied. Once the strengths of singularities are determined, the velocity and pressure distributions on the body are also determined.

The free surface problem is difficult to solve for two reasons. First, the dynamic boundary condition on the free surface is nonlinear. In addition to it, the location and the shape of the free surface is unknown. Iterative method must be used in order to solve this nonlinear problem with a moving boundary. The free surface location and shape are updated in successive iterations until the solution converges. Convergence of the iterative procedure is found to be strongly dependent on the way the free surface boundary conditions are formulated and the shape and the location of the free surface are updated. Since the kinematic and dynamic boundary conditions, equations (2) and (6), cannot be satisfied simultaneously with specified location and shape of the free surface, only one condition can be imposed in each iteration. The other condition will be used to update the free surface location and shape between successive iterations. Three different approaches can be adopted in the iteration procedure.

Center for the Commercial Deployment of Transportation Technologies

The first approach is to impose the kinematic boundary condition on the specified free surface, in each iteration, such that the normal velocity on the free surface is zero. An explicit expression for a new wave elevation is then given by the dynamic boundary condition, equation (6), for the next iteration. Although this iterative procedure is obvious, simple, and straightforward, it is well known that it will generate a solution without a trailing wave pattern [19].

The second approach is to impose the dynamic boundary condition on the specified free surface, in each iteration, and use the kinematic boundary condition to update the wave elevation for the next iteration. This approach has been used successfully by Hess [21] to solve the free surface flow over a submerged point vortex. Instead of using source distribution on the free surface, vortex singularities are distributed along the free surface. However, for large wave elevations, convergence could not be obtained.

Since it is the combination of the kinematic and dynamic boundary conditions which determine the wavelike behavior, the iterative procedure must incorporate the interaction between them. Therefore, the third approach is to impose a combination of the kinematic and dynamic boundary conditions on the specified free surface, in each iteration, and use either one of the kinematic and dynamic boundary conditions to update the wave elevation for the next iteration.

To derive the combined boundary condition on the free surface, rewrite equation (2) as

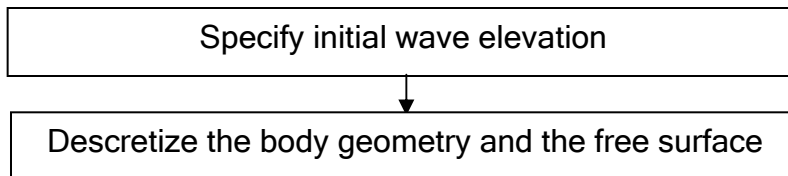
$$\phi_x \eta_x - \phi_y = 0 \quad (7)$$

by noticing that the unit normal vector $\vec{n} = \frac{1}{\sqrt{1+\eta_x^2}}(\eta_x \vec{i} - \vec{j})$. Differentiating equation (6) with respect to x and substituting it into equation (7) gives the combination of the kinematic and dynamic boundary conditions.

$$\frac{(V^2)_x}{2g} \phi_x + \phi_y = 0 \quad (8)$$

where $V^2 = \phi_x^2 + \phi_y^2$.

An iterative procedure based on equation (8) is likely to have better convergence properties. Therefore, the third approach with equation (8) as a combined boundary condition is adopted in our iterative procedure. Since the wave elevation is not known a priori, the free surface shape is assumed to be the undisturbed water surface in the first



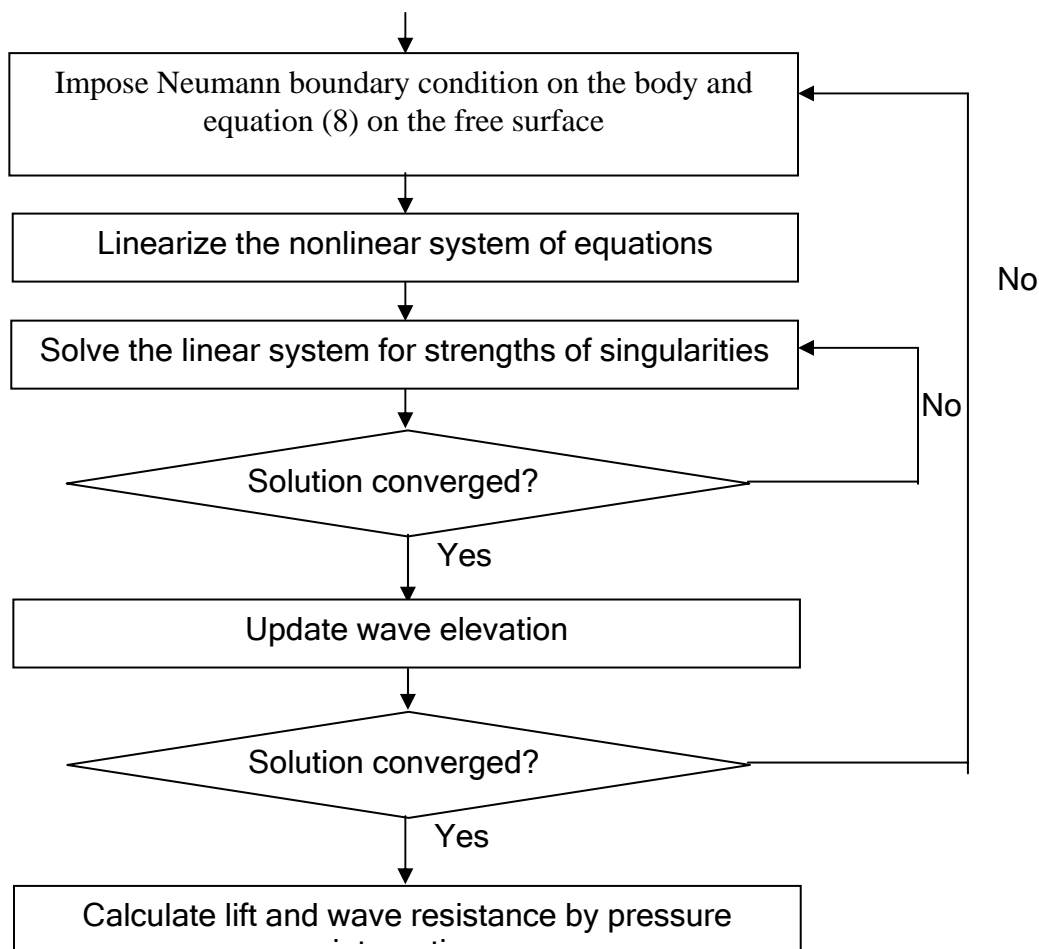


Figure 29. Flow chart of the iterative procedure

iteration. The strengths of the singularities on the two-dimensional body and the free surface are solved by the panel method to satisfy the Neumann boundary condition on the body and equation (8) on the free surface. Since equation (8) is nonlinear, this leads to a set of nonlinear system of equations. The nonlinear system of equations is linearized using Newton's method and a Gauss elimination algorithm is used to solve the linearized system of equations until solutions get converged. Once the strengths of singularities are known, the local velocity on the body and free surface can be calculated. However, the kinematic boundary condition on the free surface is not satisfied yet. Therefore, the wave elevation must be updated in a way such that fluid does not penetrate the free surface. The y coordinate of the free surface panels is allowed to move up and down between successive iterations as a function of the x coordinate. The next iteration starts with the updated location and shape of the free surface. This procedure is repeated until solution gets converged. Figure 2 shows the flow chart of this iterative procedure.

The key to the success of a numerical method in solving the nonlinear free surface problem is the convergence of the iterative procedure since locally introduced errors tend to grow due to inherent instabilities. As the potential flow has no viscosity, the solution of the nonlinear free

Center for the Commercial Deployment of Transportation Technologies

surface problem is non-unique and solutions with upstream waves may be obtained if the radiation condition is not properly imposed. Dawson [15] found that it is possible to enforce the radiation condition indirectly by approximating the derivatives of velocities in the combined free surface boundary condition, equation (8), by upwind finite difference scheme. The use of upwind finite difference scheme adds a dissipative numerical mechanism to the free surface waves and helps the satisfaction of the radiation condition automatically. It is found that the stability of the iterative procedure is quite robust using this numerical technique. Although Dawson [1] adopted a particular four-point finite difference scheme in his linearized method, a three-point upwind finite difference scheme is used to approximate the derivatives of velocities in equation (8) in the present study.

Once convergent solutions are obtained, the velocity and pressure distributions on the body can be found easily with the strength of singularities over the body and free surface be given. The pressure distribution is then integrated to obtain the lift force and wave resistance acting on the body. The non-dimensional wave resistance coefficient is defined as

$$C_w = \frac{F_x}{\frac{1}{2}\rho V_\infty^2 L} \quad (9)$$

where F_x is the force in x direction, i.e. the wave resistance. Alternatively, the wave resistance can be computed from the downstream wave pattern by means of a momentum flux balance.

2.1.2. Numerical Validation

In order to validate the capability of the present method in solving nonlinear free surface problems, a number of test runs have been conducted for which either analytical solutions or experimental data are available. The test cases include a submerged circular cylinder, and two hydrofoils. Comparisons of wave elevations and pressure distributions are made for cases with different Froude numbers and depths of submergence.

2.1.3. Submerged circular cylinder

An analytical solution for free surface flows over a deeply submerged circular cylinder was derived by Lamb [22], with the circular cylinder approximated by a doublet. Assume uniform flow with velocity V_∞ past a submerged cylinder with radius a . If a is small compared with the depth of submergence d measured from the undisturbed water surface to the axis of the circular cylinder, then the equation of the free surface is given by

$$\eta = \begin{cases} \frac{2a^2d}{x^2 + a^2} - \frac{4\pi g a^2}{V_\infty^2} \exp\left(-\frac{gd}{V_\infty^2}\right) \sin\left(\frac{gx}{V_\infty^2}\right) & x \geq 0 \\ \frac{2a^2d}{x^2 + a^2} & x < 0 \end{cases} \quad (10)$$

Center for the Commercial Deployment of Transportation Technologies

Equation (10) indicates that there is a local disturbance upstream of the cylinder for $x < 0$, followed by a train of waves downstream. The wave length is $2\pi V_\infty^2 / g$, which is equal to $2\pi F_r^2 L$. The present method was used to calculate flow past a circular cylinder with the center of the cylinder submerged at a distance of 10 diameters below the free surface. The Froude number based on the depth of submergence ($F_r \equiv \frac{V_\infty}{\sqrt{gd}}$) is 1. Figure 3 compares the wave pattern

calculated by the present method with the analytical solution of Lamb given by equation (10). It is seen that the wave pattern calculated by the present method agrees well with that based on the linear theory except that the wave length calculated by the present method is slightly smaller. This small discrepancy may be due to the nonlinear effect.

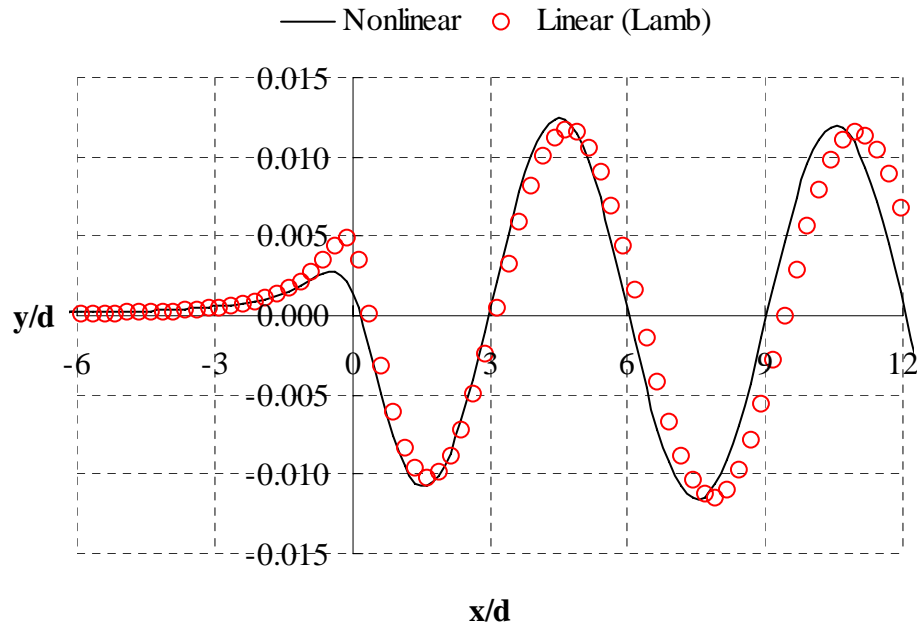


Figure 30. Waves produced by a circular cylinder at $F_r = 1$ with $a/d = 0.05$

Scullen and Tuck [23] calculated the free surface shape for flow past a circular cylinder at different Froude numbers using a nonlinear numerical method. Figure 4 shows a comparison between results obtained using the present method and those given by Scullen and Tuck for a submerged circular cylinder with $a/d = 0.2$. The x and y coordinates are scaled with respect to square of the Froude number. The lines denote results of the present method and the symbols denote results of Scullen and Tuck, respectively. The agreements of both results are excellent. It is also observed that at low Froude number, the free surface is depressed ahead of the circular cylinder but becomes slightly elevated at a high Froude number.

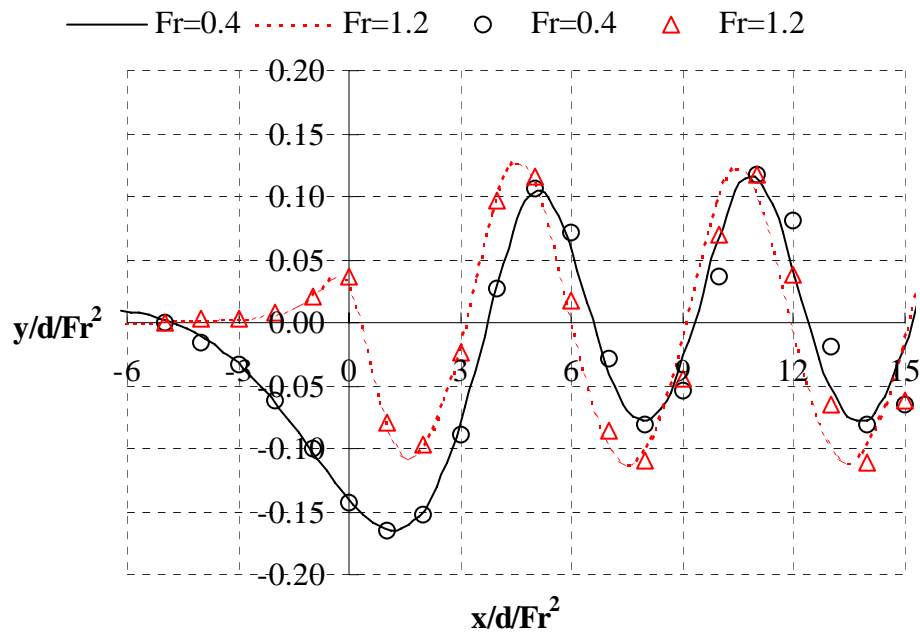


Figure 31. Wave pattern for flow past a circular cylinder with $a/d = 0.2$

2.1.4. Submerged hydrofoils

The numerical method is then applied to two hydrofoils: one with NACA 0012 cross section and the other with NACA 4412 cross-section. Wave pattern and pressure distribution are calculated for various submergence depth at different Froude numbers.

As a first test case for the NACA 0012 hydrofoil, consider flow past the hydrofoil at 4° angle of attack with leading edge depth of submergence equal to the chord length. The Froude number based on the chord is 0.5. Figure 5 shows the wave pattern calculated by the present method. Figure 6 shows the pressure distribution of the NACA 0012 hydrofoil with and without the free surface effects. It also shows the pressure distribution predicted by panel methods using positive images and negative images.

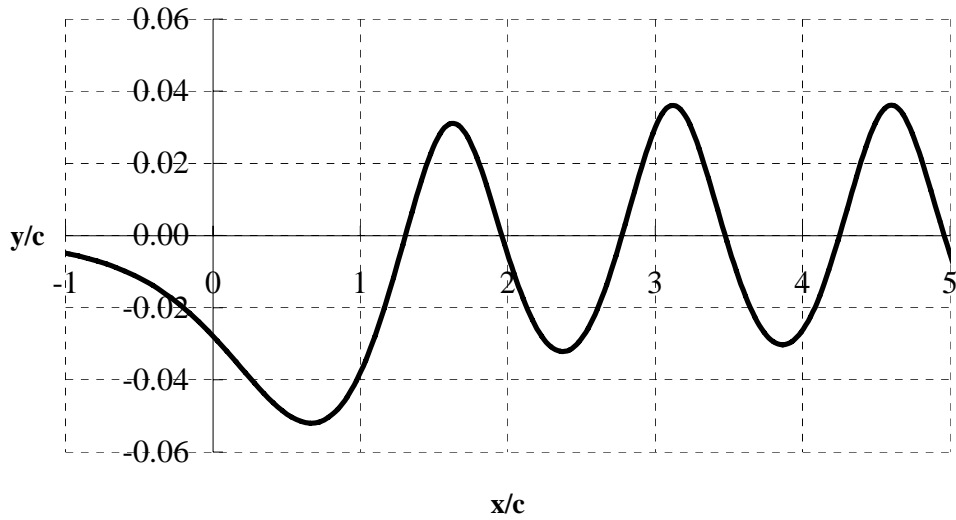


Figure 32. Wave pattern of the NACA 0012 hydrofoil at 4° angle of attack with $F_r = 0.5$, $d/c = 1$

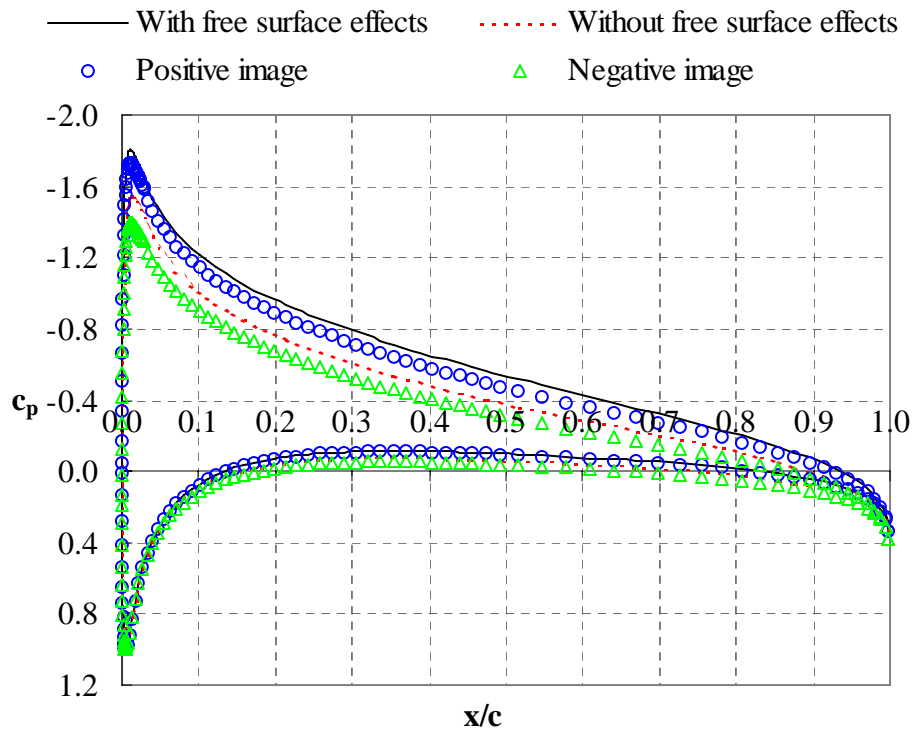


Figure 33. Pressure distribution of the NACA 0012 hydrofoil at 4° angle of attack

The negative image method satisfies Laplace’s equation with the dynamic boundary condition imposed on the undisturbed water surface. In both method of images, the undisturbed water surface acts like a mirror plane. The flow around the hydrofoil is formed by reflecting the

Center for the Commercial Deployment of Transportation Technologies

hydrofoil about the mirror plane to generate either positive or negative images. At low Froude number, solution of the positive image method well approximates the real flow. It is found from Figure 6 that the pressure distribution predicted by the positive image method is closest to that calculated by the present method. This is what as expected since the Froude number is low ($=0.5$). Figure 6 also shows that the pressure peak on the upper surface is increased due to the free surface effects, which indicates an increase in the lift for this test case.

The wave pattern of a NACA 0012 hydrofoil at 5° angle of attack was measured by Duncan [24] in a towing tank. The Froude number is 0.567 with mid-chord depth of submergence varying from 1.286 times chord to 0.783 times chord. It is found that wave breaking takes place when the depth of submergence is 0.951 times the chord length or less. Numerical results obtained by the present method are compared with the experimental data of Duncan and shown in Figures 7 to 9. It is seen that the wave amplitude becomes larger and the wave length becomes smaller as the depth of submergence decreases. These nonlinear behaviors are accurately captured by the present method and the wave pattern calculated by the present method agrees well with that measured by Duncan in general. However, as the depth of submergence decreases to 1.034 times the chord length, the discrepancy between them increases. When the depth of submergence is reduced further to 0.951 times the chord length, the present method fails to converge. Since wave breaking takes place when the depth of submergence 0.951 times chord length or less, it is questionable that if flow under these conditions can be modeled by the present method,

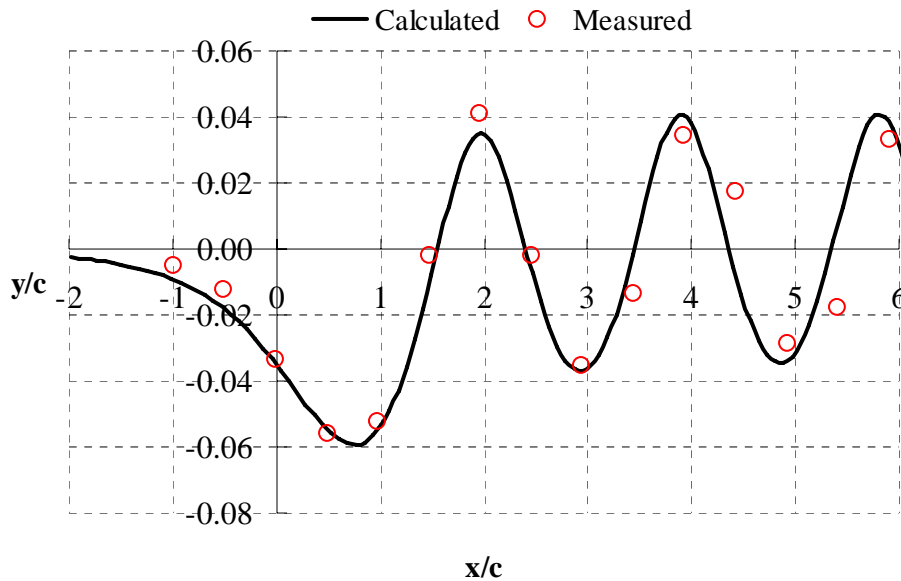


Figure 34. Wave pattern of the NACA 0012 hydrofoil at 5° angle of attack with $F_r = 0.567$, $d/c = 1.286$

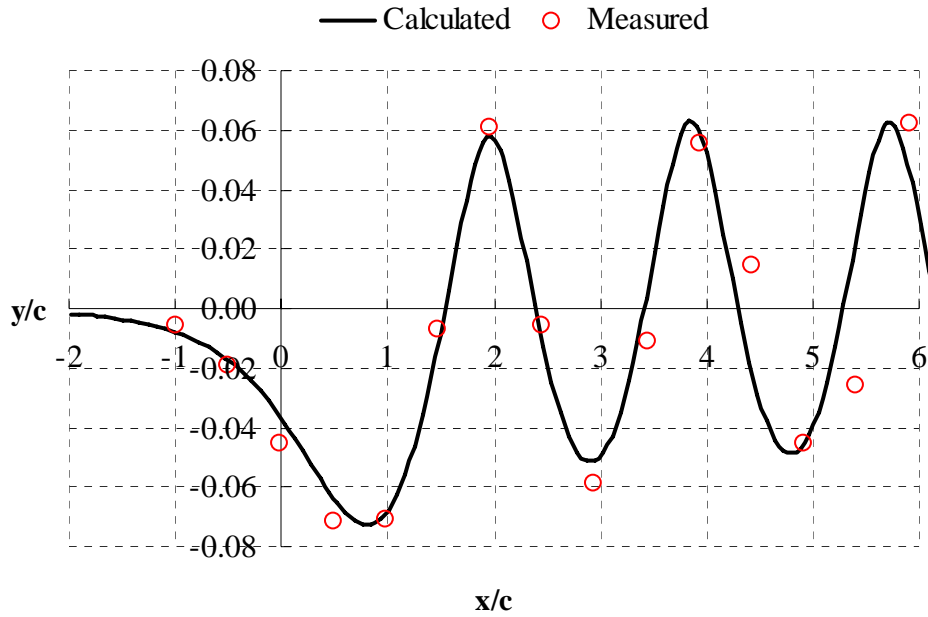


Figure 35. Wave pattern of the NACA 0012 hydrofoil at 5° angle of attack with $F_r = 0.567$, $d/c = 1.162$

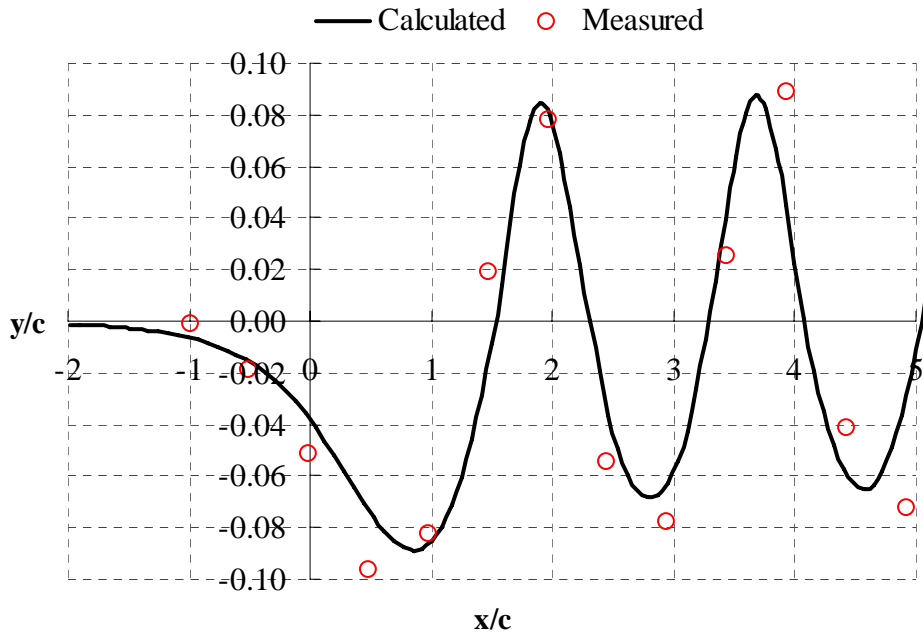


Figure 36. Wave pattern of the NACA 0012 hydrofoil at 5° angle of attack with $F_r = 0.567$, $d/c = 1.034$

Center for the Commercial Deployment of Transportation Technologies

which assumes steady potential flow. Whether the difficulty to obtain convergent solutions for these cases is due to the nonexistence of the steady potential flow solution or due to numerical instabilities is still not clear.

Pressure distribution for NACA 0012 hydrofoil at 5° angle of attack was calculated by Hino, Martinelli and Jameson [25] when the depth of submergence equals to 1.034 times the chord length. They solved the incompressible Euler equations using a finite volume method with unstructured grid. Figure 10 shows the pressure distribution predicted by the present method agrees excellently with that given by Hino, Martinelli and Jameson. However, the pressure peak at the leading edge calculated by the panel method is lower than that by the Euler method.

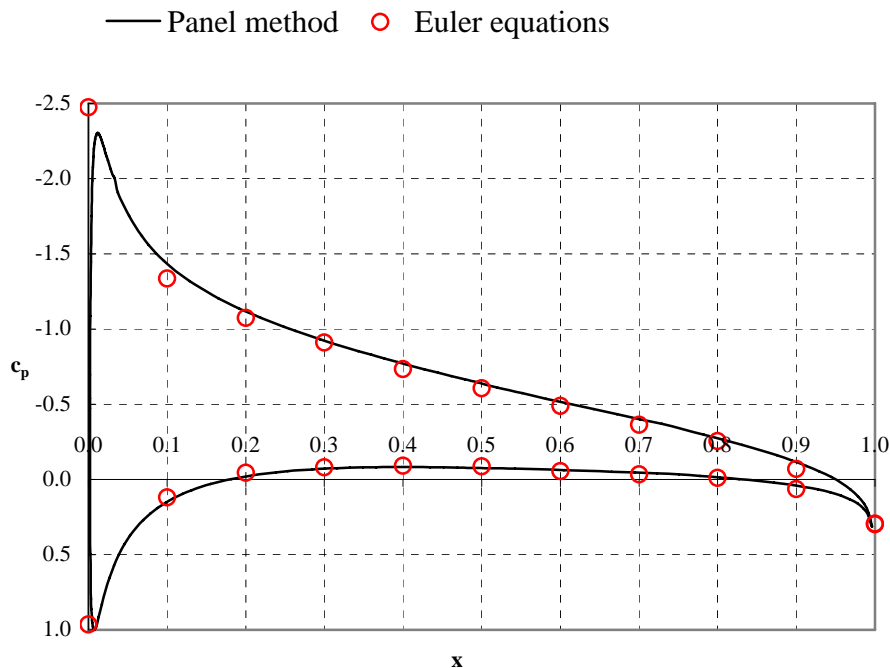


Figure 37. Pressure distribution of the NACA 0012 hydrofoil at 5° angle of attack with $F_r = 0.567$, $d/c = 1.034$

Experiments of a NACA 4412 hydrofoil were carried out by Ausman [26] in a water channel. Figure 11 shows a comparison of the pressure distribution at 4.7° angle of attack calculated by the present method and measured by Ausman. The Froude number is 1.035 and the leading edge depth of submergence is 1.3 times chord length. It is seen that the agreement is remarkable except near the trailing edge. Figure 12 shows the pressure distribution at 2.3° angle of attack when the Froude number is 0.962 and the leading edge depth of submergence is 0.288 times the chord length. The calculated results under-predicts the pressure peak on the upper surface near the leading edge. Since the finite depth of the water channel (equals to 2.5 times the chord length for this case) is not modeled in the present method, it may cause the discrepancy in results for this case.

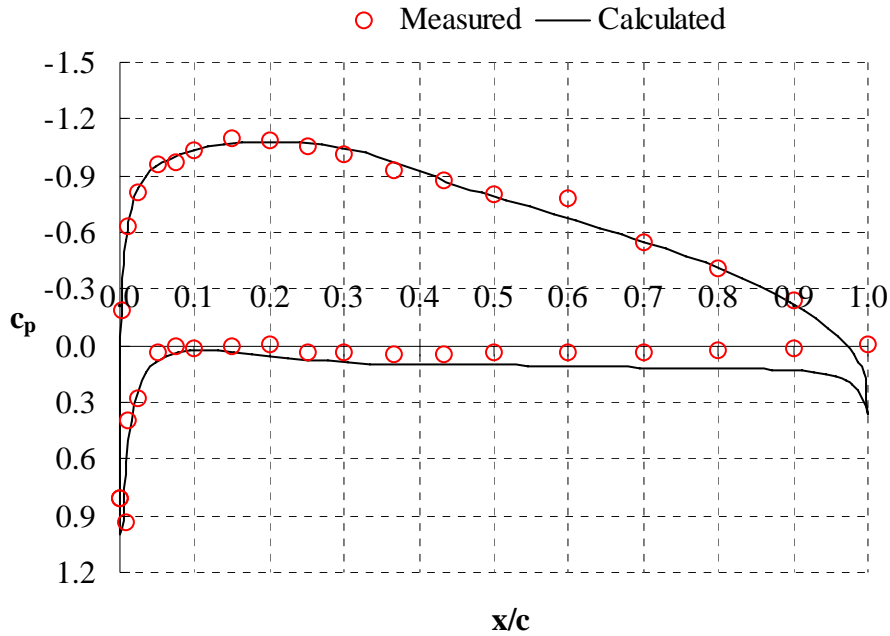


Figure 38. Pressure distribution of the NACA 4412 hydrofoil at 4.7° angle of attack with $F_r = 1.035$, $d/c = 1.3$

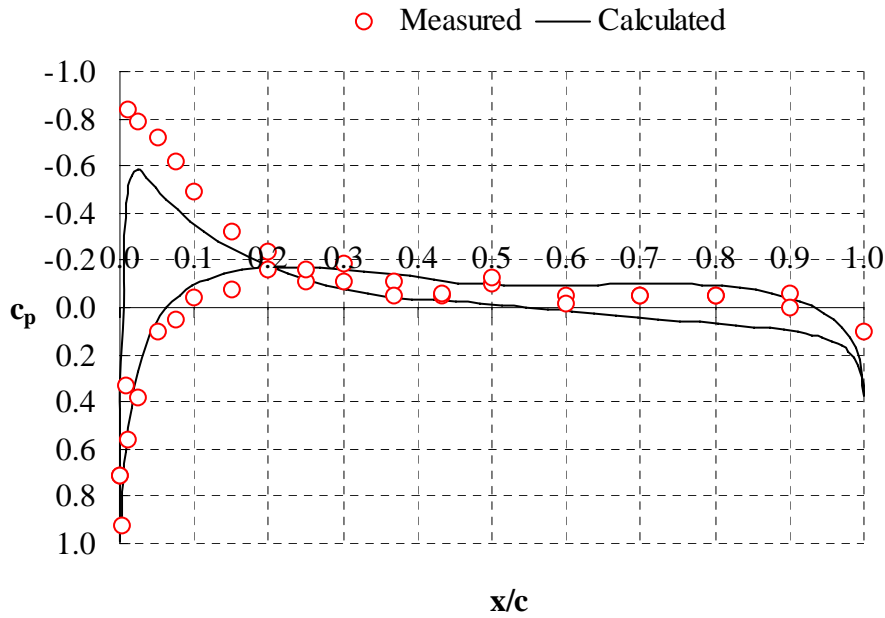


Figure 39. Pressure distribution of the NACA 4412 hydrofoil at 2.3° angle of attack with $F_r = 0.962$, $d/c = 0.288$

Center for the Commercial Deployment of Transportation Technologies**2.2 Three-Dimensional Free Surface Code Development and Improvement for High Speed Ships**

As mentioned earlier, the extension of the 2-D Free Surface method to three dimensions is very extensive, both in terms of mathematical formulation as well as in algorithm development and implementation. This task was initiated in the FY 00 program, and will be finalized in the FY 01 program. Prior to the present work, CSULB had already developed the foundation for a free surface code. However, it was in an early stage of development and far from complete. This existing code was used as the basis for the development of this new free surface code (hereafter referred to as the wave code). Like the 2-D method of section 2.1, our free surface method is distinguished from other existing methods by the implementation of a fully non-linear free surface boundary condition applied on the moving boundary, rather than an otherwise approximated boundary condition. This requirement represents new challenges, primarily due to the fact that the location of the free surface boundary is unknown *a priori*. In the following sections, we will first describe improvements to, and development of the code, to date, as well as what remains to be done in the next phase of the program. We will then present some results for both fully submerged as well as water piercing configurations.

The development of the method is described here in the context of the design of a hull/body/lifting surface configuration for application to the design of a fast ship, as described in Chapter 1. The particular design considered here is Pacific Marine's innovative "Twin H" configuration, illustrated in Figure 1, and a fully submerged configuration referred to as the "Midfoil" configuration, shown in Figure 8. However, the method is general and can be easily applied to other configurations. In the Twin H configuration, a horizontal strut connects two bulbous lifting bodies. These bodies are in turn connected to the lower hull surface by two vertical struts. The required lift for the ship is provided both by the buoyant lift due to the displacement volume of the submerged bodies, as well as by the dynamic lift developed by the lifting surfaces. The vertical struts, if not properly designed, will develop a side force that will also result in induced drag. The optimization of such a configuration for minimum drag will therefore require that the correct balance be achieved between the dynamic lift, and its associated induced drag, against the buoyant lift due to the submerged volume of the bodies. This submerged volume will result in the development of both viscous drag due to skin friction, as well as wave drag due to the development of surface waves, which will propagate away from the configuration. In order to perform this design optimization, the Wave Code is applied to compute the lift and drag associated with the motion of this body through water in the presence of the free surface. This code must therefore compute the normal lift and drag forces associated with aerodynamic and hydrodynamic problems, in addition to the computation of the wave drag developed by the body. A crucial part of this wave drag computation is the computation of an accurate modeling of the shape of the free surface waves in the presence of the translating body. The approach applied here will use the Wave Code to compute the surface shape, combined with a separate flow calculation to compute both the viscous and induced drag associated with the configuration.

For both of these computations, a general three-dimensional panel method is applied. The Wave Code is an iterative procedure based on the well-known Surface Singularity technique. At each

Center for the Commercial Deployment of Transportation Technologies

iteration, the free surface shape is assumed to be known and the singularity strength is adjusted to satisfy the constant-pressure boundary condition on the free surface as well as the standard normal-velocity boundary conditions on the submerged body. The free surface is then altered to obtain zero normal velocity on the sea surface.

As with every CFD code, this code has its own special requirements to obtain the best results. Our main effort is to obtain the best results in the most efficient way. During this process, we encountered the following issues, which will be described later in this report:

1. Use of extra strips to tie the lifting sections of the geometry.
2. Use of symmetry in order to reduce the running time and the memory requirement.
3. The size and mesh density of the free surface.
4. The modeling of Strut/Free-surface intersection.

In a classical Panel Method code, the incompressible flow about a body can be represented by a distribution of singularities on the surface of the body. The flow external to the body, induced by such a singularity distribution, will satisfy Laplace's equation for incompressible, irrotational flow. The flow problem can therefore be reduced to a boundary-integral problem in which the singularity distribution required to satisfy the boundary conditions is computed. In the method applied here, source singularity panels distributed on the surface of the body satisfy the normal velocity boundary condition. For a lifting body, a Kutta condition applied at the trailing edge requires that the pressure on the upper and lower surfaces must match. This requires the introduction of an additional singularity distribution. In the case of the Wave Code applied here, the additional singularity distribution is provided by a dipole distribution around each lifting strip. The global strength of this dipole distribution is adjusted to satisfy the Kutta condition. In addition to the bound vorticity on the surface resulting from this dipole distribution, a trailing vortex wake is introduced which extends infinitely far downstream. In general, a single wake panel is used for each lifting strip, with the computed velocity influences being based on those due to a semi-infinite panel, although for the surface piercing Twin H configuration, the near field wake is also paneled with the semi-infinite wake applied some distance downstream from the body. For the Wave Code, dipole panels are also introduced on the free surface of the water. The strengths of these singularities are computed from the requirement for the pressure to be constant along the free surface. Since the shape of the free surface is not known ahead of time, a surface shape is assumed, and the flow field resulting from this singularity distribution will not, in general, satisfy a "zero-normal" velocity condition on the free surface. The computed normal velocity resulting is therefore used in an iterative fashion to update the free surface shape, and to compute a new velocity field resulting from the application of a "constant pressure" condition on this modified free-surface shape. The resulting iterative procedure forms the basis of our Wave Code.

2.2.1 Use of Extra Strips

In the application of surface panel methods to aerodynamic and hydrodynamic lifting-body problems, the use of “Extra Strips” to provide the carry-over of lift from a wing or fin through a non-lifting fuselage or hull has been found to greatly reduce the panel density required for a reasonable level of accuracy. An “extra strip” is an internal set of panels whose singularity distribution is linked to that of the adjacent external panels. For a wing/fuselage configuration, the extra strip will carry the lift of the wing surface into the centerline of the fuselage from the wing/body intersection. While not mathematically required to satisfy the surface boundary conditions, in the absence of an internal extra strip, the fuselage surface panel density required to satisfy the surface boundary conditions becomes unacceptably large. The presence of the internal singularity distribution greatly reduces the panel density required on the nonlifting body. In addition, for configurations with multiple intersecting lifting surfaces, it has been found that the fidelity of the solutions can be greatly enhanced through the use of extra strips, which provide an internal carry-over for the circulation from one lifting surface to another. The presence of such extra strips has been found to provide an improved modeling of the continuity of circulation, which will occur physically between two intersecting lifting surfaces.

In order to develop the most appropriate panel distribution for application to the Twin H lifting body configuration, solutions were computed in the Wave Code, both with and without extra strips. For this configuration, internal extra strips are used to connect the horizontal strut with the lifting bodies, as well as to connect the lifting bodies to the vertical support struts. Figure 40 compares the results of the computed dipole strengths on the horizontal lifting surfaces. For this configuration, the dipole strength is directly proportional to the circulation about a given lifting section on the body. The dipole strengths are plotted for two computations. The first is for the case in which no extra strips are included, while the second includes extra strips as outlined above. The case without extra strips has very low circulation on the lifting bodies with no lift carry-over from the horizontal strut. Unrealistic discontinuity in circulation from one lifting section to another was observed. This Figure also shows the computed dipole strength that is obtained when extra strips are included in the model. In this case, a physically realistic carry-over of the lift from one component to the next is observed. In this Figure, a jump in the dipole strength along the center of the lifting body can be seen. This jump results from the circulation that is carried on the vertical strut. Figure 41 plots the dipole distribution on the vertical strut from which we can see that the dipole strength at the lower end of the strut does indeed match the jump, which was observed on the horizontal lifting body.

Furthermore, our studies show that extra strips must have a small but finite width; otherwise the code would fail to converge. This is simply due to the breakdown of the mathematical formulae that are used to compute the influences of the surface singularities as the panel width approaches zero. A special procedure has been developed for generating extra strips with finite width to tie the lifting components of the geometry. The width of these extra strips is sufficiently small that

Center for the Commercial Deployment of Transportation Technologies

there is no effect on the integrated forces and moments, but large enough to avoid the numerical problems described above. Some exploratory runs were performed to define the appropriate extra strip width.

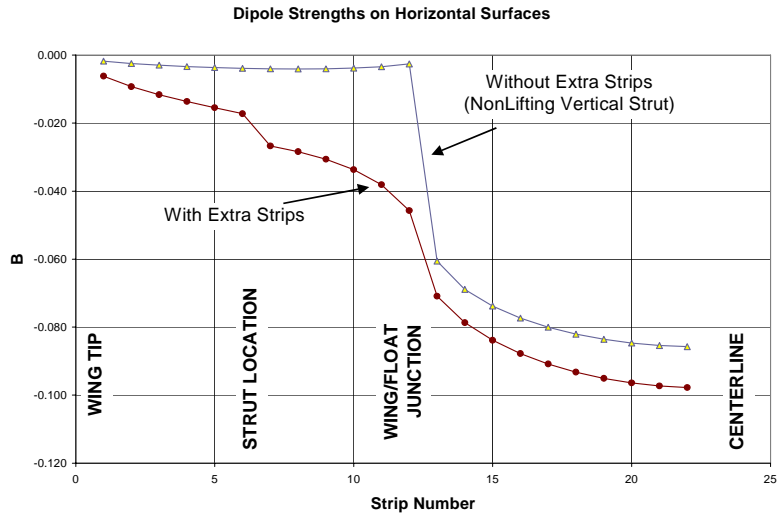


Figure 40. Computed Dipole Distribution on Horizontal Lifting Surfaces

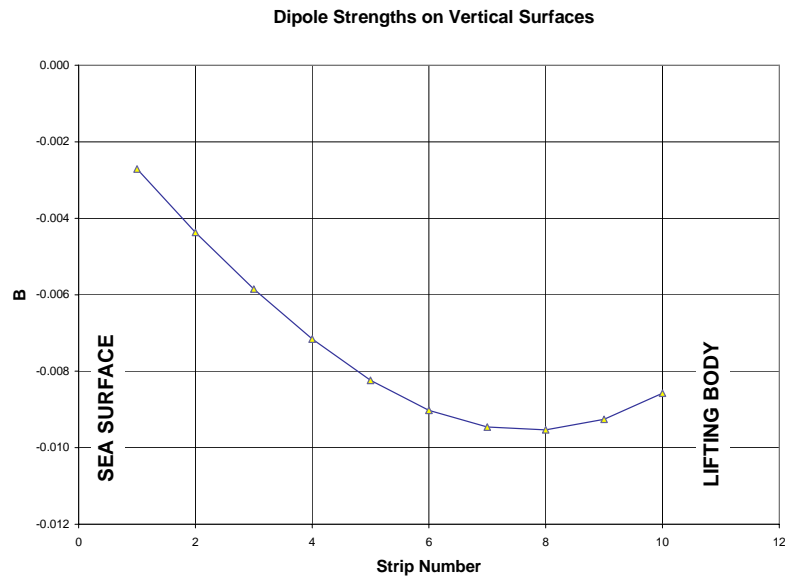


Figure 41. Computed Dipole Distribution on Vertical Strut

Center for the Commercial Deployment of Transportation Technologies

2.2.2. Symmetry option

The present code requires running time and memory that tax our resources to the limit. Computer running time in excess of 8 hours is not unusual, and the memory requirement is 4gb. A symmetry option, in which only half of the geometry is modeled, while the influence of the image is included mathematically, must therefore be used in order to reduce both running time and memory requirement. Modifications were made to the code to apply symmetry to the Y-coordinates and the velocities, and to include the free-surface influences.

The Twin H geometry was run, with and without symmetry, for one iteration. Identical results were obtained between the full geometrical model and the half model with the symmetry option. The running time for the full geometry, on a SGI origin 3200 computer, is 125 minutes approximately, while only 22 minutes was required for the half geometry with the symmetry option. In order to further reduce the CPU time and memory requirements, additional restructuring of the algorithm is planned for the future phases of the work. A C⁺⁺ version, with the proper parallelization of the code, will also substantially reduce the computer resources required and will make this code a much more versatile design tool.

2.2.3. Free Surface Mesh Sensitivity Study

The size of the free surface and the mesh density is expected to have some effects on the results. The optimum mesh is one that will result in the best solution within a reasonable running time. For high-speed (high Froude Number) applications, the sea surface size is particularly important since the surface wavelength is relatively long, thus requiring a large sea surface to adequately capture the wave. A large sea surface, however, substantially increases the CPU time and memory requirements. In order to determine the optimum mesh, that is, the optimum free surface size and the optimum number of panels, we need to study the effect of the mesh on the running time and on the shape of the free surface and the pressure distribution on the body.

To study the effect of the number of panels on the running time, another Pacific Marine lifting body referred to as the “Midfoil” geometry was used and 3 test cases were run. The midfoil geometry of Figure 8 was run as a fully submerged case (struts were removed). The sea surface sizes and panel densities are summarized in Table 9 below.

Figure number	X range (meters)	Y range (meters)	DX * DY	Number of Panels
41	6.1 to -106.7	0 to 38.1	2.26 * 2.24	51 x 18
42	6.1 to -106.7	0 to 38.1	1.13 * 1.12	101 x 35
43	6.1 to 213.4	0 to 76.2	2.26 * 2.24	98 x 35

Table 9 : Mesh Sensitivity Test Case Parameters

Center for the Commercial Deployment of Transportation Technologies

The theoretical wavelength for this condition is estimated to be 63.1 meters, thus a minimum sea size of 100 m was selected. The submerged body is located at $x = 0$ to $x = -8.8$ m. Figures 42, 43, and 44 show the qualitative shape of the sea surface height. Figure 44 shows the shape of the sea surface at the center line. This figure indicates that the sea surface shape is not sensitive to the sea surface size (as long as it is sufficiently large). However, adequate mesh density is needed to capture the wave shape accurately.

Similar mesh sensitivity studies were conducted for the Twin H configuration. Based on these initial studies, the appropriate mesh density and sea surface size were chosen for various results in this report. More comprehensive panel sensitivity studies are going to be conducted in the next phase of the program.

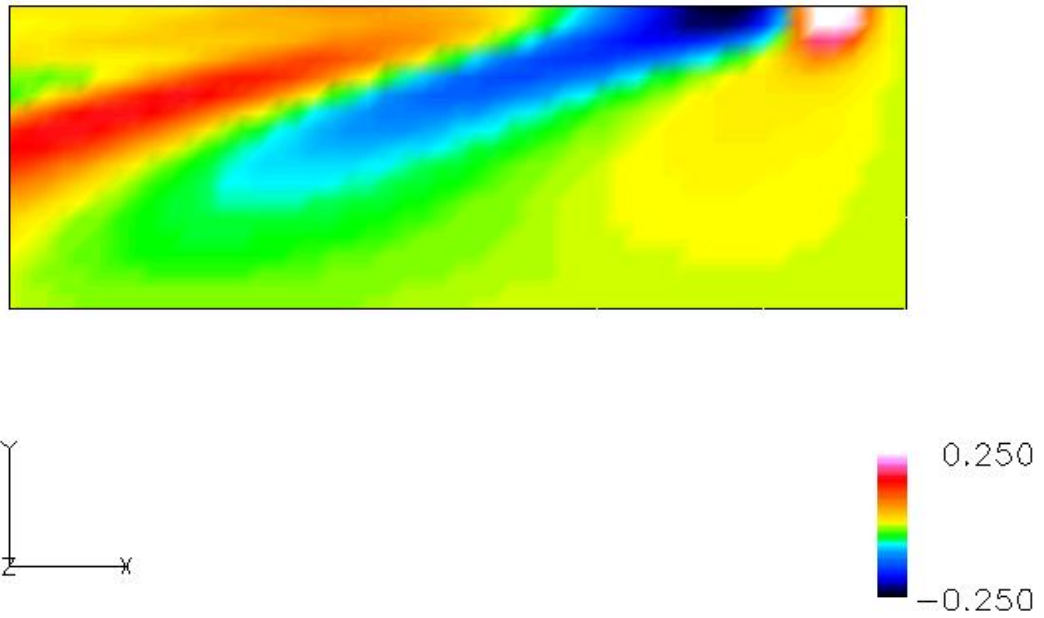


Figure 42. Wave Height Z in meters

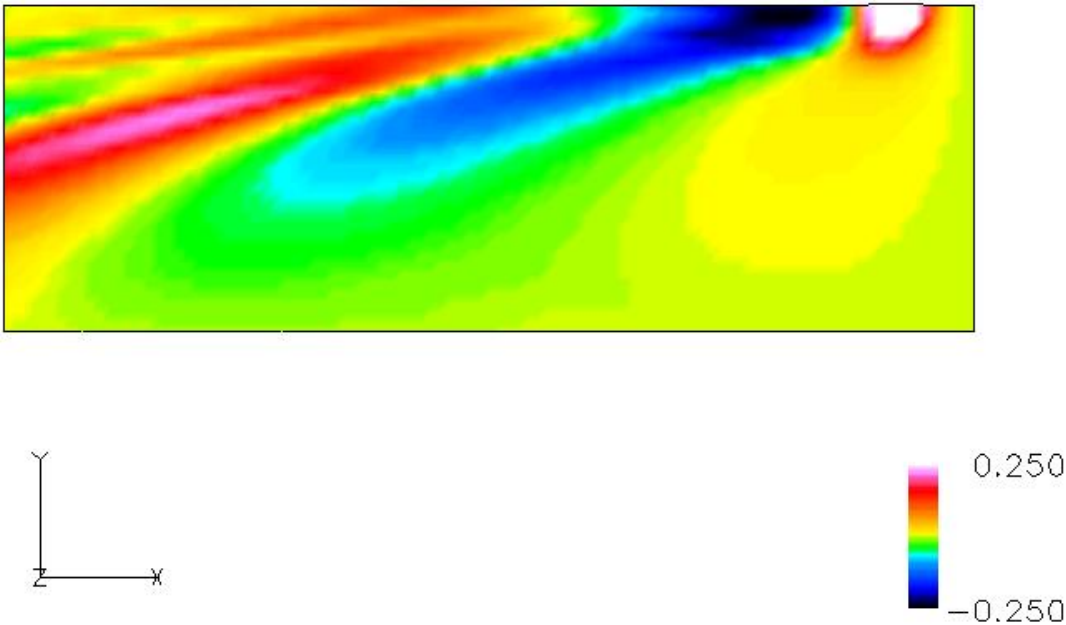


Figure 43: Wave Height Z in meters

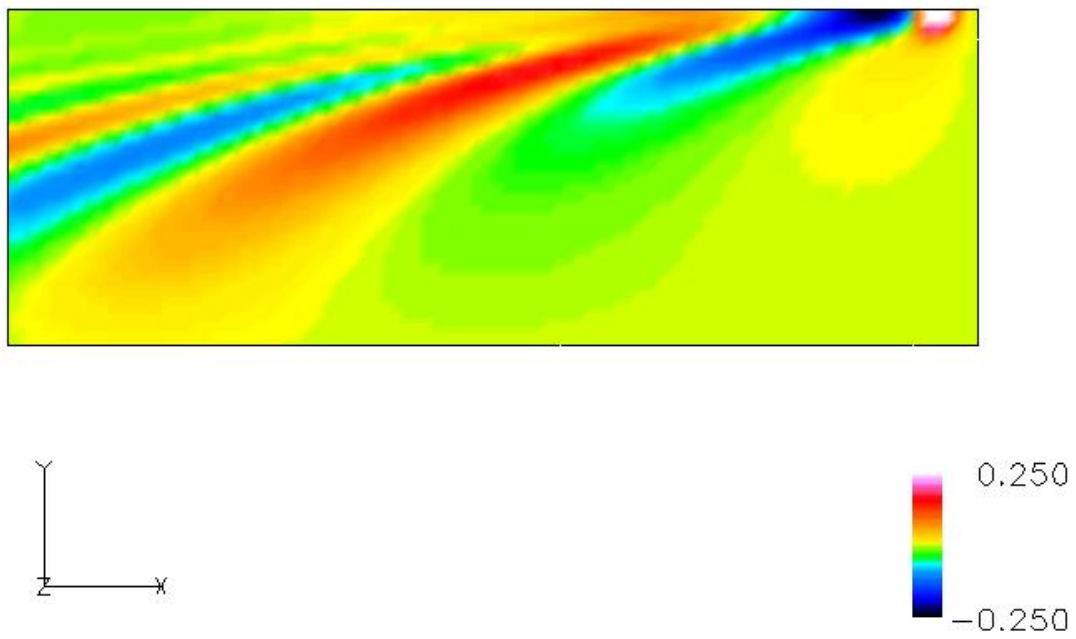


Figure 44. Wave Height Z in meters

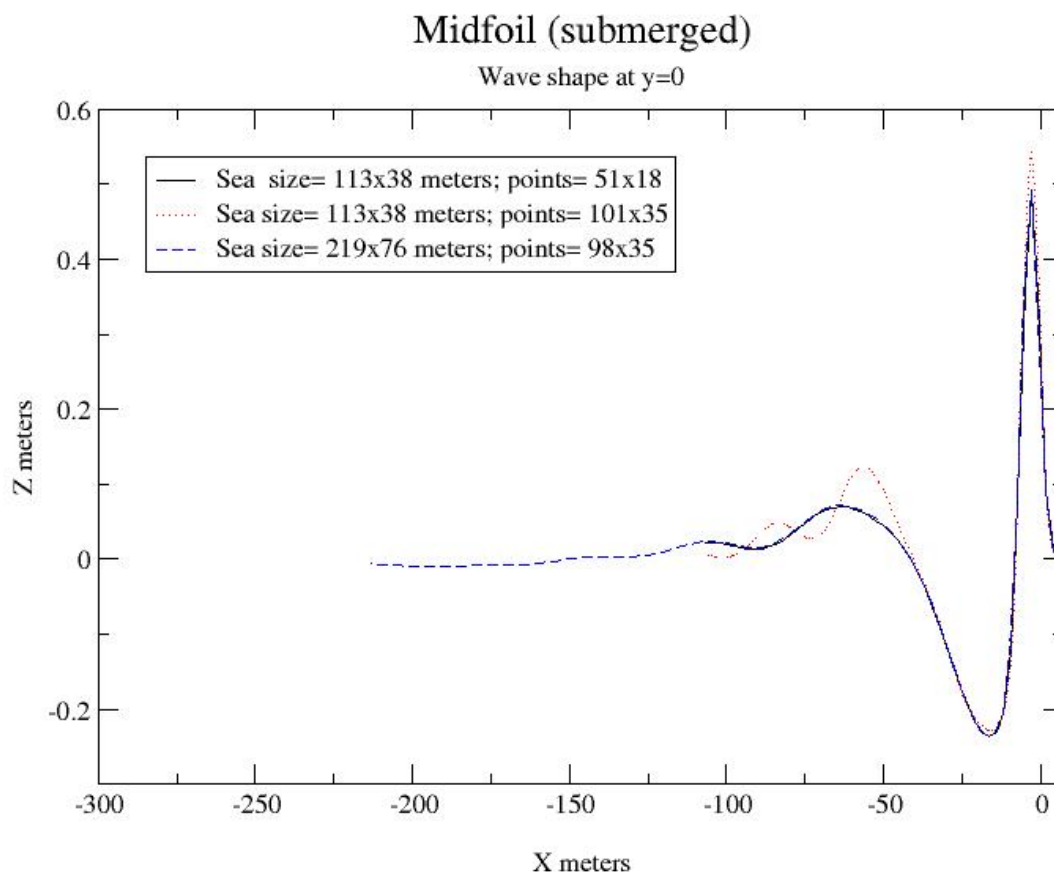


Figure 45. Midfoil (submerged) Wave Shape at $y=0$

2.2.4 Modeling of Strut/Free surface Intersection

At the intersection of the lifting strut with the free surface, physical continuity implies that the circulation about the vertical strut must decrease to zero. Therefore, it is not thought that an extra strip will be required on the vertical strut. However, in practice, the circulation on the tip strip on the strut will not be identically zero, and so there will be a non-zero strength wake singularity, which extends downstream along the free surface. The initial panel distribution on the vertical strut is designed to align with the free surface that is initially at constant height. As the free-surface calculation proceeds, the free surface shape changes. The panel distribution will also have to be changed. This will be accomplished through the use of a CAD geometrical model that has been developed (as part of the optimization process) for use with the Pro-E software package. In this way, an automatic procedure can be used to maintain continuity between strut panel distribution and the sea surface. It should be noted that the continuity in sea surface and body panels must also be continued into the near wake definition, so that the trailing wake panels from the upper edge of the strut maintain continuity with the sea surface. The correct modeling of the wake of the strut and the sea surface is currently under further investigation.

Center for the Commercial Deployment of Transportation Technologies

2.2.5 Fully submerged configuration: Submerged Midfoil

To test the development of the wave code up to now, Pacific Marine's Midfoil geometry was chosen as the first test case. This geometry is shown in Figure 8. Pacific Marine has tested this geometry and provided us with their experimental pressure data for validation. Figure 45 shows the comparison between measured pressure distribution and calculated results using IBL-Neg and our Wave Code (referred to as Dacvine). At this stage of the wave code development, in order to compute the viscous drag, in addition to other aerodynamic and hydrodynamic quantities, the wave shape computed by the wave code is imported to our IBL panel code. The disturbed sea surface shape is treated as a solid wall and the flow is then calculated. Results shown here have been obtained through this process. It can be seen from the figure that our IBL-Neg image and Wave Code results are consistent and fairly close to the experimental results. Further validation of the wave code is currently underway and will be completed in the next phase of the program. Data obtained from the planned at-sea trials (FY 01) from Pacific Marine will provide an excellent basis for validation of CFD results.

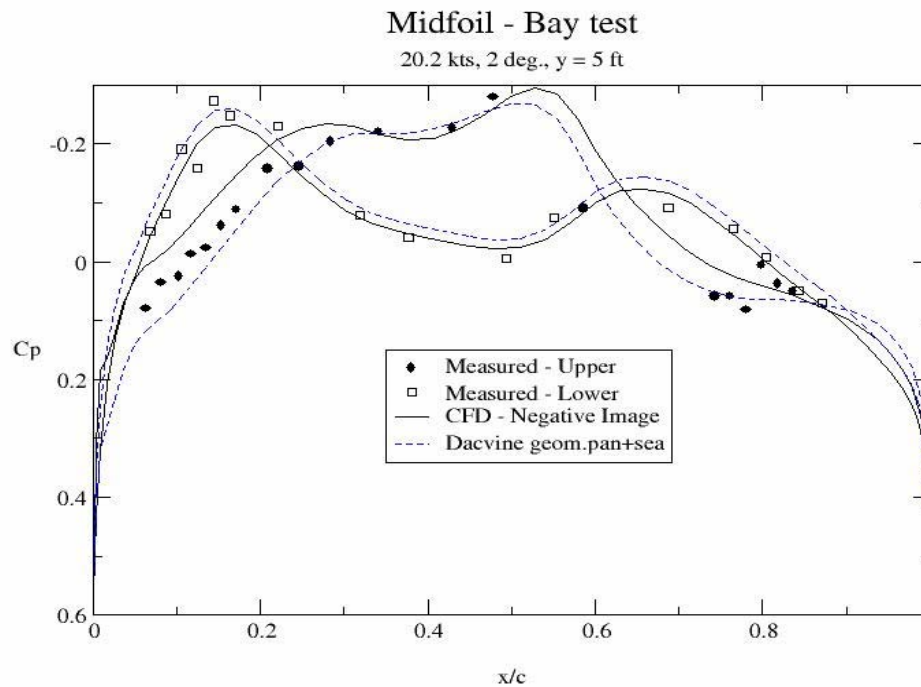


Figure 46. Comparison of the experimental and CFD pressure data

Center for the Commercial Deployment of Transportation Technologies

Figure 47 shows the sea surface (wave) height for this case and indicates that all of the main features of the sea surface shape are well described.

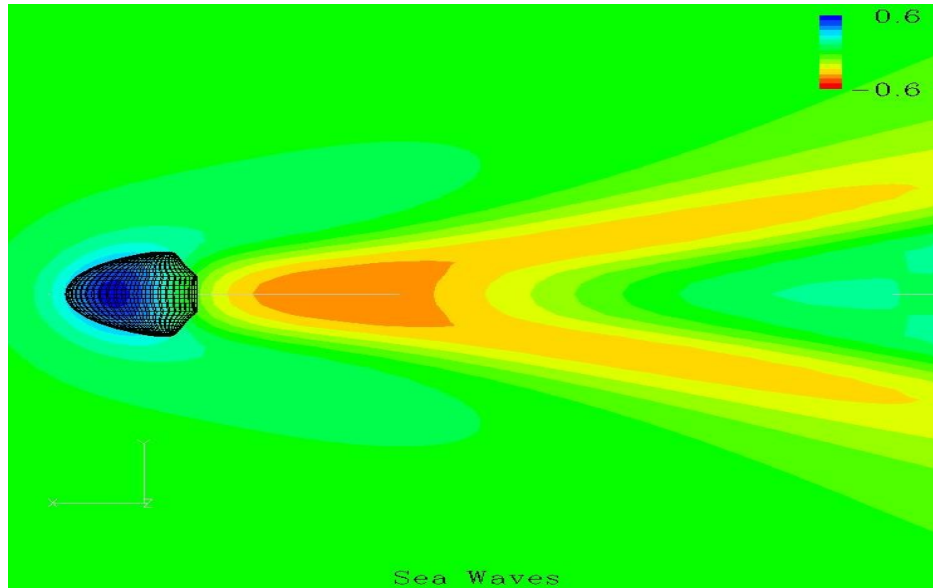


Figure 47. Sea surface height for Midfoil geometry

2.2.6. *Twin H Configuration*

The existence of a water-piercing (lift generating) strut in the TwinH geometry makes the computations more difficult, as previously described. Furthermore, the movement of the sea surface around the water-piercing object is also more complicated. After each iteration, a new sea surface shape is computed. This new sea surface is modeled with Nurb surfaces in the ProE CAD program. The ProE CAD program then determines the intersection of the sea surface and the water-piercing strut. The new “trimmed” surface is then re-paneled and used for the next iteration of the sea surface. A number of studies were conducted to improve the efficiency and accuracy of this process. While the Wave Code is currently stable and produces very reasonable results, further improvements are planned, which will be carried out in the next phase of the program. The most significant of these improvements to the code will be the implementation of a new algorithm to improve the moving of the sea surface elements, consistent with the three-dimensional wave shape. This will significantly enhance the accuracy (zero normal velocity boundary condition) as well as the CPU time requirements.

Various solutions for the TwinH geometry are presented in Chapter 1 (for example, Figures 25 and 26), and therefore are not repeated here. They are also compared with IBL-Neg image and USAERO results and discussed invalidation of the optimum section. We only present the computed sea surface shape for this case in Figure 48 to show that details of the wave pattern are well predicted.

Center for the Commercial Deployment of Transportation Technologies

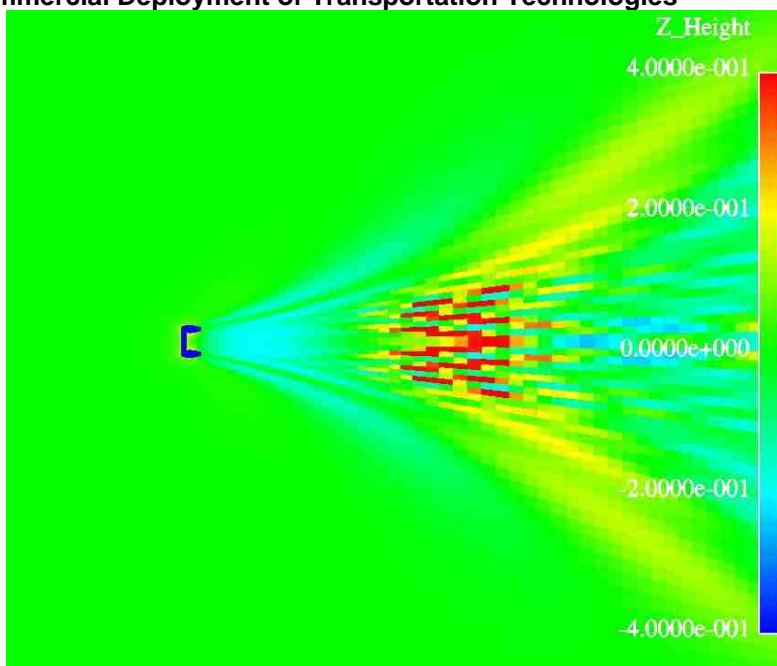


Figure 48. Sea surface shape to Twin H body

2.2.7. Remaining Work

At the end of this phase of the program we have developed a three-dimensional free surface code, which is stable and produces reasonably accurate results. The completion of this method, with many needed improvements, as well as complete validations of the results, will be the subject of future work (FY 01). Particularly, when Pacific Marine's at-sea trials are completed, the data will be used to test and validate the method.

The formulation and coding are essentially complete. There are, however, a few modifications that are necessary to reduce the currently excessive computational requirements and improve the robustness of the method. The primary improvement needed is a more elaborate algorithm for moving the sea surface panels. The current "strip" method results in slow convergence and on some occasions in slight inaccuracies in implementation of the zero normal velocity. During the next phase we will work to improve this feature.

2.3 Interactive Boundary Layer with Free Surface

As mentioned earlier, the wave code currently under development is based on full potential (inviscid) flow theory. At this phase of the program, viscous drag is calculated by first computing the free surface shape with this (inviscid) wave code. This free surface shape is then modeled as a solid wall in our standard Interactive Boundary Layer (IBL) panel code, where viscous flow and viscous drag are computed.

Center for the Commercial Deployment of Transportation Technologies

It is the eventual goal of the authors to implement an IBL method directly into the wave code. The initiation of this task was subcontracted to the Boeing Company. Their work is described in a separate report, which is included here as Appendix I. The outcome of the Boeing study will be used in the future phases of Free Surface Code development.

SUMMARY/CONCLUSION

The overall outcome of this project has been the development of a novel design and optimization method, its application to fast ships and the development of new CFD methods to calculate flow over submerged and water-piercing bodies with free surface effects.

The design and optimization method developed (Chapter 1) links a CAD program for shape representation, a grid generation program for paneling surfaces, a CFD program for calculation of the flow, and a numerical optimization program. In this approach, the baseline geometry is *parametrically* modeled in CAD, passed on to the mesh generating program, the mesh is then passed on to the CFD program to solve the flow field and determine the objective function, such as Lift to Drag (L/D) ratio. Using a Genetic Algorithm, the optimizer then changes the parameters to find the optimum subject to define constraints.

This method was applied to Pacific Marine's Twin-H lifting body. The result was a new configuration with a 17% increase in L/D relative to the base geometry at a speed of 40 knots.

In the second part of the work (Chapter 2), new CFD methods for free surface flows were developed.

In the two-dimensional study, a general method has been developed to calculate flows over submerged two-dimensional bodies. The fully nonlinear effects of the free surface are taken into account. The wave pattern and pressure distribution on the surface of two-dimensional bodies are calculated for different Froude numbers and depths of submergence. Results are compared with either analytical solutions or measurements from experiments. It is concluded that

- (1) The results of the present method showed good agreement with analytical solutions and measurements in general. It demonstrates that the present method is capable of calculating two-dimensional nonlinear free surface flows accurately.
- (2) The adoption of upwind finite difference scheme suppresses numerical instability and enables the iterative procedure to be stable.
- (3) As the Froude number increases and the depth of submergence decreases, the augmented nonlinear effects tend to increase the wave amplitude and reduce the wave length.
- (4) For large disturbances, the physical solution is expected to produce a breaking wave. When the breaking wave takes place, it is difficult to obtain a converged numerical solution. Whether this is due to the nonexistence of a steady potential flow solution or due to numerical instability needs to be clarified.

A general method to calculate the 3-D flow has also been initiated. Like the 2-D case, the 3-D method applies the non-linear free surface boundary condition on the exact location of the free surface, instead of otherwise approximate conditions utilized in other methods.

Center for the Commercial Deployment of Transportation Technologies

This method has been applied to two of the Pacific Marine lifting bodies, and results are compared with available experimental data, as well as other CFD results. They indicate good agreement. At this stage of the program, the 3-D free surface code has shown to be stable and produces reasonable results. A number of improvements, as well as a more comprehensive validation effort, are planned for the next phase. Also planned are at-sea trials of the optimized body by Pacific Marine in order to validate our results.

BIBLIOGRAPHY

1. Parametric Technology Corporation, *Pro/Engineer* software, <http://www.ptc.com/>
2. ICEMCFD Engineering, Inc., *ICEMCFD* software, <http://www.icemcfd.com/>
3. E. Besnard, A. Schmitz, K. Kaups, G. Tzong, H. Hefazi, H.H. Chen, O. Kural, and T. Cebeci, "Hydrofoil Design and Optimization for Fast Ships," *Proceedings of the 1998 ASME International Congress and Exhibition*, Anaheim, CA, November 1998.
4. Engineous Software, Inc., *iSIGHT* software, <http://www.engineous.com/>
5. J.L. Hess, D.M. Firedman, and R.W. Clark, *Calculation of compressible flow about three-dimensional inlets with auxiliary inlets, slats, and vanes by means of a panel method*. McDonnell Douglas Report No. MDC J3789, 1985; also NASA CR-174975 and AIAA Paper No. AIAA-85-1196.
6. T. Cebeci, *An Engineering Approach to the Calculation of Aerodynamic Flows*, Springer-Verlag, 1999.
7. T. Cebeci and P. Bradshaw, *Physical and Computational Aspects of Convective Heat Transfer*, Springer-Verlag, 1984.
8. Squire, H.B., and Young, A.D., *The calculation of the profile drag of aerofoils*, ARC RM 1838, 1938.
9. S. Hoerner, *Fluid-Dynamics Drag*, Horner, 1965.
10. R. Gornstein, *Private Communication*, Navatek, Ltd., HI, 2000.
11. Abbott, I.H. and Von Doenhoff, A.E., *Theory of Wing Sections*, Dover Publications, Inc., NY, 1959.
12. M.L. Stein, *Large Sample Properties of Simulations using Latin Hypercube Sampling*, *Technometrics*, 29 (2): 143-151, 1987.
13. J.H. Holland, *Adaptation in Natural and Artificial Systems*, University of Michigan Press, Ann Arbor, 1975.
14. D. Goldberg, *Genetic Algorithms in Search, Optimization, and Machine Learning*, Addison-Wesley, 1989.

Center for the Commercial Deployment of Transportation Technologies

15. C.W. Dawson, "A Practical Computer Method for Solving Ship-Wave Problems," *Proceedings*, Second International Conference on Numerical Ship Hydrodynamics, Berkeley, 1977.
16. S.-Y. Ni, "A Method for Calculating Nonlinear Free Surface Potential Flows Using Higher-Order Panels," Ph.D. Thesis, Chalmers University, Gothenburg, Sweden, 1987.
17. G. Jensen, V. Bertram, and H. Soding, "Ship Wave-Resistance Computations," *Proceedings*, Fifth International Conference on Numerical Ship Hydrodynamics, Hiroshima, Japan, 1988.
18. H.C. Raven, "A Practical Nonlinear Method for Calculating Ship Wavemaking and Wave Resistance," 19th Symposium on Naval Hydrodynamics, Seoul, Korea, 1992.
19. H.C. Raven, "A Solution Method for the Nonlinear Ship Wave Resistance Problem," Doctoral Thesis, Maritime Research Institute, Netherlands, 1995.
20. J.L. Hess, "Panel Methods in Computational Fluid Dynamics," *Annual Review of Fluid Mechanics*, Vol. 22, pp. 255-274, 1990.
21. J.L. Hess, "Progress in the Calculation of Nonlinear Free-Surface Problems by Surface-Singularity Techniques," *Proceedings*, Second International Conference on Numerical Ship Hydrodynamics, Berkeley, 1977.
22. H. Lamb, *Hydrodynamics*, Dover Publications, New York, 1945.
23. D.C. Scullen and E.O. Tuck, "Nonlinear Free-Surface Flow Computations for Submerged Cylinders," *Journal of Ship Research*, Vol. 39, pp. 185-193, 1995.
24. J.H. Duncan, "The Breaking and Non-Breaking Wave Resistance of a Two-Dimensional Hydrofoil," *Journal of Fluid Mechanics*, Vol. 126, pp. 507-520, 1983.
25. T. Hino, L. Martinelli, and A. Jameson, "A Finite-Volume Method with Unstructured Grid for Free Surface Flow Simulations," *Proceedings*, Sixth International Conference on Numerical Ship Hydrodynamics, Iowa, 1993.
26. J.S. Ausman, "Pressure Limitation on the Upper Surface of a Hydrofoil," Ph.D. Thesis in Mechanical Engineering, University of California, Berkeley, 1954.

LIST OF TABLES

<u>Table</u>	<u>Description</u>	<u>Page Number</u>
1	Lift for the baseline configuration at 0 degree angle of attack.....	17
2	Baseline performance, $\alpha = 0^\circ$	17
3	Parameters defining each component and their relative placement.....	18
4	Foil cross-section parametric definition.....	21
5	Design space	28
6	Optimized vs. Baseline configuration definition	32
7	Performance of optimized vs. baseline configuration-IBL-Neg. Method	33
8	Performance of optimized configuration with various CFD methods	39
9	Mesh sensitivity test case parameters	58

LIST OF FIGURES

<u>Figure</u>	<u>Description</u>	<u>Page Number</u>
1	Artist's Concept of LSC(X).....	3
2	Twin H-body Configuration, Baseline.....	5
3	Flow chart of the numerical optimization.....	6
4	Free surface flow.....	8
5	Induced velocities with positive image.....	9
6	Induced velocities with negative image.....	9
7	Interactive Boundary Layer approach.....	10
8	Midfoil configuration (submerged parts in red).....	11
9	Pressure distribution on the Midfoil	12
10	Comparison between measured and calculated pressure distribution at $y = 5$ ft.	12
11	Log Law profiles at $y = 5$ ft on the Midfoil lower surface at 17.1 ft from the leading edge	13
12	Log Law profiles at $y = 5$ ft on the Midfoil upper surface at 20.1 ft from the leading edge	14
13	Dynamic pressure coefficient distribution over the baseline Twin-H Configuration	15
14	Pressure distribution computed by the CSULB IBL method with negative images (IBL-Neg.) and free surface code (wave) on	15
	a) the H-body (at $y = 3.8$ m)	15
	b) on the strut (at $z = 0.12$).....	16
	c) on the cross-foil (at $y = 0.4$ m – centerline is at $y = 0$), concluded	16
15	Components of the Twin H-Body Configuration a) cross-foil, b) H-body, and c) strut.....	18
16	Paneling distribution on Twin H-Body Configuration	20
17	Latin hypercube sampling.....	22
18	Optimization process	24
19	From design variables to Pro-Engineer files – <i>runShape</i>	25
20	From Pro-Engineer files to surface mesh – <i>create_mesh</i>	26
21	From surface mesh to flow solution, objective function, and constraint determination – <i>runDAC</i>	27
22	Absolute percentage variation in L/D for 1% change in design variable	30
23	Absolute percentage variation in L/D for 1 degree change in angle	31
24	Dynamic pressure comparison between the baseline (Top half of the picture) and optimized configuration (bottom half). <i>Top view</i>	34

Center for the Commercial Deployment of Transportation Technologies

25	Dynamic pressure comparison between the baseline (top half of the picture) and optimized configuration (bottom half). <i>Bottom view</i>	35
26	Pressure distribution on cross-foil at.....	37
	a) $y = 0.4\text{m}$ (near center)	
	b) $y = 2.22\text{m}$ (near junction with H-body)	
27	Dynamic pressure distribution on H-body.....	38
	a) inner section ($y = 3.1\text{m}$)	
	b) outer section ($y = 3.9\text{m}$)	
28	Coordinate system for free surface flow over submerged bodies.....	42
29	Flow chart of the iterative procedure.....	44
30	Waves produced by a circular cylinder at $F_r = 1$ with $a/d = 0.05$	46
31	Wave pattern for flow past a circular cylinder with $a/d = 0.2$	47
32	Wave pattern of the NACA 0012 hydrofoil at 4° angle of attack with $F_r = 0.5$, $d/c = 1$	48
33	Pressure distribution of the NACA 0012 hydrofoil at 4° angle of attack.....	48
34	Wave pattern of the NACA 0012 hydrofoil at 5° angle of attack with $F_r = 0.567$, $d/c = 1.286$	49
35	Wave pattern of the NACA 0012 hydrofoil at 5° angle of attack with $F_r = 0.567$, $d/c = 1.162$	50
36	Wave pattern of the NACA 0012 hydrofoil at 5° angle of attack with $F_r = 0.567$, $d/c = 1.034$	50
37	Pressure distribution of the NACA 0012 hydrofoil at 5° angle of attack with $F_r = 0.567$, $d/c = 1.034$	51
38	Pressure distribution of the NACA 4412 hydrofoil at 4.7° angle of attack with $F_r = 1.035$, $d/c = 1.3$	52
39	Pressure distribution of the NACA 4412 hydrofoil at 2.3° angle of attack with $F_r = 0.962$, $d/c = 0.288$	52
40	Computed Dipole Distribution on Horizontal Lifting Surfaces.....	56
41	Computed Dipole Distribution on Vertical Strut.....	56
42	Wave Height Z in meters.....	59
43	Wave Height Z in meters.....	60
44	Wave Height Z in meters.....	61
45	Midfoil (submerged) Wave shape at $y=0$	62
46	Comparison of the experimental and CFD pressure data.....	63
47	Sea surface height for Midfoil Geometry.....	64
48	Sea surface shape to Twin-H body.....	65

GLOSSARY

Symbols

L : lift

$$C_p = \frac{p - p_{atm}}{q_\infty} = 1 - \left(\frac{V}{V_\infty}\right)^2 - \frac{2}{F_r^2} \left(\frac{z}{L}\right) : \text{pressure coefficient}$$

$$C_{pd} = \frac{p - p_\infty}{q_\infty} = 1 - \left(\frac{V}{V_\infty}\right)^2 : \text{dynamic pressure coefficient}$$

D : drag

$$F_r = \frac{V_\infty}{\sqrt{gL}} : \text{Froude number}$$

g : gravitational acceleration

k : roughness height

L : reference length

p : pressure

$$q = \frac{1}{2} \rho V^2 : \text{dynamic pressure}$$

$$R_L = \frac{VL}{\nu} : \text{Reynolds number based on a length } L$$

V : velocity

$$u_\tau = \sqrt{\frac{\tau_w}{\rho}} : \text{friction velocity}$$

(x, y, z) : Cartesian coordinate system; x : flow direction over submerged body; y : spanwise direction; z : vertical direction pointing upwards (i.e. submerged hull is at $z < 0$)

α : angle of attack

ρ : density

ν : kinematic viscosity

Subscripts

∞ : far-field, or infinity

atm : atmospheric

Acronyms

CFD: Computational Fluid Dynamics

FE: Finite Element

LT: long tons

ACKNOWLEDGEMENT

This work is the combined effort of a team of CSULB faculty, Pacific Marine staff, and several consultants. Major contributors to the work, and co-authors of this report, are: Drs. Eric Besnard and H.H. Chen, Adeline Schmitz, and AK. Khattab, from CSULB, as well as Roger Clark and A. Egan, independent contractors.

Computational Fluid Dynamics Tool Development and Validation

A General Interactive Boundary-layer Method for Three-dimensional Flows

By

**K. C. Chang
The Boeing Company
kuo-cheng.chang@boeing.com**

Prepared under

**CCDoTT Task 2.8
DTM91-97-H-00007**

**For
California State University, Long Beach**

September 2001

Table of Contents

	Summary	
1.0	Introduction	
2.0	Interactive Boundary-layer Method	
2.1	Introduction	
2.2	Quasi Three-dimensional Boundary-layer Equations	
2.3	Transformed Equations	
2.4	Numerical Method	
3.0	Computer Programs	
4.0	Results	
4.1	Two-dimensional Flows	
4.2	Three-dimensional Flows	
	4.2.1 Displacement Thickness versus Transpiration Velocity Approaches – 2D Boundary-layer Method	
	4.2.2 Two-dimensional versus Quasi Three-dimensional Method – Displacement Surface Approach for Three-dimensional Flows	
5.0	User's Manual for the Boundary-layer Programs	
6.0	Concluding Remarks	
7.0	References	

Summary

This report describes a general boundary-layer method and a computer program for calculating three-dimensional flows and for introducing viscous effects into panel methods by the use of displacement surface approach. For a given inviscid velocity distribution, freestream conditions and body geometry, the boundary-layer method provides solutions of both two-dimensional and quasi three-dimensional boundary-layer equations. An inverse boundary-layer procedure employing Veldman interaction law links the solutions of the inviscid and viscous flow equations. The output of the method includes the usual boundary-layer parameters such c_f , θ , δ^* , etc. as well as a new body geometry that includes the displacement thickness due to viscous effects. A test case is also given to facilitate the application of the computer program to other cases.

1.0 INTRODUCTION

An accurate prediction of hydrodynamic lift and drag for a given configuration can be obtained by either solving the Navier-Stokes equations (NS methods) or by coupling an inviscid method with a boundary layer method (IBL method). In recent years, there has been significant progress in the NS methods due to the advent of supercomputers and computation algorithms. Today the calculations are being performed routinely with NS methods not only for 2d flows but also for complex aircraft and ship configurations. However, the NS methods require huge computer resources and for general configurations, require grids, which may take weeks or even months to generate. Since an engineering design may require hundreds or thousands of calculations, the NS methods are not very suitable for engineering design studies.

In an IBL method, the external flow field is calculated from an inviscid method and a boundary layer method is used to calculate the displacement thickness distribution, which is used to incorporate viscous effects into the inviscid flow method. This method is efficient, reliable and accurate enough for many engineering design studies.

In an IBL method, one can pursue two approaches to incorporate the displacement thickness effects due to viscosity into the inviscid flow method. One is to use the transpiration approach in which the blowing velocity distribution on the surface is calculated by taking the derivative of the displacement thickness and the external velocity. The blowing velocity is then used as the wall boundary condition in inviscid flow calculations. The advantage of this approach is that there is no need to generate a new geometry, the calculated results are not sensitive to the smoothness of the blowing velocity, and hence the displacement thickness. The incorporation of this approach into the inviscid flow method, however, requires extensive modification of the inviscid flow method and expertise in both inviscid and viscous flow methods.

Another approach to use is the displacement method in which the calculated displacement thickness distribution from the boundary layer method is added to the original geometry to form a new geometry, which is then used to calculate inviscid flow to simulate viscous effects. This approach requires generating a new geometry each time a new displacement thickness distribution is obtained. It is not as efficient as the transpiration velocity approach and may be sensitive to smoothness of the displacement thickness distribution. However, this approach does not need any modifications to the inviscid flow method. It is applicable even when there is no source code available. So it is a more practical approach to include viscous effects in an inviscid flow method.

The objective of the work reported here is to use the second approach and develop an interactive boundary-layer method that can be used with an inviscid flow method to introduce viscous corrections. The development of such a method requires solving the boundary-layer equations in an interactive mode. The boundary-layer equations to be

solved could be in two dimensions or in three dimensions. The two-dimensional boundary-layer equations are easier to solve and require less computer time. Its use to account for viscous effects is found to be satisfactory in most cases. However, for complex geometry, where flow is highly three-dimensional, the two-dimensional boundary-layer method may not be sufficient and a three-dimensional boundary-layer method is then required to accurately account for viscous effects. As a result in this report we consider both two- and three-dimensional boundary-layer solutions to incorporate the viscous effects into an inviscid method.

The following section presents a brief summary of the interactive boundary layer (IBL) method used for this purpose. It is followed by a description of the computer program for the IBL method (Section 3.0) and by section that presents results and evaluation of the method with the transpiration velocity approach (Section 4.0). Section 5.0 gives a short description of the user's manual for the boundary-layer program. Concluding statements are presented in Section 6.0.

2.0 INTERACTIVE BOUNDARY-LAYER METHOD

2.1 Introduction

The procedure of coupling inviscid-flow and boundary-layer equations has been popular for many years. However, completely satisfactory results are still difficult to obtain for general flows. The main obstacle to this goal is associated with separation. When the boundary-layer equations are solved for a prescribed pressure distribution, the solutions break down at the point of vanishing wall shear (i.e. separation). However, the solutions do not break down if the external flow velocity is computed as part of the solution by, for example, prescribing a displacement thickness: this is known as the inverse method and allows the solution of the boundary-layer equations with separation.

There are several approaches [1,2,3] that can be used in an inverse method. One is the Hilbert integral approach due to Veldman [3] in which the external velocity, $u_e(x)$, distribution for two-dimensional flows is written as

$$u_e(x) = u_e^o(x) + \delta u_e(x) \quad (2.1)$$

Here $u_e^o(x)$ is the inviscid velocity and δu_e is the perturbation velocity due to displacement thickness distribution. It is given by

$$\delta u_e(x) = \frac{1}{\pi} \int_{x_a}^{x_b} \frac{d}{d\sigma} (u_e \delta^*) \frac{d\delta}{x - \sigma} \quad (2.2)$$

The above expression is based on the thin airfoil approximation with the term $\frac{d}{d\sigma} (u_e \delta^*)$ denoting the blowing velocity used to simulate the boundary-layer effects in the interaction region (x_a, x_b) . The interaction law given by Eqs. (2.1) and (2.2) is also applicable to three-dimensional flow under the quasi-three-dimensional approximation for which the spanwise pressure gradient is small. [4]

In the study reported here, we account for viscous effects by using two-dimensional and quasi-three-dimensional inverse interactive boundary-layer methods. The two-dimensional inverse boundary-layer method is reported in several papers and books, for example, Ref 4. Here we only describe the quasi-three-dimensional inverse boundary-layer method.

2.2 Quasi Three-Dimensional Boundary-layer Equations

Consider a flow over a three-dimensional body defined in the Cartesian coordinate system $(\bar{x}, \bar{y}, \bar{z})$ by

$$F(\bar{x}, \bar{y}, \bar{z}) = 0 \quad (2.3)$$

A convenient coordinate system for three-dimensional boundary-layer equations for laminar and turbulent flows is a non-orthogonal and curvilinear system. Let x and z denote the boundary-layer coordinate system on the surface, θ the angle between the coordinate lines x and z , and y the distance measured normal to the surface. The three-dimensional boundary-layer equations and their boundary conditions for steady incompressible laminar and turbulent flows can be written in this coordinate system in the following form.

Continuity Equation

$$\frac{\partial}{\partial x}(uh_2 \sin \theta) + \frac{\partial}{\partial z}(wh_1 \sin \theta) + \frac{\partial}{\partial y}(vh_2 h_1 \sin \theta) = 0 \quad (2.4)$$

x – Momentum Equation

$$\begin{aligned} \frac{u}{h_1} \frac{\partial u}{\partial x} + \frac{w}{h_2} \frac{\partial u}{\partial z} + v \frac{\partial u}{\partial y} - k_1 u^2 \cot \theta + k_2 w^2 \csc \theta + uwk_{12} \\ = -\frac{\csc^2 \theta}{\rho h_1} \frac{\partial p}{\partial x} + \frac{\cot \theta \csc \theta}{\rho h_2} \frac{\partial p}{\partial z} + \frac{\partial}{\partial y} \left(v \frac{\partial u}{\partial y} - \overline{u'v'} \right) \end{aligned} \quad (2.5)$$

z – Momentum Equation

$$\begin{aligned} \frac{u}{h_1} \frac{\partial w}{\partial x} + \frac{w}{h_2} \frac{\partial w}{\partial z} + v \frac{\partial w}{\partial y} + k_1 u^2 \csc \theta - k_2 w^2 \cot \theta + uwk_{21} \\ = -\frac{\csc^2 \theta}{\rho h_2} \frac{\partial p}{\partial z} + \frac{\cot \theta \csc \theta}{\rho h_1} \frac{\partial p}{\partial x} + \frac{\partial}{\partial y} \left(v \frac{\partial w}{\partial y} - \overline{w'v'} \right) \end{aligned} \quad (2.6)$$

Boundary Conditions

$$y = 0, u = v = w = 0; \quad y = \delta, u = u_e(x), w = w_e(x) \quad (2.7)$$

Here h_1 and h_2 denote the surface metric coefficients, and θ denotes the angle between the coordinate lines x and z and, as a result of first-order boundary-layer theory, the metric coefficients are functions of the surface coordinates x and z only. They can be obtained from the relation between $\bar{x}, \bar{y}, \bar{z}$ and x, y, z and are given by

$$h_1^2 = \left(\frac{\partial \bar{x}}{\partial x} \right)^2 + \left(\frac{\partial \bar{y}}{\partial x} \right)^2 + \left(\frac{\partial \bar{z}}{\partial x} \right)^2 \quad (2.8a)$$

$$h_2^2 = \left(\frac{\partial \bar{x}}{\partial z}\right)^2 + \left(\frac{\partial \bar{y}}{\partial z}\right)^2 + \left(\frac{\partial \bar{z}}{\partial z}\right)^2 \quad (2.8b)$$

$$\cos \theta = \frac{(\partial \bar{x} / \partial x)(\partial \bar{x} / \partial z) + (\partial \bar{y} / \partial x)(\partial \bar{y} / \partial z) + (\partial \bar{z} / \partial x)(\partial \bar{z} / \partial z)}{h_1 h_2} \quad (2.9)$$

The parameters K_1 and K_2 are known as the geodesic curvatures of the curves $z = \text{constant}$ and $x = \text{constant}$, respectively, and are given by

$$K_1 = \frac{1}{h_1 h_2 \sin \theta} \left[\frac{\partial}{\partial x} (h_2 \cos \theta) - \frac{\partial h_1}{\partial z} \right] \quad (2.10a)$$

$$K_2 = \frac{1}{h_1 h_2 \sin \theta} \left[\frac{\partial}{\partial z} (h_1 \cos \theta) - \frac{\partial h_2}{\partial x} \right] \quad (2.10b)$$

The parameters K_{12} and K_{21} are defined by

$$K_{12} = \frac{1}{\sin \theta} \left[-K_1 - \frac{1}{h_1} \frac{\partial \theta}{\partial x} + \cos \theta \left(K_2 + \frac{1}{h_2} \frac{\partial \theta}{\partial z} \right) \right] \quad (2.11a)$$

$$K_{21} = \frac{1}{\sin \theta} \left[-K_2 - \frac{1}{h_1} \frac{\partial \theta}{\partial z} + \cos \theta \left(K_1 + \frac{1}{h_1} \frac{\partial \theta}{\partial x} \right) \right] \quad (2.11b)$$

The magnitude of the velocity vector u_t in the boundary layer is given by

$$u_t = (u^2 + w^2 + 2uw \cos \theta)^{1/2} \quad (2.12)$$

Assuming that the spanwise pressure gradients are small, the flow variations with respect to z can be neglected. This assumption allows the equations to be reduced to a form which provides a better approximations to Eqs. (2.4) to (2.7) than those based on the two-dimensional theory or infinite-swept-wing approximations. The resulting equations are referred to as quasi-three-dimensional equations and are written as

$$\frac{\partial}{\partial x} (u h_2 \sin \theta) + \frac{\partial}{\partial y} (v h_2 h_1 \sin \theta) = 0 \quad (2.13)$$

$$\frac{u}{h_1} \frac{\partial u}{\partial x} + v \frac{\partial u}{\partial y} - K_1 u^2 \cot \theta + K_2 w^2 \csc \theta + uwK_{12} = -\frac{\csc^2 \theta}{\rho h_1} \frac{\partial p}{\partial x} + \frac{\partial}{\partial y} (v \frac{\partial u}{\partial y} - \overline{u'v'}) \quad (2.14)$$

$$\frac{u}{h_1} \frac{\partial w}{\partial x} + v \frac{\partial w}{\partial y} + K_1 u^2 \csc \theta - K_2 w^2 \cot \theta + uwK_{21} = \frac{\cot \theta \csc \theta}{\rho h_1} \frac{\partial p}{\partial x} + \frac{\partial}{\partial y} (v \frac{\partial w}{\partial y} - \overline{w'v'}) \quad (2.15)$$

Eqs. (2-13) to (2.15) contain Reynolds shear stress terms, $-\overline{u'v'}$ and $-\overline{v'w'}$, which have to be modeled in order to reduce the number of the unknowns to the number of the equations. There are several approaches for this purpose. The most common one is to use an eddy viscosity, ν_t , in which Reynolds shear stress terms are related to the gradient of the mean velocity profiles by

$$-\overline{u'v'} = \nu_t \frac{\partial u}{\partial y}, \quad -\overline{v'w'} = \nu_t \frac{\partial w}{\partial y} \quad (2.16)$$

There are several methods to obtain the eddy viscosity. It can be obtained by solving transport equations like k- ϵ model in which two transport equations, one for the turbulent kinetic energy, k, and the other for the rate of turbulent energy dissipation, ϵ ; it can also be obtained by using algebraic expressions, like the Cebeci-Smith (CS) model. This model has been proved to accurately predict flows for wide range of angles of attack including stall and post-stall. It is given in several references, see Ref 4, for example, and is not discussed here.

2.3 Transformed Equations

The boundary-layer equations of the previous section can be solved in physical or transformed coordinates and each has its advantages. The transformed coordinates are more convenient because they allow large steps to be taken and can be used to generate the initial conditions at the stagnation point for two-dimensional flow or along the attachment line for three-dimensional flows. There are several transformations that can be used for this purpose. Here we use two kinds of transformation. In the region where the boundary-layer equations are solved in the standard mode in which the external velocity, u_e , is prescribed, an extension of the two-dimensional Falkner-Skan transformation to three-dimensional flows is used. In the region where the boundary-layer equations are solved in the inverse mode in which the external velocity, u_e , is part of the solution, the transformation needs to be modified. This is done by using the transformation:

$$x = x, \quad d\eta = \left(\frac{u_o}{vs_1} \right)^{1/2} dy \quad (2.17)$$

Here u_o is a reference velocity and s_1 denotes the arc length in the longitudinal direction measured from the initial line $x = x^*$. The dependent variables are transformed by using a two-component velocity potential such that

$$uh_2 = \frac{\partial \varphi}{\partial y}, \quad wh_1 = \frac{\partial \phi}{\partial y}, \quad vh_1h_2 = -\frac{\partial \varphi}{\partial x} \quad (2.18)$$

In addition, dimensionless velocity potentials, φ and ϕ , are defined by

$$\varphi = (vu_o s_1)^{1/2} h_2 f(x, \eta), \quad \phi = (vu_o s_1)^{1/2} g(x, \eta) \quad (2.19)$$

With the transformations defined by Eqs. (2.17) to (2.19) and with the definition of eddy viscosity, Eq. (2.16), the quasi-three-dimensional boundary-layer equations, Eqs. (2.13) to (2.15) and their boundary conditions can be written in the following form:

$$(bf'')' + m_1 ff'' + m_2 (f')^2 + m_5 f' g' + m_8 (g')^2 + m_{11} = m_{10} (f' \frac{\partial f'}{\partial x} - f'' \frac{\partial f}{\partial x}) \quad (2.20)$$

$$(bg'')' + m_1 fg'' + m_3 (g')^2 + m_4 f' g' + m_9 (f')^2 + m_{12} = m_{10} (f' \frac{\partial g'}{\partial x} - g'' \frac{\partial f}{\partial x}) \quad (2.21)$$

$$\eta = 0, \quad f = f' = g' = 0; \quad \eta = \delta, \quad f' = \frac{u_e}{u_o} = \bar{u}_e, \quad g' = \frac{w_e}{u_o} = \bar{w}_e \quad (2.22)$$

Here the primes denote differentiation with respect to η . The parameters, m_1 to m_{12} , and b are defined by

$$m_1 = \frac{\sqrt{s_1}}{h_1 h_2 \sin \theta} \frac{\partial}{\partial x} (\sqrt{s_1} h_2 \sin \theta), \quad m_2 = s_1 K_1 \cos \theta, \quad m_3 = s_1 K_2 \cot \theta$$

$$m_6 = \frac{\sqrt{s_1}}{h_1 h_2 \sin \theta} \frac{\partial}{\partial x} (\sqrt{s_1} h_1 \sin \theta), \quad m_4 = -s_1 K_{21} \cos \theta, \quad m_5 = -s_1 K_{12}$$

$$m_8 = -s_1 K_2 \csc \theta, \quad m_9 = -s_1 K_1 \csc \theta, \quad m_{10} = s_1 / h_1 \quad (2.23)$$

$$m_{11} = -m_2 \bar{u}_e^2 - m_5 \bar{u}_e \bar{w}_e - m_8 \bar{w}_e^2 + m_{10} \bar{u}_e \frac{\partial \bar{u}_e}{\partial x}$$

$$m_{12} = -m_9 \bar{u}_e^2 - m_4 \bar{u}_e \bar{w}_e - m_3 \bar{w}_e^2 + m_{10} \bar{u}_e \frac{\partial \bar{w}_e}{\partial x}$$

$$b = (1 + v_t^+), \quad v_t^+ = v_t / v$$

2.4 Numerical Method

The system of equations, (2.20) to (2.22) with the parameters, m_1 to m_{12} defined in Eq. (2.23) can efficiently be solved by using finite-difference methods. The Crank-Nicolson and the Keller's box method [5] are the most popular ones for this purpose. The Keller's box method has several advantages over the Crank-Nicolson method and is used here. This method is described in numerous papers and books and is not discussed here. Those who are interested in the method may refer to Ref. 4.

3.0 COMPUTER PROGRAMS

To introduce the viscous effects into inviscid flow calculations, we have developed two computer programs. One computer program provides solutions of two-dimensional boundary-layer equations in the inverse mode, and the other provides the solutions of quasi-three-dimensional boundary-layer equations described in the previous section, again in the inverse mode. Both computer programs calculate the displacement thickness distribution as well as the corresponding transpiration velocity distribution to be used in the inviscid-flow calculations to account for viscous effects. The programs also have options to calculate the viscous wake.

The two computer programs are written so that they are self-contained and portable. With minor modifications in the “interface subroutine”, which links the boundary-layer programs with inviscid flow program, they can be coupled with any inviscid panel method. They can also be stand-alone boundary-layer codes and calculate the viscous flow characteristics such as the boundary-layer profiles, skin-friction drag and form drag, flow separation, and location of transition where the flow changes from laminar to turbulent. The transition location is important since it influences not only the drag but also the lift. Both computer programs have several options to specify the transition location. It can be input at a particular location like the tripped location in a wind tunnel test; it can be specified at the leading edge or it can be determined from the computer programs according to a transition prediction method. For example, it is set at the location where the flow separates or the location where the Michel method is satisfied if the flow is two-dimensional. For two-dimensional flows the flow changing from laminar to turbulent is controlled exclusively by the streamwise flow instability (Tollmien-Schlichting wave). For three-dimensional flows, the flow that changes from laminar to turbulent can be due to the streamwise flow instability, due to the attachment-line contamination, or due to the cross-flow instability [6]. In the computer program solving the quasi-three-dimensional boundary-layer equations, options for the transition caused by all three mechanisms are included.

To test the two boundary-layer programs and to evaluate the viscous/inviscid interactions using the transpiration velocity approach and displacement surface approach, we have coupled the two boundary-layer programs to a Boeing three-dimensional panel code. The panel code uses Hess’ panel method to calculate the incompressible inviscid flow and employs various Mach number correction methods for compressibility effects. The code has the option to specify transpiration velocity distribution at the wall to simulate the viscous effects so that no significant modification is needed when it is coupled with the present boundary-layer codes. The panel code has been well validated and has been used widely at the Boeing Company for the analysis and design of high-lift systems. The panel code admits multiple angles of attack to be run in the inviscid flow calculations or in the viscous flow calculations with the transpiration velocity approach. When the displacement surface approach is used to simulate the viscous effects, a new geometry must be generated each time a new displacement thickness distribution is obtained. For a new geometry, panels change and the influence coefficient matrix and its solutions have

to be recalculated. The calculations of the matrix and its solutions are the most time-consuming task in the panel code. The present Boeing panel code does not allow the change of the geometry during the calculations. Modifying the code to allow this change is very involved and no attempt was made in this work. For the transpiration velocity approach, the calculations were made allowing interaction between the inviscid flow method and the inverse boundary-layer method. First, the inviscid flow solutions are obtained and the calculated pressure distribution is used for the inverse boundary-layer method. The boundary-layer method then provides the transpiration rate distribution, which is served as the new boundary condition for the inviscid flow method for a new pressure distribution. The iteration continues until the solutions converge. But for the displacement surface approach, this iterative procedure is not possible. Instead, we simply just use the converged IBL solutions of the blowing velocity method to generate a new geometry to obtain a new pressure distribution. Our main goal is to demonstrate that the displacement thickness approach is a feasible alternative to include viscous effects into the calculations to determine lift and drag coefficients and other flow parameters for a given configuration. The procedure we adopted for the displacement surface approach does this very well.

4.0 Results

The method and the computer programs described in the previous sections are used to evaluate the accuracy of the displacement surface approach with the well-established blowing velocity approach. In Section 4.1 we present results obtained with these two approaches for a NACA 0012 airfoil for different angles of attack and Reynolds number. In Section 4.2, we compare results for a finite tapered wing using two-dimensional and quasi three-dimensional boundary-layer methods described in Section 2.

4.1 Two-dimensional Flows

To evaluate the accuracy of the displacement surface approach for two-dimensional flows, we use a Boeing two-dimensional panel/boundary-layer code, which employs the blowing velocity approach to account for viscous effects. We make appropriate changes to this method so that it can also be used for viscous effects using the displacement surface approach. According to this method, we first calculated the inviscid flow to obtain a pressure distribution needed for the inverse boundary-layer method. The boundary-layer solutions are then used to obtain the displacement thickness or blowing velocity distributions to be used to obtain a new pressure distribution. The procedure is repeated until the solutions converge for each angle of attack.

Figures 1 to 3 show results for the NACA 0012 airfoil for angles of attack from 1.0 to 5.0 degrees and Reynolds numbers of 5 to 30 millions. Figure 1 shows lift coefficient, C_l , distributions with and without viscous effects with the two approaches for Reynolds numbers of 5 and 20 millions. As can be seen, the blowing velocity approach consistently gives higher lift than the displacement surface approach, but the difference between the two approaches is much smaller than the difference between the inviscid flow and viscous flow solutions. The effect of the Reynolds number on predicted lift (C_l) and drag (C_d) coefficients is shown in Fig. 2. As the Reynolds number increases, the predicted C_l increases and the C_d decreases in both approaches, consistent with experimental results. The thickness at the trailing edge of the airfoil after the displacement thickness is added to the airfoil is shown in Fig. 3. The thickness (i. e. open trailing edge) is up to more than 1% of the airfoil chord length, and this open trailing edge does not produce any undesirable results as evidenced by the pressure distributions shown in Fig. 4. These results demonstrate that the displacement surface approach to include the viscous effects in inviscid flow calculations is feasible and as accurate as the blowing velocity approach.

4.2 Three-dimensional Flows

To evaluate the accuracy of the displacement surface approach for three-dimensional flows, we use the computer program described in the previous section and obtain a solution of the boundary-layer equations using 2d strip theory and quasi 3d boundary-layer approximations. We choose a finite-swept tapered wing based on a NACA 0012

airfoil. This wing has leading-edge and trailing-edge backward sweep angles of 17.5° and 10.0° , respectively. Fig. 5(a) shows the inviscid lift coefficient, C_l , distribution for the angles of attack up to 7.0 degrees with different panel distributions, and Fig. 5(b) shows the section C_l distributions for an angle of attack of 7.0 degrees. As can be seen, the solutions with the panels of 100×14 are sufficiently close to those with extremely fine panels of 100×24 for the given configuration. Therefore, this panel distribution of 100×14 was used for the results presented here.

4.2.1 Displacement Thickness versus Transpiration Velocity Approaches – 2D Boundary-layer Method

Figures (6) to (9) show results obtained with the displacement surface and blowing velocity approaches for the angles of attack up to 7.0 degrees and the Reynolds numbers of 5 to 20 million. The boundary-layer solutions were obtained with the two-dimensional boundary-layer method. Fig. 6 shows comparison of a C_l distribution for the Reynolds numbers of 5 million and 20 million with these two approaches together with inviscid flow solutions. Similar to the results for two-dimensional flows presented in the previous section, the lift coefficient, C_l , obtained with the displacement surface approach is consistently lower than that obtained with the blowing velocity approach. However, the difference is very small compared with the difference between the inviscid and the viscous flow solutions with either approach. The effect of Reynolds numbers is shown in Fig. 7. Again, as in two-dimensional flows, the predicted C_l increases as the Reynolds number increases. Fig. 8 shows the trailing-edge thickness (DTE) distributions for the Reynolds numbers of 5 million and 20 million, resulting from the addition of the calculated displacement thickness normal to the wing geometry. The DTE increases as the angle of attack increases and decreases as the Reynolds number increases. The DTE distribution is quite smooth except near the centerline of the wing, where the displacement thickness was extrapolated spanwise from the neighbor solutions. The somewhat abnormal DTE variation near the centerline does not influence the inviscid flow solutions as evidenced by the section C_l distributions shown in Fig. 9. The abnormality on the DTE distributions will be reduced or completely eliminated if the panel size near the center line decreases. From the results shown here, we can conclude that the displacement surface approach to account for viscous effects in three-dimensional flows is as accurate as the transpiration velocity approach.

4.2.2 Two-dimensional versus Quasi Three-dimensional Boundary-layer Methods – Displacement Surface Approach for Three-dimensional Flows

Studies conducted but not shown here indicate that for three-dimensional flows, the results obtained with the quasi-three-dimensional boundary-layer method for the displacement surface and blowing velocity approaches are similar to those with the two-dimensional boundary-layer method. For this reason, we only present results with the displacement surface approach using two-dimensional boundary-layer method in

comparison with those using quasi-three-dimensional boundary-layer method. Figs. 10 to 13 show the results for a NACA 0012 swept wing at angles of attack up to 7.0 degrees and the Reynolds numbers of 5 to 20 million. Fig 10 shows a comparison between the inviscid and viscous the lift coefficient, C_l , distributions for the Reynolds numbers of 5 million and 20 million. The calculated C_l by the quasi three-dimensional boundary-layer method is lower than the lift calculated by the two-dimensional boundary-layer method for all angles of attack and Reynolds number under consideration. The difference between the two methods increases as the angle of attack increases and the Reynolds number decreases, showing a strong swept angle and taper effects. The effect of the Reynolds number on the C_l distribution is also shown in Fig. 11. Fig. 12 compares the spanwise trailing edge thickness (DTE) distributions, which include the displacement thickness at the trailing edge of both upper and lower surfaces, with two-dimensional and quasi three-dimensional boundary-layer methods for the Reynolds number of 5 million. The DTE obtained with the quasi three-dimensional boundary-layer method is larger than the DTE calculated with the two-dimensional boundary-layer method for all angles of attack. The DTE increases smoothly from the tip to near the centerline of the wing. At the centerline of the wing, the DTE is extrapolated and its value there strongly depends on the variation of the values of the neighboring stations. Although the DTE distribution is not as smooth as one would like near the centerline, this behavior does not influence the results as evidenced by the section C_l distributions shown in Fig. 13.

5.0 User's Manual for the Boundary-Layer Programs

As described in Section 3, the two-dimensional and quasi three-dimensional boundary-layer programs are portable, self-contained, and multi-functioned. They can easily be coupled with any incompressible panel code with a suitable 'interface subroutine'. To discuss further, we consider a case that generates a displacement surface distribution to simulate viscous effects for a wing geometry and inviscid flow solution obtained by a panel code. The required input data are as follows.

1. File 1. This file is used to define wing geometry in "Hess" format of
(x,y,z,i1,i2)
Here i1 indicates the beginning of a new section (i1 = 2), or the beginning a new strip (i1 = 1), or an inner point (i1 = 0). (x, y, z) represent the Cartesian coordinates of the grid points. Since wing a lifting section, i2 must set equal to 1.
2. File 2. This file is used to input the three velocity components at their associated locations from a panel method in a format of
(xc, yc, zc, vx, vy, vz, i1).
Here (xc, yc, zc) represent the Cartesian coordinates, (vx, vy, vz) are the corresponding velocity components normalized by the freestream velocity U_∞ and i1 is defined the same as in the file 1.
3. File 5. This file is used to define the necessary input to perform the boundary-layer calculations for the geometry and inviscid velocity distributions given in Files 1 and 2.
NB1 : number of chordwise boundary layer grid for the first input surface
NB2 : number of chordwise boundary layer grid for the second input surface.
Cref : reference length used to in the definition of the Reynolds number. It must be in the same unit as the geometry coordinates.
Rc : Reynolds number based on the reference length, Cref, and the freestream velocity, $U_\infty \times Cref / \nu$.
IBL : option for the boundary-layer method;
= 1 for two-dimensional boundary-layer method
= 2 for quasi-three-dimensional boundary layer method.
ITR1 : Boundary-layer transition flag for the first input surface (0 for user specified x/c, 1 at the pressure suction peak and 2 for internally computed by Michel's criterion or at laminar separation point)
ITR2 : the same as ITR1 but for the second input surface.
XOC1 : x/c transition location on the first input surface (used only if ITR1 = 0).
XOC2 : x/c transition location on the second input surface (used only if ITR2 = 0).

In addition in this file we input Alpha and Beta, angle of attack and side angle. They are used only for printing purpose.

The output files include:

1. File 38. This file provides a summary of the boundary-layer solutions for each strip, including predicted transition location, location of flow separation and reattachment if any, the displacement thickness at the trailing edge, and skin friction drag and form drag coefficients
2. File 88. The file contains external velocity, displacement thickness, momentum thickness and skin-friction coefficient distributions etc. in the chordwise direction for each strip.
3. File 89. The file, only available for quasi three-dimensional boundary-layer option. It contains geometrical parameters related to three-dimensional boundary-layer coordinate system, θ , h_1 , h_2 , K_1 , K_2 , K_{12} , K_{21} , and U_e and W_e . The file is used for debugging purpose.
4. File 3. The file contains the displacement surface coordinates to be used for inviscid panel calculations. The coordinates are stored in 'Hess' format of $(x,y,z,i1,i2)$, with $i1$ and $i2$ having the same definition in the input file 1.

6.0 CONCLUDING REMARKS

In this report we have described a general method for calculating three-dimensional boundary-layer flows and for incorporating viscous effects into panel methods. We have used the displacement surface approach in which the displacement thickness is calculated from the boundary-layer equations and is added to the body geometry.

The method has been applied to airfoils and wings for a range of angles of attack and Reynolds number. The calculated results are compared with another approach, called the transpiration velocity approach, for incorporating viscous effects. Studies indicate that both approaches essentially produce same results and support the use of the displacement surface approach, which can be used with any panel method with essentially no changes to the panel method. The transpiration velocity approach, on the other hand, requires substantial changes to the panel method.

7.0 References

1. Carter, J. E., "A new Boundary-layer Inviscid Iteration Technique for Separated Flow," AIAA Paper 75-1450, 1979.
2. Kwon, O. K. and Pletcher, R. H., "Prediction of Incompressible Separated Boundary-layers Including Viscous-Inviscid Interaction," J. Fluids Engineering 101, 1979.
3. Veldman, A. E. P., "New, Quasi-Simultaneous Method to Calculate Interacting Boundary Layers," AIAA J., Vol. 19, 1981.
4. Cebeci, T., An Engineering Approach to the Calculation of Aerodynamic Flows, Horizon Publishing Inc., Long Beach, Ca., 1999.
5. Keller, H. B., Numerical Methods for Two-Point Boundary Value Problems, Ginn-Blaisdell, Waltham, Mass., 1968.
6. Poll, D. I. A., "Transition Description and Prediction in Three-dimensional Flows," in "Special Course on Stability and Transition of Laminar Flow," AGARD Report No. 709, 1984.

Fig. 1 Comparison of C_l Distributions
 N0012 Airfoil at (a) $Re = 5 M$ & (b) $Re = 20 M$

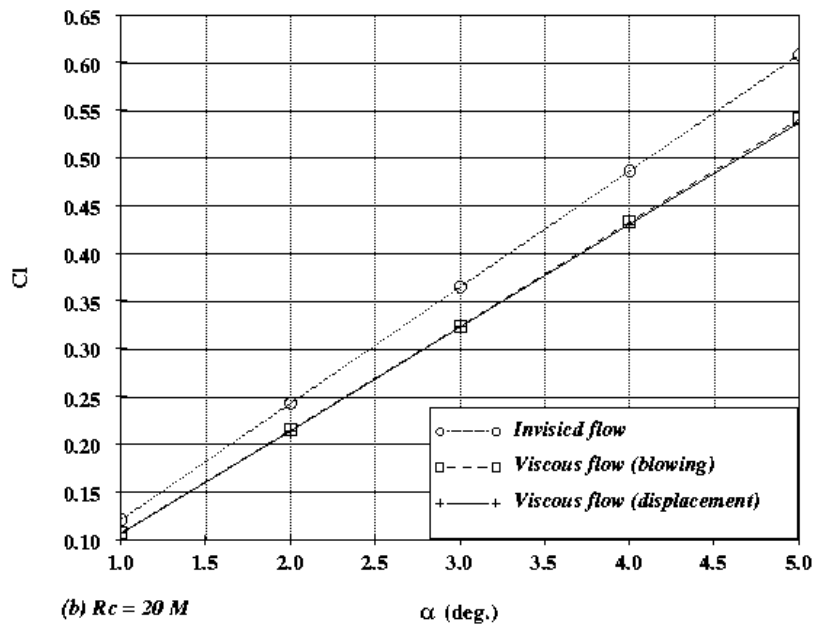
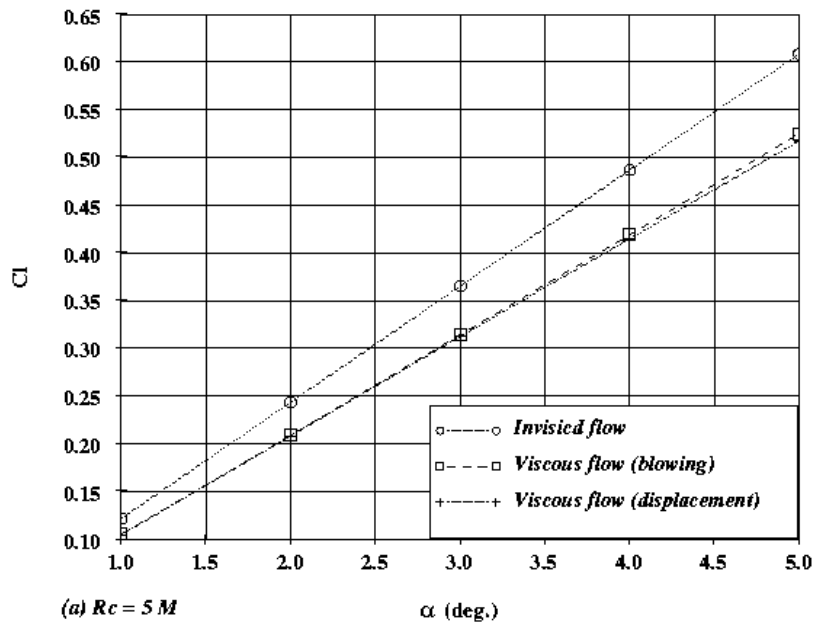


Fig. 2 Reynolds Number Effects on C_l & C_d Distributions
N0012 Airfoil

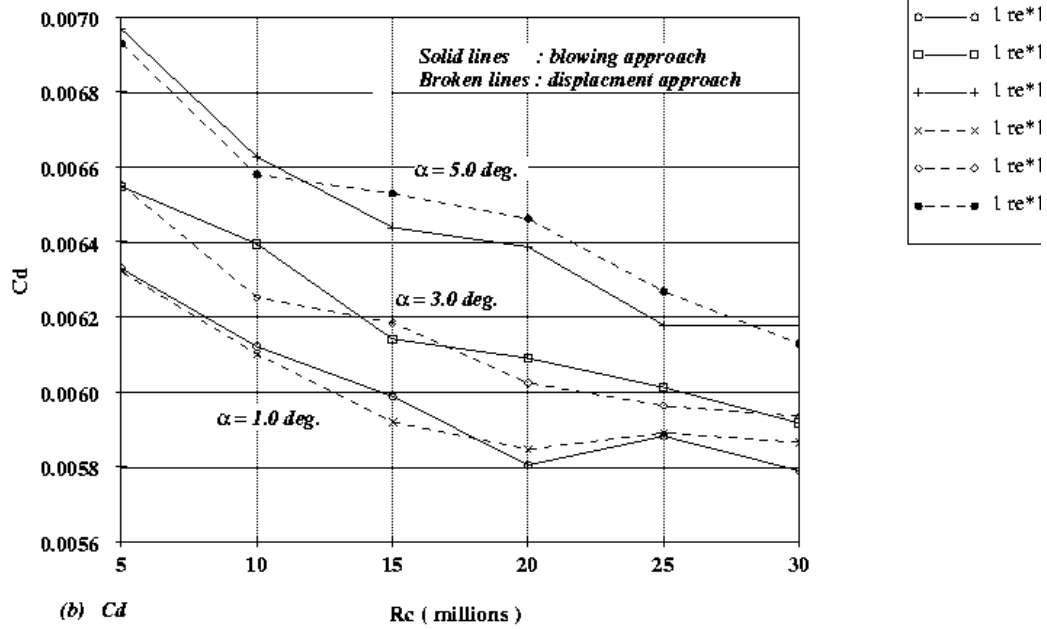
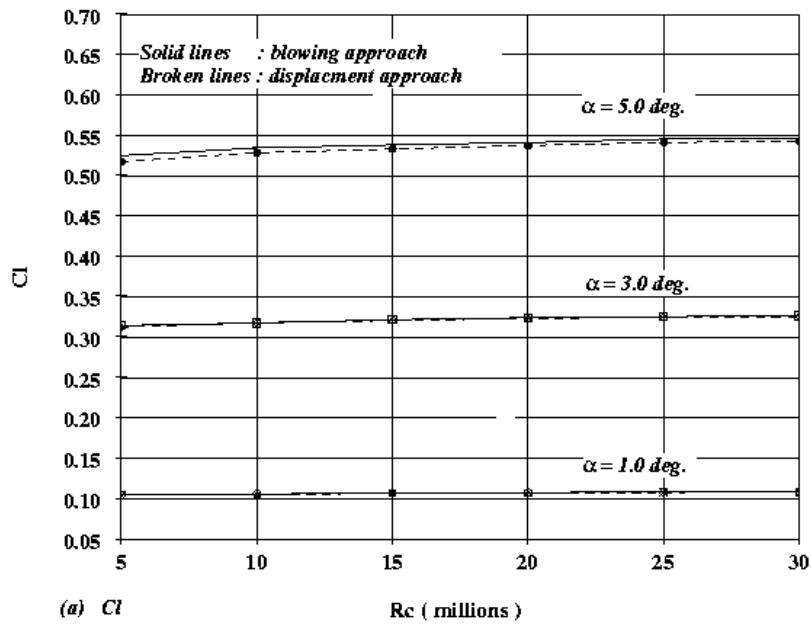


Fig. 3 Comparison of Original Geometry with Displacement Surfaces
N0012 at (a) $Re = 5.0 M$ & (b) $Re = 20.0 M$

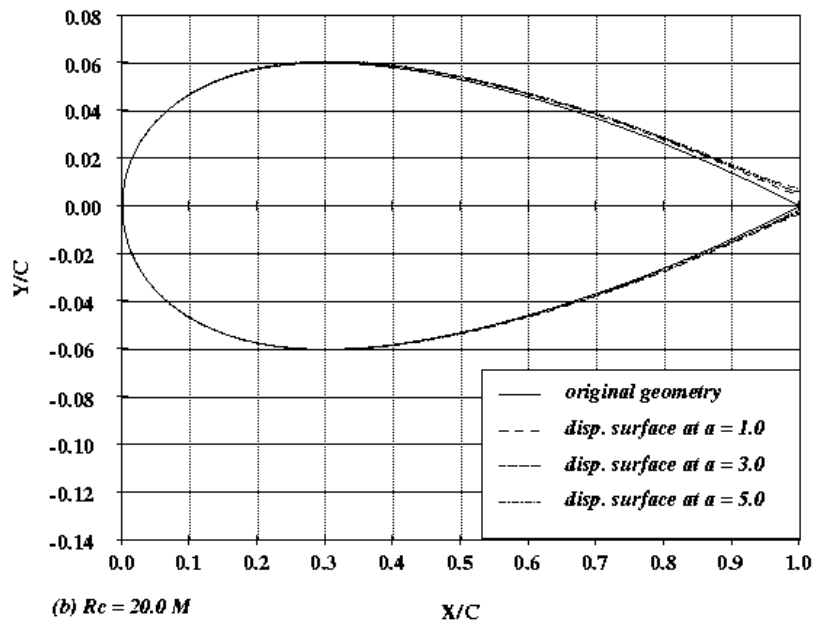
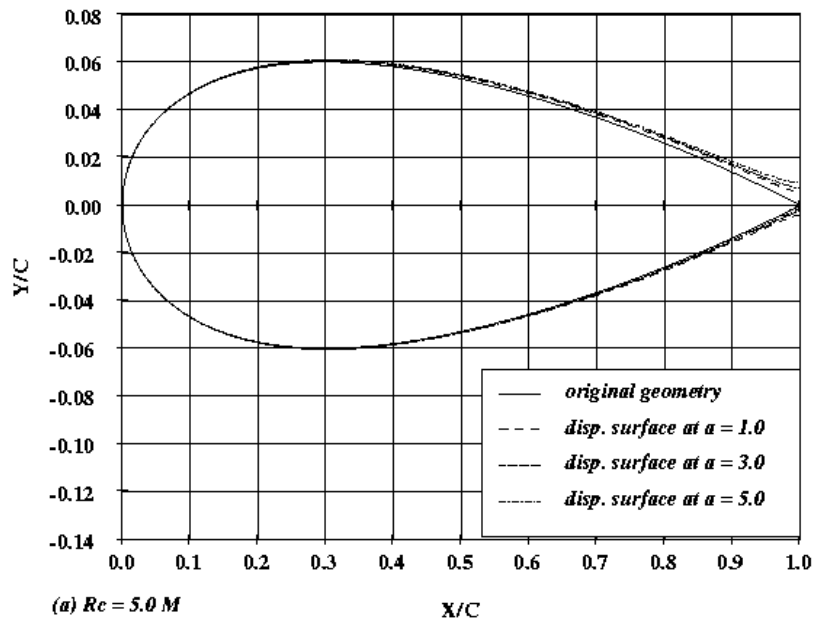


Fig. 4 Comparison of Cp Distributions
N0012 Airfoil at $\alpha = 5.0$ deg, and (a) $Re = 5M$ & (b) $Re = 20M$

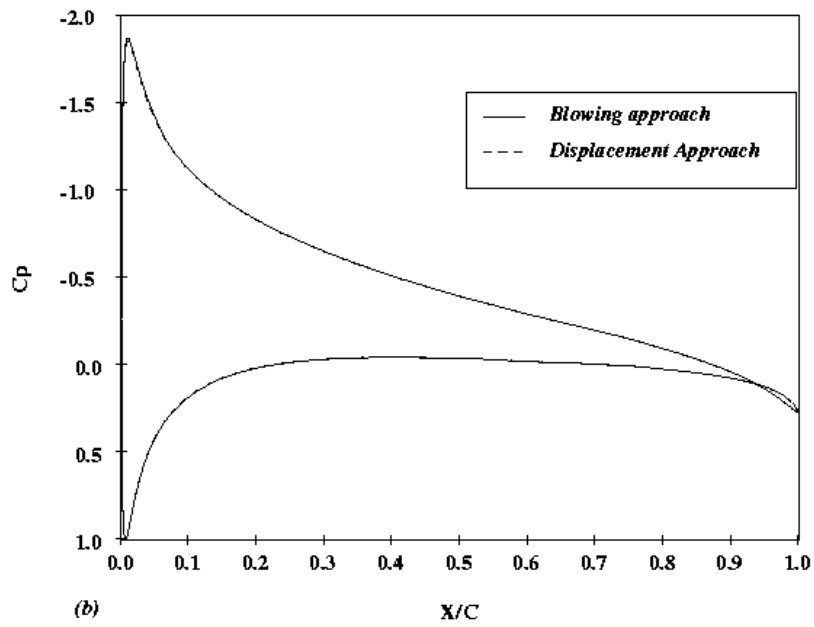
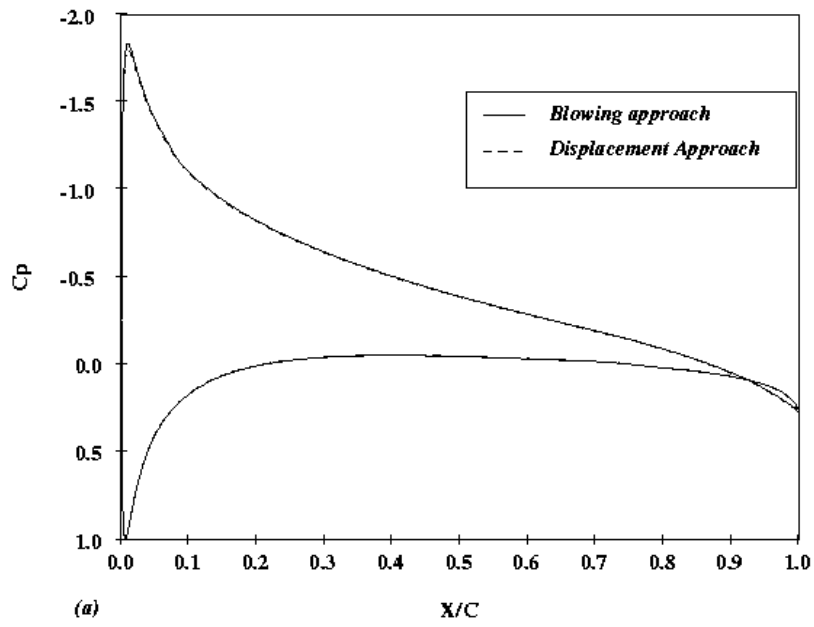


Fig. 5 Effects of Panel Number on Solutions
 NACA 0012 Swept Wing - Inviscid Flow

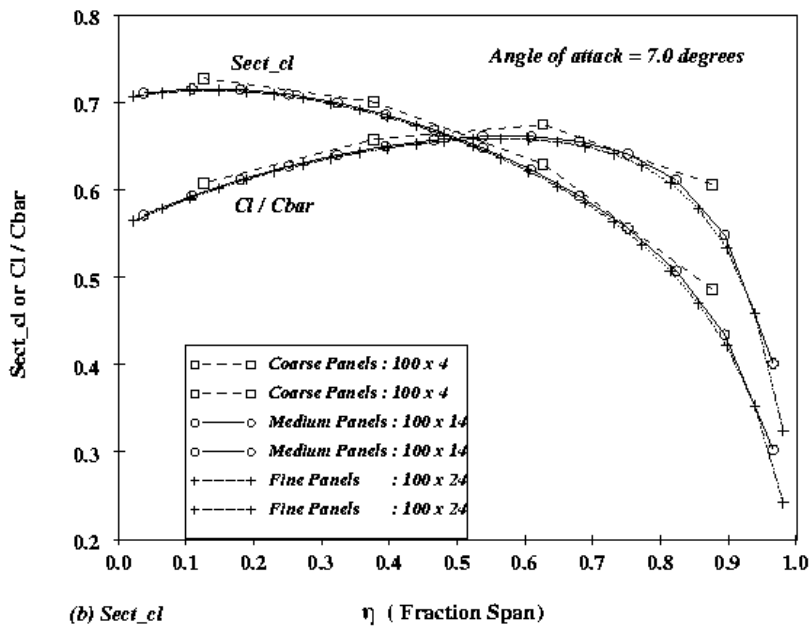
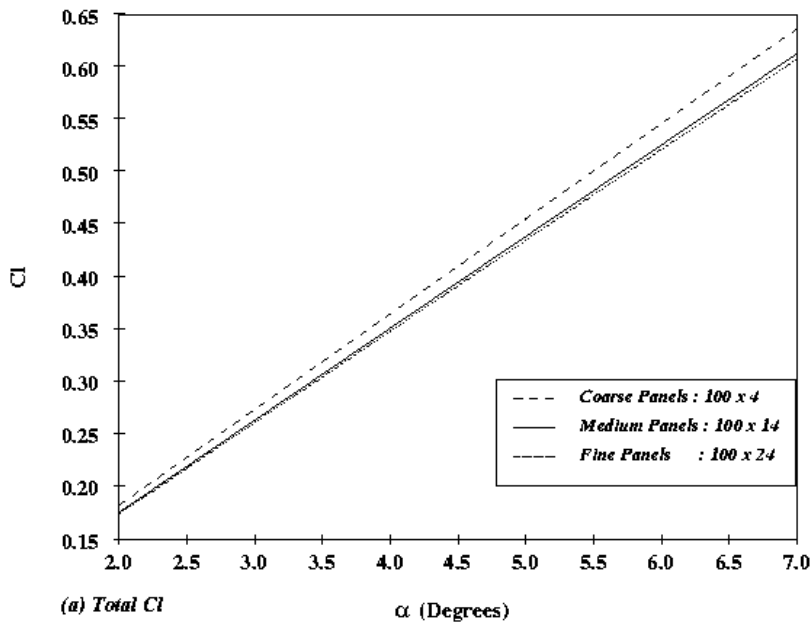
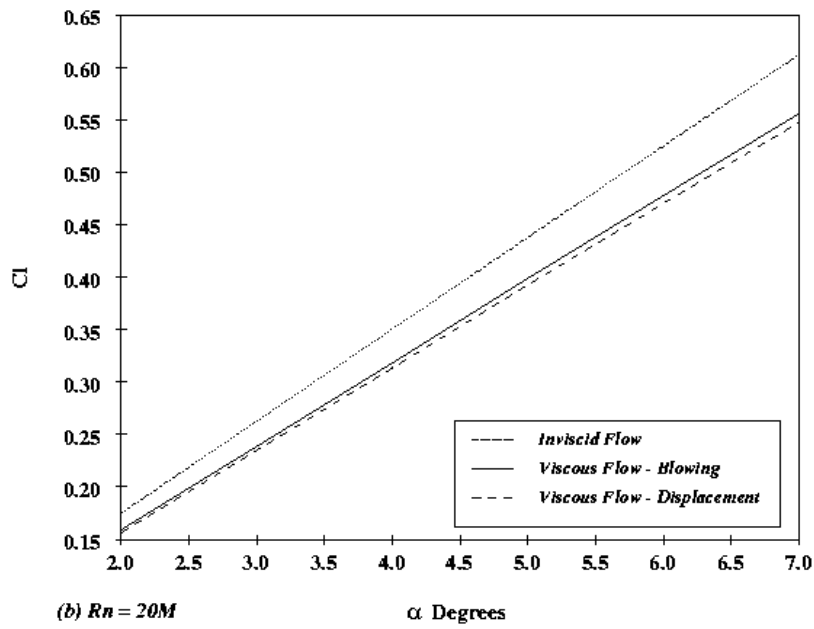
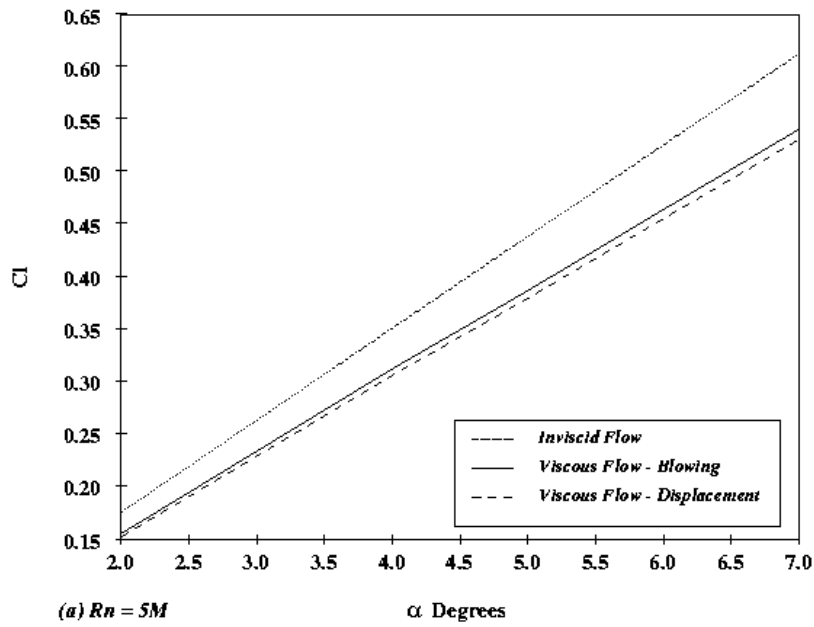
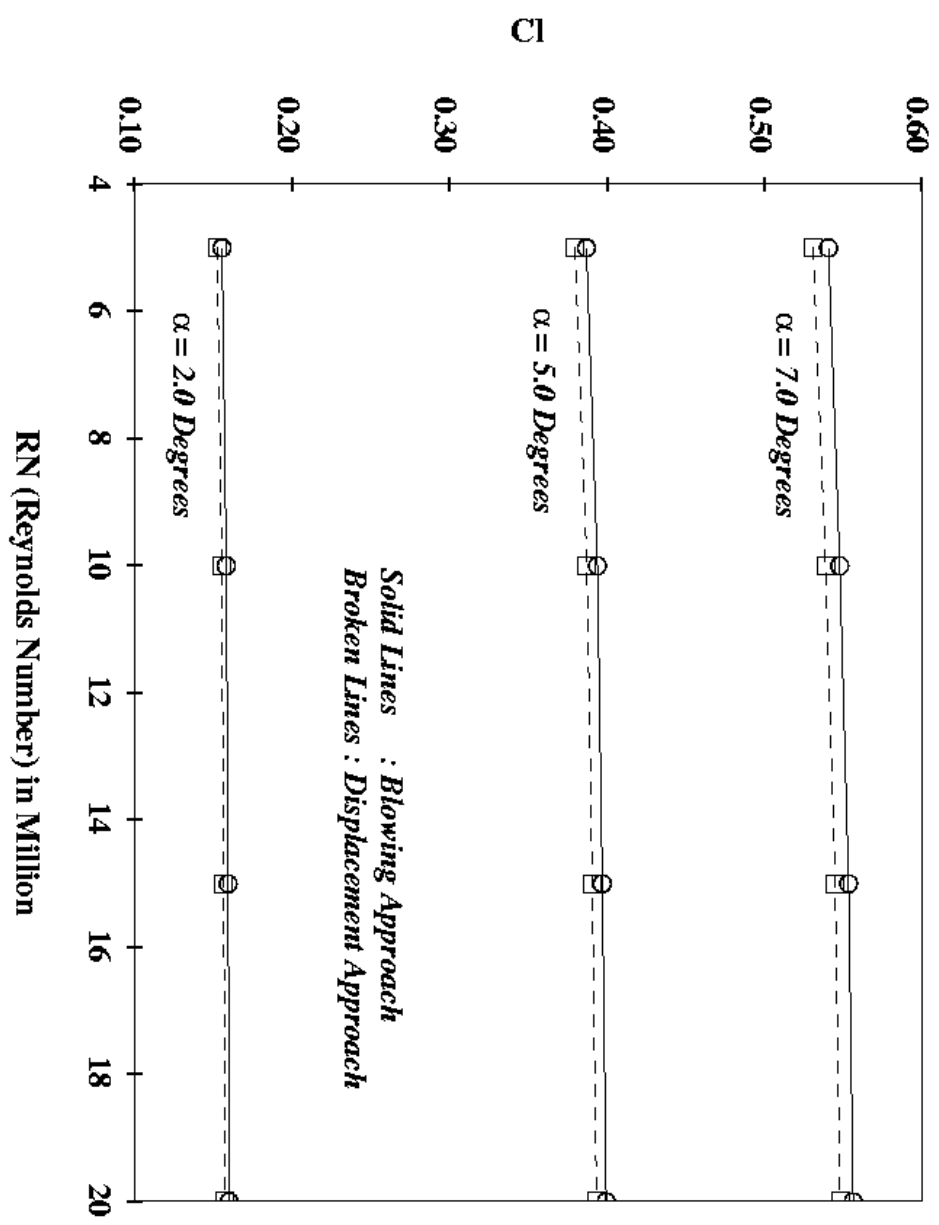


Fig. 6 Cl Distributions - Blowing vs Displacement Approach
 NACA 0012 Swept Wing with 2d B. L. Method



**Fig. 7 C1 Distribution - Blowing vs Displacement Approach
 NACA 0012 Swept Wing - RN Effects (2d BL Method)**



**Fig. 8 Trailing Edge Thickness (DTE) Distribution
NACA 0012 Swept Wing (2d BL method)**

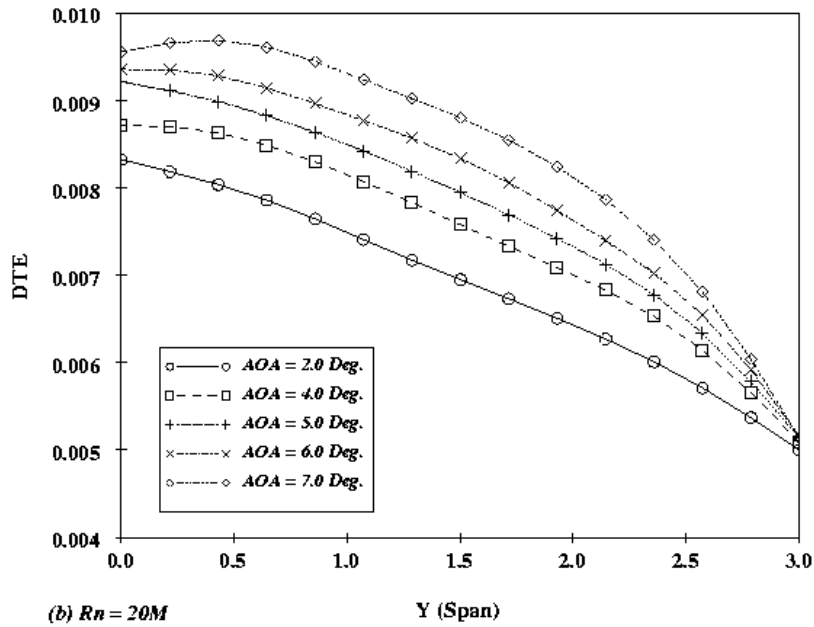
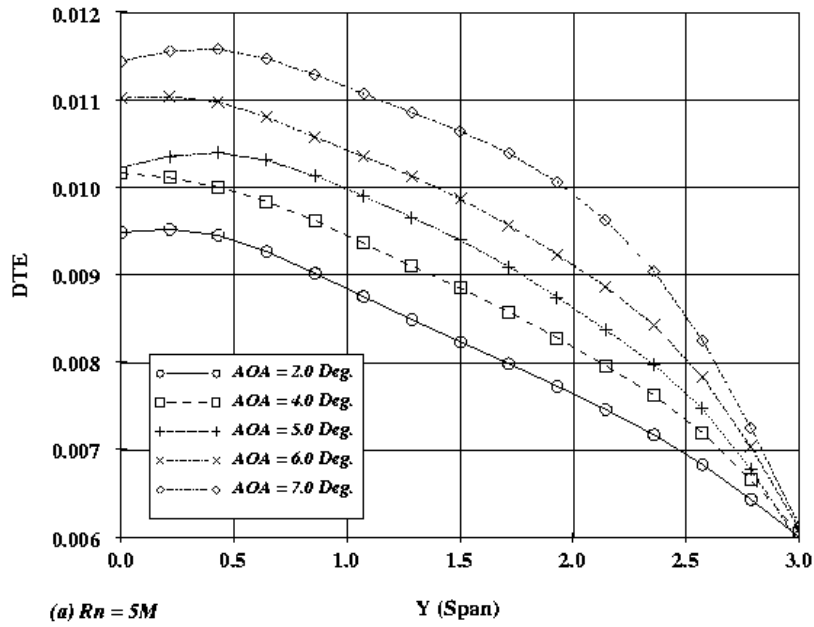


Fig. 9 Section Cl Distribution - Displacement Approach
 NACA0012 Swept Wing (2d BL Method)

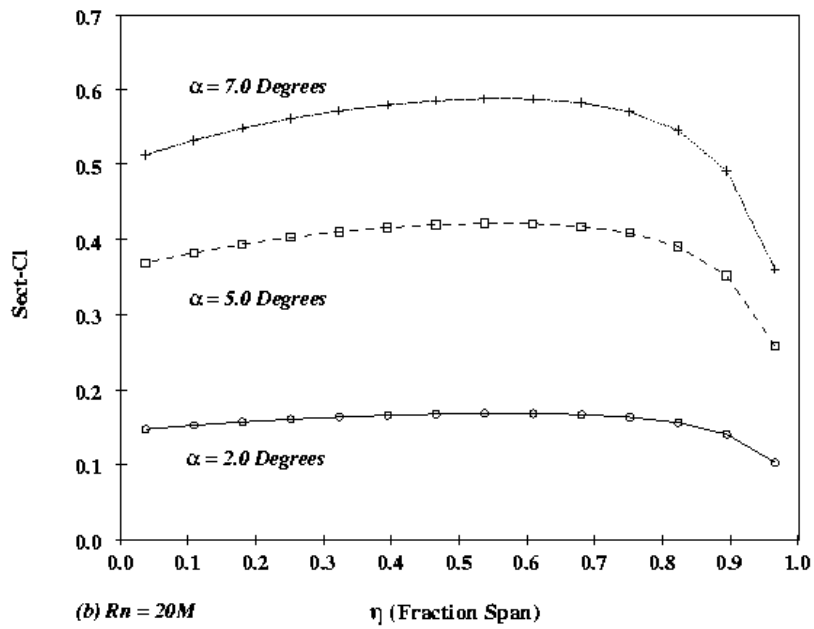
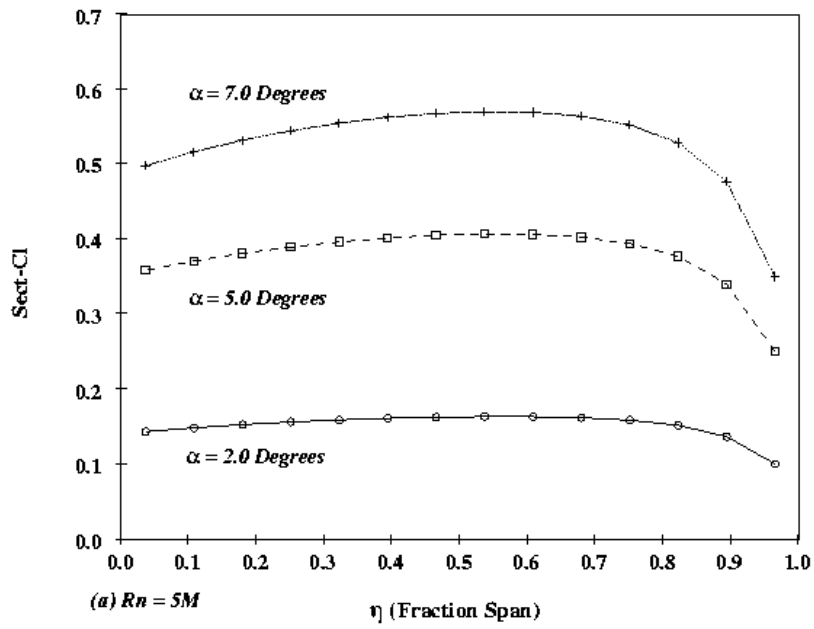


Fig. 10 C_l Distributions - 2D BL vs Quasi-3D BL Method
 NACA0012 Swept Wing - Displacement Approach

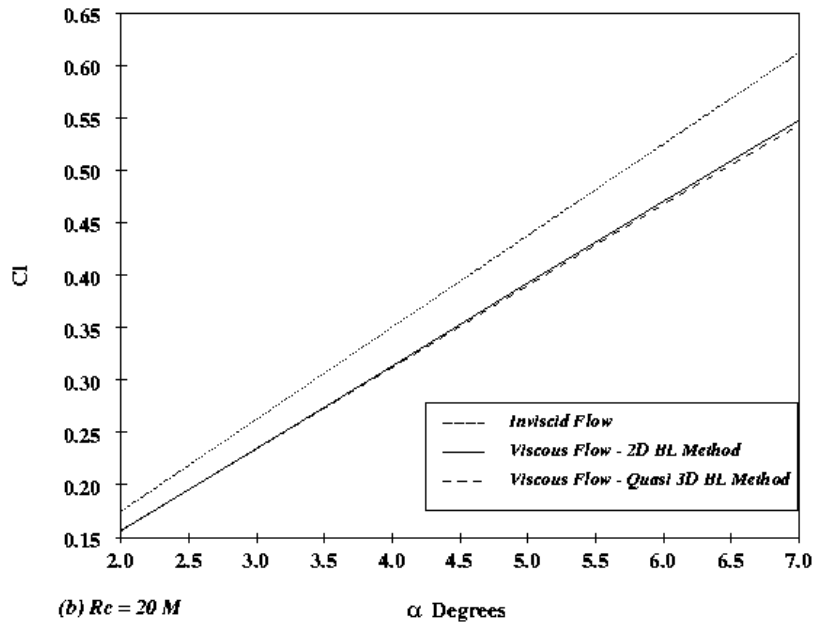
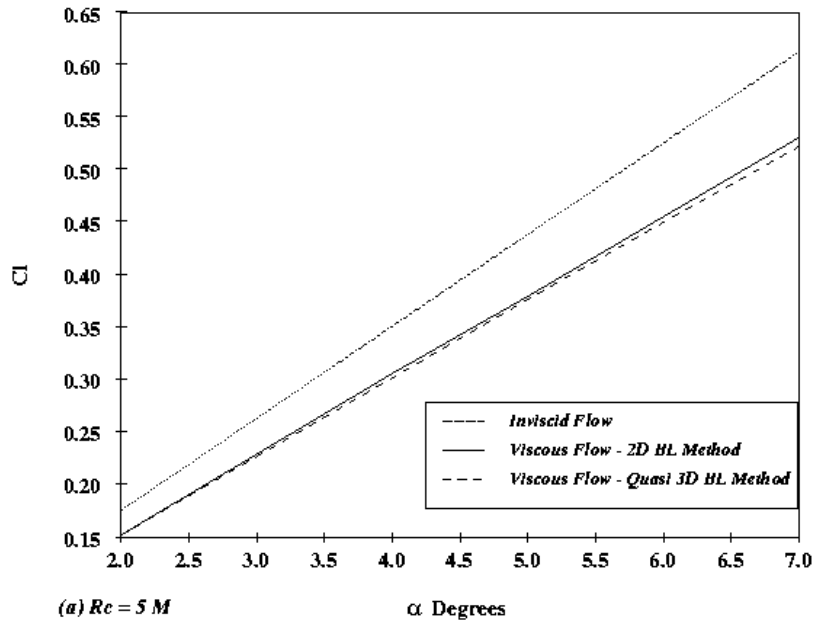


Fig. 11 C1 Distribution - 2d BL vs Quasi 3d BL Method
 NACA 0012 Swept Wing - RN Effects (Displacement Approach)

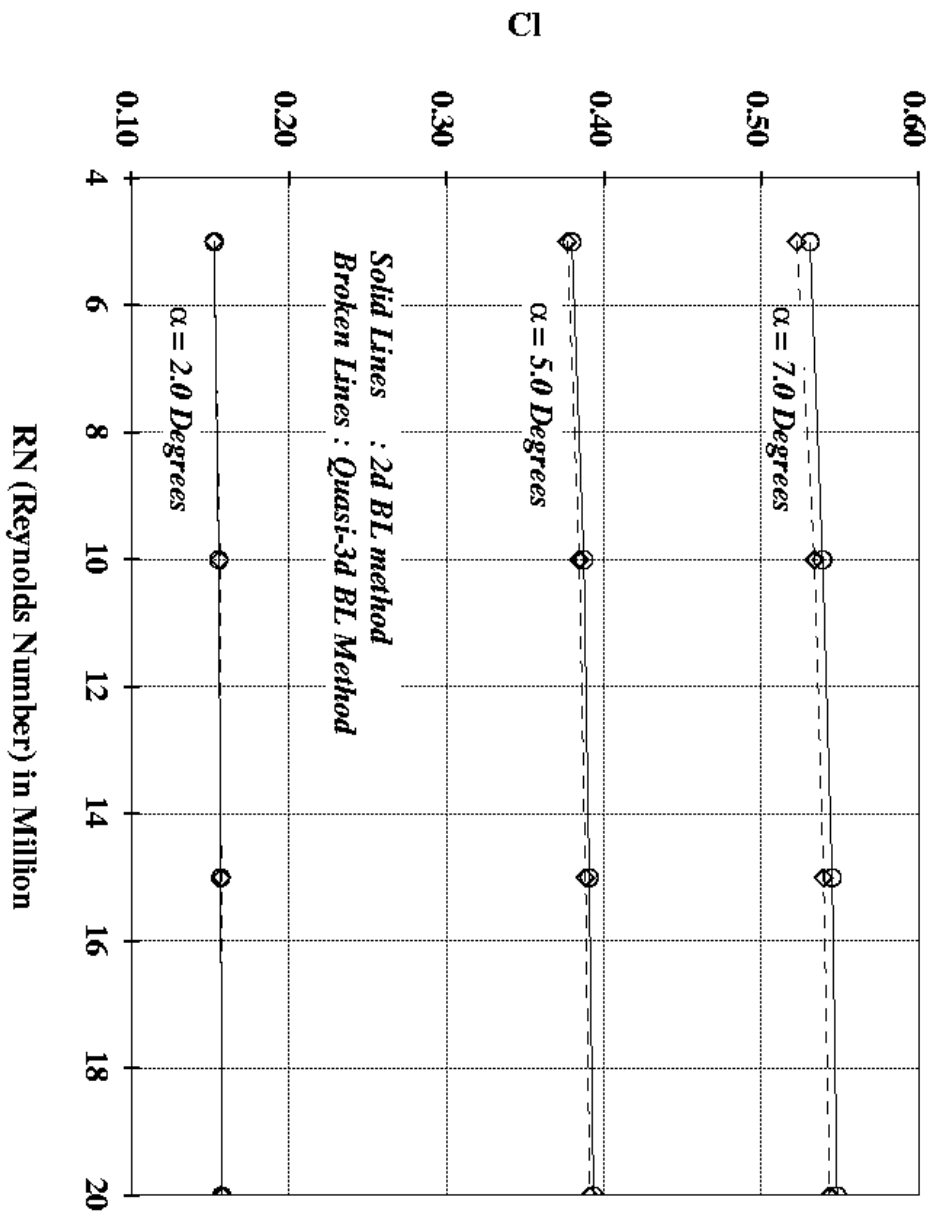


Fig. 12 Trailing Edge Thickness (DTE) Distribution
 NACA 0012 Swept Wing at $Rn = 5M$

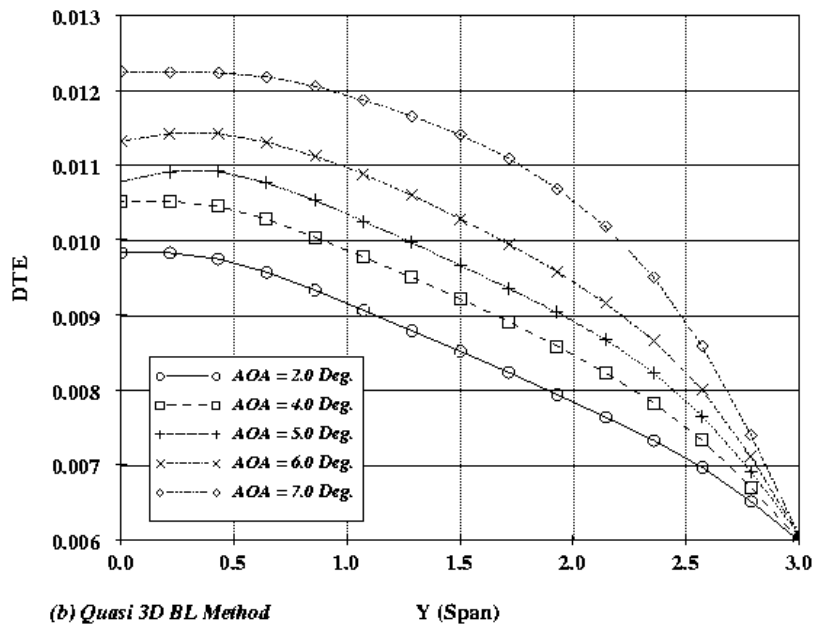
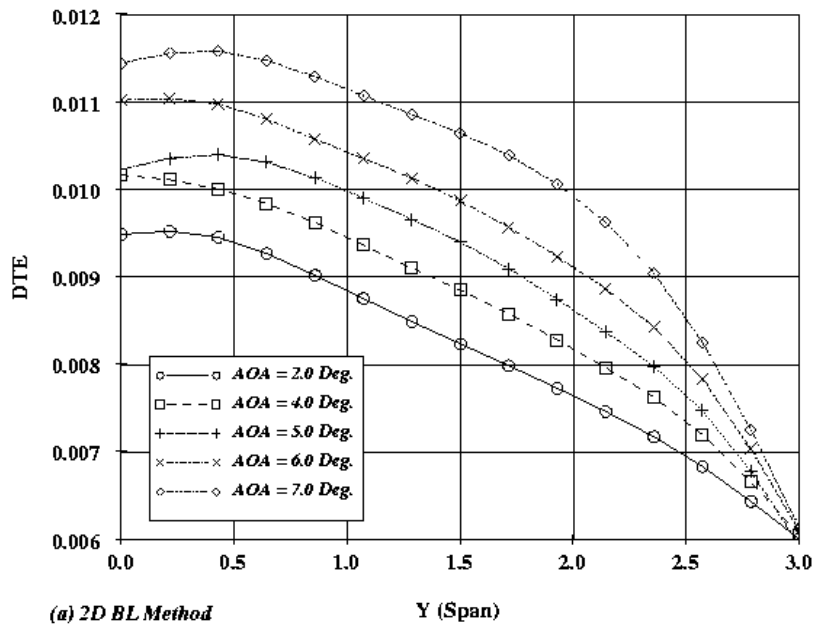


Fig. 13 Sect-CI Distribution - Displacement Thickness Approach
 NACA 0012 Swept Wing - 2D BL vs Quasi 3D BL Method

